CAAP Annual Report

Date of Report: *10/7/2020*

Prepared for: *U.S. DOT Pipeline and Hazardous Materials Safety Administration*

Contract Number: 693JK31850001CAAP

Project Title: *Development of Low-Power Wireless Sensor Network of Conductivity Probes for Detection of Corrosive Fluids Inside Pressure Vessels and Piping*

Prepared by: *Matthew Cullin, University of Alaska Anchorage*

Contact Information: *PI: Matt Cullin, mcullin@alaska.edu, (907) 786 - 1038*

For annual period ending: *10/7/2020***

** *Per AOR contact instructions, this annual report will provide details of the first two years of the contract, as the previous annual report contained insufficient detail.*

Business and Activity Section

(a) Contract Activity

No contract modifications are requested at this time.

To date, $237,922.94 has been spent on this project ($71,897.72 in Y1, and $166,025.22 in Y2). This leaves $59,674.06 unspent. While the cost distribution over the project year is different than the original budget, the bottom line for the project remains unchanged. The remaining funds will be sufficient to complete the project work. For a detailed list of expenditures, see Appendix 1.

(b) Status Update of Annual Activities

Y1: All scheduled tasks were completed in Y1 per the original project timeline. Two undergraduate design teams conducted semester-long projects to design the conductivity probe body and a pressure test vessel for the probe. The graduate research assistant (GRA) completed finite element analysis of several probe configurations.

Y2: Most of the scheduled tasks were completed in Y2 per the original project timeline. The major hurdle that was encountered was an inability to generate sufficient power from a reasonably-sized (3”x3”) thermoelectric generator under normal pipeline operating conditions. As a result, alternative methods of energy harvesting (solar) and storage (battery + super capacitor) were pursued. In addition, a dissimilar metal binary conductivity probe was designed and tested as an ultra-low-power sensing option. As such, the prototype of a fully-functional probe was delayed pending finalization of the electrode materials. The low-power Zensor™ microcontroller modules were fully specified and will be ordered in the near future. The graduate research assistant, Christina Forbes, completed her MSME degree.

(c) Cost share activity

Cost share has been executed per the original project budget. Cost share is entirely faculty salary.

(d) Progress on project tasks

The status of relevant project tasks is summarized in the Gantt chart below (Table 1). The details and documentation for each task are included in the Results and Discussion section below.

The major hurdle that was encountered was an inability to generate sufficient power from a reasonably-sized (3”x3”) thermoelectric generator under normal pipeline operating conditions. As a result, alternative methods of energy harvesting (solar) and storage (battery + super capacitor) were pursued. In addition, a dissimilar metal binary conductivity probe was designed and tested as an ultra-low-power sensing option. As such, the prototype of a fully-functional probe was delayed pending finalization of the electrode materials. Y2 conference presentations were cancelled due to COVID-19, however the conference paper was published.

Detailed discussion and descriptions for the following:

1. Background and Objectives in Y1 and Y2

1.1 Background

The purpose of this project was to design and test a low-power wireless network of conductivity sensors for detecting conductive fluids (electrolyte) inside pipelines and pressure vessels. To this end the project tasks and timeline in Table 1 were undertaken.

1.2 Objectives in the Y1 and Y2

The objectives in Y1 and Y2 can be broadly classified as follows:

- Design and analysis of conductivity probes and supporting test apparatus (Y1)
- Development of measurement sequence (Y2)
- Testing of probe designs and measurement sequence (Y2,Y3)
- Design and testing of thermoelectric generator + super capacitor as a local nodal power source (Y2)
- Integration of sensor design/measurement sequence and power generation and storage into Zensor™ microcontroller (node). (Y3)

The individual tasks associated with each of these broad objectives are found in Table 1.

Table 1: Status of project tasks

Individual	Task #	Activity (relevant objective)	F18	S19	Su19	F19	S20	Su20	F20	S21	Su21	Status
PI (all)	1	Kick Off Meeting										Complete
PI (all)	2	Establish relevent operational limits for conductivity probe and WSN (all)										Complete
UGDT	3	Design stand-alone conductivity probe body										Complete
GRA	4	Simulate conductivity electrode configurations										Complete
UGRA	5	Prototype stand-alone conductivity probe										Modified
UGDT	6	Design CC-holder-integrated conductivity probe body										Complete
GRA	7	Design, prototype, and test WSN integration electronics										Ongoing, delayed
UGDT	8	Test stand-alone conductivity probe										Complete
UGDT	9	Prototype CC-holder-integrated conductivity probe										Complete
GRA	10	Design, prototype, and test energy harvesting and storage system										Ongoing, delayed
UGRA	11	Prototype CC-holder-integrated conductivity probe										Delayed, modified
GRA	12	Prototype and test full system										Delayed
UGDT	13	Test CC-holder-integrated conductivity probe										Ongoing
GRA	14	Build and test multi-node WSN of conductivity sensors										Ongoing
UGRA	15	Assist GRA with test of multi-node WSN of conductivity sensors										Modified
GRA	16	Prepare thesis										Complete
PI (Cullin)	17	Manage budget and project reporting										
PI (Cullin)	18	Advise and oversee UGRA										
co-PI (Petersen)	19	Advise and oversee GRA										
co-PI (Srinivasan)	20	Prepare materials for and oversee UGDTs										
PI (all)	21	Prepare and submit quarterly Performance Progess Reports	Q1	Q2	Q3	Q4	Q5	Q6	Q7	Q8	Q9	Q10	Q11	Q12	
PI (all)	22	Travel to, and present at, a remote government and/or public event										Modified
PI (Cullin)	23	Prepare and submit Draft Final Research Report										
PI (Cullin)	24	Prepare and submit Public Final Research Report										
PI (Cullin)	25	Deliver close-out Internet-Based Presentation										

2. Experimental Program in Y1 and Y2

2.1 Experimental design

Y1: The Y1 activities (Task # 1-5 in Table 1) were focused on the design and analysis of conductivity probes and supporting test apparatus. The experimental methods used included the finite element method for analyzing the stresses in the probe body and pressure test vessel and the potential/current distributions for various electrode configurations. It is worth noting that the pressure test vessel was not part of the original project description. The design of this apparatus is an academic exercise meant to bring additional undergraduate students into the current project. No project funds were spent on this additional design work. The details of the design methodology can be found in the attached reports (Appendices 2 and 3).

Y2: The Y1 activities (Task # 6-10 in Table 1) were focused on the development of measurement sequence (Y2), testing of probe designs and measurement sequence, and design and testing of thermoelectric generator + super capacitor as a local nodal power source. The details and documentation of the methods used to complete these tasks can be found in the Master's thesis written by the graduate research assistant on this project (Appendix 4) and a report on the thermoelectric generator characterization (Appendix 5).

Preliminary measurements were conducted on an ultra-low-power binary conductivity probe utilizing the galvanic effect between dissimilar metals (copper and aluminum). These measurements were conducted using an Arduino Wifi RevB microcontroller in air, oil, and conductive electrolyte (sodium chloride solution).

3. Results and Discussions

Appendices 2-6 contain reports that detail the results and discussion of the various project tasks undertaken in Y1 and Y2. A high-level summary of the results is provided below:

- A single probe, with a removable corrosion coupon holder was designed to satisfy both probe configurations (flush-mount and coupon-holder-integrated) described in the original proposal.

- A 4-electrode conductivity probe, arranged in a linear configuration was determined to provide adequate sensitivity over the range of conductivities of interest (oil to seawater) while remaining practical in terms of the size constraints associated with 2-inch hydraulic access fittings.

- 4-mm-diameter graphite (or nickel) electrodes were specified. Functional prototypes of the sensing element were constructed from epoxy (mount) and graphite (electrodes).

- A current-interrupt measurement sequence was successfully utilized to obtain conductivity measurements. This sequence consisted of the establishment of a test current between the outer electrodes, a sudden interruption of the test current, and a measurement of the instantaneous potential drop on interrupt. The latter potential drop is attributed entirely to ohmic potential gradients, rather than polarization of the electrodes or ionic inhomogeneity. This technique, while effective, was determined to use a significant amount of energy relative to the operational power of the microcontrollers.

- Conductivity measurements were successfully conducted in an oil-water mixture. As expected, the readings were affected by the flow regime and the degree of agitation and mixing of the two phases.

- Alternating current (AC) conductivity measurement techniques were considered; however, the additional electronics and power consumption were not compatible with the low-cost, low-power targets of the measurement system being designed.

- Thermoelectric generation was found to be impractical for typical operations. Alternative sources of energy harvesting are being developed, namely, solar with the addition of a small battery to bridge the darker winter months found in arctic climates.

- Discussions with industry advisors indicate that they would favor solar over thermoelectric as a power source. The former requires fewer perforations of the insulation/weather barrier of the pipelines operating on the North Slope. This is advantageous as it minimizes the risk of Corrosion Under Insulation (CUI) at the node locations.

- A binary approach (yes/no) to conductivity measurement utilizing dissimilar material electrodes (galvanic effect) is being explored. Preliminary experiments indicate that this configuration can be used to detect the presence of an electrolyte, while minimizing the power consumption during the measurement. A 4-electrode (2+2) configuration is being pursued to allow for sequential testing and the detection of electrode fouling. The downside is that the result is binary and so the nature of the electrolyte (exact value of conductivity) cannot be determined from the readings.

4. Future work

In Y3, the primary focus will be:

- the full integration of the galvanic measurement element with the Zensor™ microcontroller and a solar power source.

- Testing of a sensor network (multiple nodes) to establish practical sample and data transmission rates for such a network.

Appendix 1: Project expenditure details

Description	Amount	FSYR	Period	Project Year	Trans Date
ARDUINO STORE	25.36	2019	8	1	19-Feb-19
DKC*DIGI KEY CORP	43.05	2019	8	1	19-Feb-19
AMZN MKTP US	34.67	2019	8	1	19-Feb-19
ADAFRUIT INDUSTRIES	18.66	2019	8	1	19-Feb-19
ARDUINO STORE	12.98	2019	8	1	19-Feb-19
DKC*DIGI KEY CORP	22.04	2019	8	1	19-Feb-19
AMZN MKTP US	17.75	2019	8	1	19-Feb-19
ADAFRUIT INDUSTRIES	9.55	2019	8	1	19-Feb-19
ARDUINO STORE	38.34	2019	8	1	19-Feb-19
DKC*DIGI KEY CORP	65.09	2019	8	1	19-Feb-19
AMZN MKTP US	52.42	2019	8	1	19-Feb-19
ADAFRUIT INDUSTRIES	28.21	2019	8	1	19-Feb-19
ARDUINO STORE	40.62	2019	8	1	21-Feb-19
AMZN MKTP US	172.59	2019	8	1	21-Feb-19
ADAFRUIT INDUSTRIES	43.16	2019	8	1	21-Feb-19
ARDUINO STORE	20.8	2019	8	1	21-Feb-19
AMZN MKTP US	88.37	2019	8	1	21-Feb-19
ADAFRUIT INDUSTRIES	22.1	2019	8	1	21-Feb-19
ARDUINO STORE	61.42	2019	8	1	21-Feb-19
AMZN MKTP US	260.96	2019	8	1	21-Feb-19
ADAFRUIT INDUSTRIES	65.26	2019	8	1	21-Feb-19
HR Payroll 2019 BW 5 2	114.38	2019	10	1	17-Apr-19
HR Payroll 2019 BW 6 2	114.37	2019	10	1	17-Apr-19
HR Payroll 2019 BW 7 2	15.26	2019	10	1	17-Apr-19
HR Payroll 2019 BW 5 2	58.56	2019	10	1	17-Apr-19
HR Payroll 2019 BW 6 2	58.56	2019	10	1	17-Apr-19
HR Payroll 2019 BW 7 2	7.81	2019	10	1	17-Apr-19
HR Payroll 2019 BW 5 2	172.94	2019	10	1	17-Apr-19
HR Payroll 2019 BW 6 2	172.93	2019	10	1	17-Apr-19
HR Payroll 2019 BW 7 2	23.07	2019	10	1	17-Apr-19
HR Payroll 2019 BW 10 0	190.61	2019	10	1	27-Apr-19
HR Payroll 2019 BW 10 0	97.59	2019	10	1	27-Apr-19
HR Payroll 2019 BW 10 0	288.2	2019	10	1	27-Apr-19
HR Payroll 2019 BW 11 0	274.52	2019	11	1	11-May-19
HR Payroll 2019 BW 11 0	140.55	2019	11	1	11-May-19
HR Payroll 2019 BW 11 0	415.07	2019	11	1	11-May-19
HR Payroll 2019 BW 12 0	1,403.20	2019	11	1	25-May-19
HR Payroll 2019 BW 12 0	91.21	2019	11	1	25-May-19
HR Payroll 2019 BW 12 0	46.7	2019	11	1	25-May-19
HR Payroll 2019 BW 12 0	718.44	2019	11	1	25-May-19
HR Payroll 2019 BW 12 0	137.91	2019	11	1	25-May-19
HR Payroll 2019 BW 12 0	2,121.64	2019	11	1	25-May-19

HR Payroll 2019 BW 13 0	4,094.61	2019	12	1	8-Jun-19
HR Payroll 2019 BW 13 0	1,403.20	2019	12	1	8-Jun-19
HR Payroll 2019 BW 13 0	1,335.97	2019	12	1	8-Jun-19
HR Payroll 2019 BW 13 0	684.02	2019	12	1	8-Jun-19
HR Payroll 2019 BW 13 0	2,096.44	2019	12	1	8-Jun-19
HR Payroll 2019 BW 13 0	718.44	2019	12	1	8-Jun-19
HR Payroll 2019 BW 13 0	2,019.99	2019	12	1	8-Jun-19
HR Payroll 2019 BW 13 0	6,191.05	2019	12	1	8-Jun-19
HR Payroll 2019 BW 13 0	2,121.64	2019	12	1	8-Jun-19
HR Payroll 2019 BW 14 0	1,403.20	2019	12	1	22-Jun-19
HR Payroll 2019 BW 14 0	91.21	2019	12	1	22-Jun-19
HR Payroll 2019 BW 14 0	46.7	2019	12	1	22-Jun-19
HR Payroll 2019 BW 14 0	718.44	2019	12	1	22-Jun-19
HR Payroll 2019 BW 14 0	137.91	2019	12	1	22-Jun-19
HR Payroll 2019 BW 14 0	2,121.64	2019	12	1	22-Jun-19
HR Payroll 2019 BW 15 0	701.6	2019	12	1	30-Jun-19
HR Payroll 2019 BW 15 0	63.85	2019	12	1	30-Jun-19
HR Payroll 2019 BW 15 0	32.69	2019	12	1	30-Jun-19
HR Payroll 2019 BW 15 0	359.22	2019	12	1	30-Jun-19
HR Payroll 2019 BW 15 0	96.54	2019	12	1	30-Jun-19
HR Payroll 2019 BW 15 0	1,060.82	2019	12	1	30-Jun-19
HR Payroll 2019 BW 15 0	576.93	2020	1	1	6-Jul-19
HR Payroll 2019 BW 15 0	701.6	2020	1	1	6-Jul-19
HR Payroll 2019 BW 15 0	235.78	2020	1	1	6-Jul-19
HR Payroll 2019 BW 15 0	120.72	2020	1	1	6-Jul-19
HR Payroll 2019 BW 15 0	295.39	2020	1	1	6-Jul-19
HR Payroll 2019 BW 15 0	359.22	2020	1	1	6-Jul-19
HR Payroll 2019 BW 15 0	356.5	2020	1	1	6-Jul-19
HR Payroll 2019 BW 15 0	872.32	2020	1	1	6-Jul-19
HR Payroll 2019 BW 15 0	1,060.82	2020	1	1	6-Jul-19
HR Payroll 2019 BW 16 0	1,153.85	2020	1	1	20-Jul-19
HR Payroll 2019 BW 16 0	1,403.20	2020	1	1	20-Jul-19
HR Payroll 2019 BW 16 0	471.54	2020	1	1	20-Jul-19
HR Payroll 2019 BW 16 0	241.43	2020	1	1	20-Jul-19
HR Payroll 2019 BW 16 0	590.77	2020	1	1	20-Jul-19
HR Payroll 2019 BW 16 0	718.44	2020	1	1	20-Jul-19
HR Payroll 2019 BW 16 0	712.97	2020	1	1	20-Jul-19
HR Payroll 2019 BW 16 0	1,744.62	2020	1	1	20-Jul-19
HR Payroll 2019 BW 16 0	2,121.64	2020	1	1	20-Jul-19
SIGMA ALDRICH US	144.35	2020	1	1	25-Jul-19
SIGMA ALDRICH US	73.91	2020	1	1	25-Jul-19
SIGMA ALDRICH US	218.26	2020	1	1	25-Jul-19
HR Payroll 2019 BW 17 0	471.54	2020	2	1	3-Aug-19
HR Payroll 2019 BW 17 0	241.43	2020	2	1	3-Aug-19
HR Payroll 2019 BW 17 0	712.97	2020	2	1	3-Aug-19
HR Payroll 2019 BW 17 0	1,153.85	2020	2	1	12-Aug-19
HR Payroll 2019 BW 17 0	1,403.20	2020	2	1	12-Aug-19

HR Payroll 2019 BW 17 0	590.77	2020	2	1	12-Aug-19
HR Payroll 2019 BW 17 0	718.44	2020	2	1	12-Aug-19
HR Payroll 2019 BW 17 0	1,744.62	2020	2	1	12-Aug-19
HR Payroll 2019 BW 17 0	2,121.64	2020	2	1	12-Aug-19
HR Payroll 2019 BW 18 0	576.93	2020	2	1	17-Aug-19
HR Payroll 2019 BW 18 0	1,403.20	2020	2	1	17-Aug-19
HR Payroll 2019 BW 18 0	299.62	2020	2	1	17-Aug-19
HR Payroll 2019 BW 18 0	153.41	2020	2	1	17-Aug-19
HR Payroll 2019 BW 18 0	295.39	2020	2	1	17-Aug-19
HR Payroll 2019 BW 18 0	718.44	2020	2	1	17-Aug-19
HR Payroll 2019 BW 18 0	453.03	2020	2	1	17-Aug-19
HR Payroll 2019 BW 18 0	872.32	2020	2	1	17-Aug-19
HR Payroll 2019 BW 18 0	2,121.64	2020	2	1	17-Aug-19
HR Payroll 2019 BW 19 0	701.6	2020	2	1	31-Aug-19
HR Payroll 2019 BW 19 0	359.22	2020	2	1	31-Aug-19
HR Payroll 2019 BW 19 0	1,060.82	2020	2	1	31-Aug-19
HR Payroll 2019 BW 20 0	701.6	2020	3	1	14-Sep-19
HR Payroll 2019 BW 20 0	359.22	2020	3	1	14-Sep-19
HR Payroll 2019 BW 20 0	1,060.82	2020	3	1	14-Sep-19
HR Payroll 2019 BW 21 0	701.6	2020	3	1	28-Sep-19
HR Payroll 2019 BW 21 0	359.22	2020	3	1	28-Sep-19
HR Payroll 2019 BW 21 0	1,060.82	2020	3	1	28-Sep-19
Year 2 Total	**$71,897.72**				

DKC*DIGI KEY CORP	530.03	2020	4	2	3-Oct-19
DKC*DIGI KEY CORP	271.38	2020	4	2	3-Oct-19
DKC*DIGI KEY CORP	801.41	2020	4	2	3-Oct-19
HR Payroll 2019 BW 22 0	701.6	2020	4	2	12-Oct-19
HR Payroll 2019 BW 22 0	359.22	2020	4	2	12-Oct-19
HR Payroll 2019 BW 22 0	1,060.82	2020	4	2	12-Oct-19
CoEng ME Grad Asst Waiver	5,194.00	2020	4	2	16-Oct-19
CoEng ME Grad Asst Waiver	5,194.00	2020	4	2	16-Oct-19
OMEGA *ENGINEERING	138	2020	4	2	24-Oct-19
LOWES #00907	37.83	2020	4	2	24-Oct-19
GRAINGER	69.98	2020	4	2	24-Oct-19
AMZN MKTP US	12.74	2020	4	2	24-Oct-19
OMEGA *ENGINEERING	70.66	2020	4	2	24-Oct-19
LOWES #00907	19.37	2020	4	2	24-Oct-19
GRAINGER	35.83	2020	4	2	24-Oct-19
AMZN MKTP US	6.52	2020	4	2	24-Oct-19
OMEGA *ENGINEERING	208.66	2020	4	2	24-Oct-19
LOWES #00907	57.2	2020	4	2	24-Oct-19
GRAINGER	105.81	2020	4	2	24-Oct-19
AMZN MKTP US	19.26	2020	4	2	24-Oct-19
HR Payroll 2019 BW 23 0	701.6	2020	4	2	26-Oct-19
HR Payroll 2019 BW 23 0	359.22	2020	4	2	26-Oct-19

HR Payroll 2019 BW 23 0	1,060.82	2020	4	2	26-Oct-19
HR Payroll 2019 BW 24 0	701.6	2020	5	2	9-Nov-19
HR Payroll 2019 BW 24 0	359.22	2020	5	2	9-Nov-19
HR Payroll 2019 BW 24 0	1,060.82	2020	5	2	9-Nov-19
OMEGA *ENGINEERING	393	2020	5	2	21-Nov-19
OMEGA *ENGINEERING	201.22	2020	5	2	21-Nov-19
OMEGA *ENGINEERING	594.22	2020	5	2	21-Nov-19
HR Payroll 2019 BW 25 0	701.6	2020	5	2	23-Nov-19
HR Payroll 2019 BW 25 0	359.22	2020	5	2	23-Nov-19
HR Payroll 2019 BW 25 0	1,060.82	2020	5	2	23-Nov-19
NACE INTERNATIONAL	20	2020	5	2	28-Nov-19
NACE INTERNATIONAL	10.24	2020	5	2	28-Nov-19
NACE INTERNATIONAL	30.24	2020	5	2	28-Nov-19
HR Payroll 2019 BW 26 0	701.6	2020	6	2	7-Dec-19
HR Payroll 2019 BW 26 0	359.22	2020	6	2	7-Dec-19
HR Payroll 2019 BW 26 0	1,060.82	2020	6	2	7-Dec-19
HR Payroll 2020 BW 1 0	701.6	2020	6	2	21-Dec-19
HR Payroll 2020 BW 1 0	359.22	2020	6	2	21-Dec-19
HR Payroll 2020 BW 1 0	1,060.82	2020	6	2	21-Dec-19
HR Payroll 2020 BW 2 0	701.6	2020	7	2	4-Jan-20
HR Payroll 2020 BW 2 0	359.22	2020	7	2	4-Jan-20
HR Payroll 2020 BW 2 0	1,060.82	2020	7	2	4-Jan-20
HR Payroll 2020 BW 3 0	701.6	2020	7	2	18-Jan-20
HR Payroll 2020 BW 3 0	359.22	2020	7	2	18-Jan-20
HR Payroll 2020 BW 3 0	1,060.82	2020	7	2	18-Jan-20
CoEng ME Grad Asst Waiver	6,176.00	2020	7	2	29-Jan-20
CoEng ME Grad Asst Waiver	6,176.00	2020	7	2	29-Jan-20
HR Payroll 2020 BW 4 0	701.6	2020	8	2	10-Feb-20
HR Payroll 2020 BW 4 0	359.22	2020	8	2	10-Feb-20
HR Payroll 2020 BW 4 0	1,060.82	2020	8	2	10-Feb-20
HR Payroll 2020 BW 5 0	701.6	2020	8	2	15-Feb-20
HR Payroll 2020 BW 5 0	359.22	2020	8	2	15-Feb-20
HR Payroll 2020 BW 5 0	1,060.82	2020	8	2	15-Feb-20
HR Payroll 2020 BW 6 0	701.6	2020	8	2	29-Feb-20
HR Payroll 2020 BW 6 0	359.22	2020	8	2	29-Feb-20
HR Payroll 2020 BW 6 0	1,060.82	2020	8	2	29-Feb-20
CPI*COLEPARMERINSTRUMT	191.46	2020	9	2	5-Mar-20
CPI*COLEPARMERINSTRUMT	98.03	2020	9	2	5-Mar-20
CPI*COLEPARMERINSTRUMT	289.49	2020	9	2	5-Mar-20
HR Payroll 2020 BW 7 0	701.6	2020	9	2	14-Mar-20
HR Payroll 2020 BW 7 0	359.22	2020	9	2	14-Mar-20
HR Payroll 2020 BW 7 0	1,060.82	2020	9	2	14-Mar-20
HR Payroll 2020 BW 8 0	701.6	2020	9	2	28-Mar-20
HR Payroll 2020 BW 8 0	359.22	2020	9	2	28-Mar-20
HR Payroll 2020 BW 8 0	1,060.82	2020	9	2	28-Mar-20
HR Payroll 2020 BW 9 0	701.6	2020	10	2	11-Apr-20
HR Payroll 2020 BW 9 0	359.22	2020	10	2	11-Apr-20

HR Payroll 2020 BW 9 0	1,060.82	2020	10	2	11-Apr-20
HR Payroll 2020 BW 10 0	701.6	2020	10	2	25-Apr-20
HR Payroll 2020 BW 10 0	359.22	2020	10	2	25-Apr-20
HR Payroll 2020 BW 10 0	1,060.82	2020	10	2	25-Apr-20
HR Payroll 2020 BW 11 0	701.6	2020	11	2	9-May-20
HR Payroll 2020 BW 11 0	359.22	2020	11	2	9-May-20
HR Payroll 2020 BW 11 0	1,060.82	2020	11	2	9-May-20
ARDUINO STORE	490.61	2020	11	2	14-May-20
ARDUINO STORE	251.19	2020	11	2	14-May-20
ARDUINO STORE	741.8	2020	11	2	14-May-20
15830-3PYH 03/14/20 Srinivasan, R	791.76	2020	11	2	15-May-20
15830-3PYH 03/14/20 Srinivasan, R	799	2020	11	2	15-May-20
15830-3PYH 03/14/20 Srinivasan, R	405.38	2020	11	2	15-May-20
15830-3PYH 03/14/20 Srinivasan, R	409.09	2020	11	2	15-May-20
15830-3PYH 03/14/20 Srinivasan, R	1,197.14	2020	11	2	15-May-20
15830-3PYH 03/14/20 Srinivasan, R	1,208.09	2020	11	2	15-May-20
HR Payroll 2020 BW 12 0	4,091.40	2020	11	2	23-May-20
HR Payroll 2020 BW 12 0	887.25	2020	11	2	23-May-20
HR Payroll 2020 BW 12 0	701.6	2020	11	2	23-May-20
HR Payroll 2020 BW 12 0	1,363.83	2020	11	2	23-May-20
HR Payroll 2020 BW 12 0	698.28	2020	11	2	23-May-20
HR Payroll 2020 BW 12 0	2,094.80	2020	11	2	23-May-20
HR Payroll 2020 BW 12 0	454.27	2020	11	2	23-May-20
HR Payroll 2020 BW 12 0	359.22	2020	11	2	23-May-20
HR Payroll 2020 BW 12 0	2,062.11	2020	11	2	23-May-20
HR Payroll 2020 BW 12 0	6,186.20	2020	11	2	23-May-20
HR Payroll 2020 BW 12 0	1,341.52	2020	11	2	23-May-20
HR Payroll 2020 BW 12 0	1,060.82	2020	11	2	23-May-20
CoEng ME Grad Asst Waiver	4,080.00	2020	11	2	27-May-20
CoEng ME Grad Asst Waiver	4,080.00	2020	11	2	27-May-20
HR Payroll 2020 BW 13 0	4,091.40	2020	12	2	6-Jun-20
HR Payroll 2020 BW 13 0	855.75	2020	12	2	6-Jun-20
HR Payroll 2020 BW 13 0	701.6	2020	12	2	6-Jun-20
HR Payroll 2020 BW 13 0	1,360.97	2020	12	2	6-Jun-20
HR Payroll 2020 BW 13 0	696.82	2020	12	2	6-Jun-20
HR Payroll 2020 BW 13 0	2,094.80	2020	12	2	6-Jun-20
HR Payroll 2020 BW 13 0	438.14	2020	12	2	6-Jun-20
HR Payroll 2020 BW 13 0	359.22	2020	12	2	6-Jun-20
HR Payroll 2020 BW 13 0	2,057.79	2020	12	2	6-Jun-20
HR Payroll 2020 BW 13 0	6,186.20	2020	12	2	6-Jun-20
HR Payroll 2020 BW 13 0	1,293.89	2020	12	2	6-Jun-20

HR Payroll 2020 BW 13 0	1,060.82	2020	12	2	6-Jun-20
DKC*DIGI KEY CORP	66.53	2020	12	2	11-Jun-20
AMAZON.COM*MY54Q20O2	207.71	2020	12	2	11-Jun-20
THE HOME DEPOT #8940	122.76	2020	12	2	11-Jun-20
DKC*DIGI KEY CORP	34.06	2020	12	2	11-Jun-20
AMAZON.COM*MY54Q20O2	106.35	2020	12	2	11-Jun-20
THE HOME DEPOT #8940	62.85	2020	12	2	11-Jun-20
DKC*DIGI KEY CORP	100.59	2020	12	2	11-Jun-20
AMAZON.COM*MY54Q20O2	314.06	2020	12	2	11-Jun-20
THE HOME DEPOT #8940	185.61	2020	12	2	11-Jun-20
AMAZON.COM*MY8XB3KE0	14.42	2020	12	2	15-Jun-20
AMAZON.COM*MY8XB3KE0	7.38	2020	12	2	15-Jun-20
AMAZON.COM*MY8XB3KE0	21.8	2020	12	2	15-Jun-20
HR Payroll 2020 BW 14 0	1,176.00	2020	12	2	20-Jun-20
HR Payroll 2020 BW 14 0	701.6	2020	12	2	20-Jun-20
HR Payroll 2020 BW 14 0	170.87	2020	12	2	20-Jun-20
HR Payroll 2020 BW 14 0	87.49	2020	12	2	20-Jun-20
HR Payroll 2020 BW 14 0	602.11	2020	12	2	20-Jun-20
HR Payroll 2020 BW 14 0	359.22	2020	12	2	20-Jun-20
HR Payroll 2020 BW 14 0	258.36	2020	12	2	20-Jun-20
HR Payroll 2020 BW 14 0	1,778.11	2020	12	2	20-Jun-20
HR Payroll 2020 BW 14 0	1,060.82	2020	12	2	20-Jun-20
DKC*DIGI KEY CORP	70.2	2020	12	2	25-Jun-20
DKC*DIGI KEY CORP	35.94	2020	12	2	25-Jun-20
DKC*DIGI KEY CORP	106.14	2020	12	2	25-Jun-20
HR Payroll 2020 BW 15 0	807.58	2020	12	2	30-Jun-20
HR Payroll 2020 BW 15 0	687.75	2020	12	2	30-Jun-20
HR Payroll 2020 BW 15 0	491.12	2020	12	2	30-Jun-20
HR Payroll 2020 BW 15 0	359.86	2020	12	2	30-Jun-20
AMZN MKTP US	17.94	2020	12	2	30-Jun-20
AMZN MKTP US	494.92	2020	12	2	30-Jun-20
HR Payroll 2020 BW 15 0	184.25	2020	12	2	30-Jun-20
HR Payroll 2020 BW 15 0	413.48	2020	12	2	30-Jun-20
HR Payroll 2020 BW 15 0	352.13	2020	12	2	30-Jun-20
HR Payroll 2020 BW 15 0	251.45	2020	12	2	30-Jun-20
AMZN MKTP US	9.19	2020	12	2	30-Jun-20
AMZN MKTP US	253.4	2020	12	2	30-Jun-20
HR Payroll 2020 BW 15 0	544.11	2020	12	2	30-Jun-20
HR Payroll 2020 BW 15 0	1,221.06	2020	12	2	30-Jun-20
HR Payroll 2020 BW 15 0	1,039.88	2020	12	2	30-Jun-20
HR Payroll 2020 BW 15 0	742.57	2020	12	2	30-Jun-20
AMZN MKTP US	27.13	2020	12	2	30-Jun-20
AMZN MKTP US	748.32	2020	12	2	30-Jun-20
HR Payroll 2020 BW 15 0	346.11	2021	1	2	4-Jul-20
HR Payroll 2020 BW 15 0	341.25	2021	1	2	4-Jul-20
HR Payroll 2020 BW 15 0	210.48	2021	1	2	4-Jul-20
HR Payroll 2020 BW 15 0	158.74	2021	1	2	4-Jul-20

HR Payroll 2020 BW 15 0	81.27	2021	1	2	4-Jul-20
HR Payroll 2020 BW 15 0	177.21	2021	1	2	4-Jul-20
HR Payroll 2020 BW 15 0	174.72	2021	1	2	4-Jul-20
HR Payroll 2020 BW 15 0	107.77	2021	1	2	4-Jul-20
HR Payroll 2020 BW 15 0	240.01	2021	1	2	4-Jul-20
HR Payroll 2020 BW 15 0	523.32	2021	1	2	4-Jul-20
HR Payroll 2020 BW 15 0	515.97	2021	1	2	4-Jul-20
HR Payroll 2020 BW 15 0	318.25	2021	1	2	4-Jul-20
DKC*DIGI KEY CORP	94.26	2021	1	2	9-Jul-20
DKC*DIGI KEY CORP	48.26	2021	1	2	9-Jul-20
DKC*DIGI KEY CORP	142.52	2021	1	2	9-Jul-20
HR Payroll 2020 BW 16 0	1,153.68	2021	1	2	18-Jul-20
HR Payroll 2020 BW 16 0	1,002.75	2021	1	2	18-Jul-20
HR Payroll 2020 BW 16 0	701.6	2021	1	2	18-Jul-20
HR Payroll 2020 BW 16 0	516.05	2021	1	2	18-Jul-20
HR Payroll 2020 BW 16 0	264.22	2021	1	2	18-Jul-20
HR Payroll 2020 BW 16 0	590.68	2021	1	2	18-Jul-20
HR Payroll 2020 BW 16 0	513.41	2021	1	2	18-Jul-20
HR Payroll 2020 BW 16 0	359.22	2021	1	2	18-Jul-20
HR Payroll 2020 BW 16 0	780.27	2021	1	2	18-Jul-20
HR Payroll 2020 BW 16 0	1,744.36	2021	1	2	18-Jul-20
HR Payroll 2020 BW 16 0	1,516.16	2021	1	2	18-Jul-20
HR Payroll 2020 BW 16 0	1,060.82	2021	1	2	18-Jul-20
AMZN MKTP US	53.45	2021	1	2	30-Jul-20
AMZN MKTP US	27.37	2021	1	2	30-Jul-20
AMZN MKTP US	80.82	2021	1	2	30-Jul-20
HR Payroll 2020 BW 17 0	1,153.68	2021	2	2	1-Aug-20
HR Payroll 2020 BW 17 0	887.25	2021	2	2	1-Aug-20
HR Payroll 2020 BW 17 0	701.6	2021	2	2	1-Aug-20
HR Payroll 2020 BW 17 0	1.59	2021	2	2	1-Aug-20
HR Payroll 2020 BW 17 0	504.99	2021	2	2	1-Aug-20
HR Payroll 2020 BW 17 0	0.81	2021	2	2	1-Aug-20
HR Payroll 2020 BW 17 0	258.55	2021	2	2	1-Aug-20
HR Payroll 2020 BW 17 0	590.68	2021	2	2	1-Aug-20
HR Payroll 2020 BW 17 0	454.27	2021	2	2	1-Aug-20
HR Payroll 2020 BW 17 0	359.22	2021	2	2	1-Aug-20
HR Payroll 2020 BW 17 0	2.4	2021	2	2	1-Aug-20
HR Payroll 2020 BW 17 0	763.54	2021	2	2	1-Aug-20
HR Payroll 2020 BW 17 0	1,744.36	2021	2	2	1-Aug-20
HR Payroll 2020 BW 17 0	1,341.52	2021	2	2	1-Aug-20
HR Payroll 2020 BW 17 0	1,060.82	2021	2	2	1-Aug-20
HR Payroll 2020 BW 18 0	929.25	2021	2	2	15-Aug-20
HR Payroll 2020 BW 18 0	701.6	2021	2	2	15-Aug-20
HR Payroll 2020 BW 18 0	1.63	2021	2	2	15-Aug-20
HR Payroll 2020 BW 18 0	158.36	2021	2	2	15-Aug-20
HR Payroll 2020 BW 18 0	0.83	2021	2	2	15-Aug-20
HR Payroll 2020 BW 18 0	81.08	2021	2	2	15-Aug-20

HR Payroll 2020 BW 18 0	475.78	2021	2	2	15-Aug-20
HR Payroll 2020 BW 18 0	359.22	2021	2	2	15-Aug-20
HR Payroll 2020 BW 18 0	2.46	2021	2	2	15-Aug-20
HR Payroll 2020 BW 18 0	239.44	2021	2	2	15-Aug-20
HR Payroll 2020 BW 18 0	1,405.03	2021	2	2	15-Aug-20
HR Payroll 2020 BW 18 0	1,060.82	2021	2	2	15-Aug-20
SL corr temp/student rate R15 & R16	3.43	2021	2	2	18-Aug-20
SB corr temp/student rate R15 & R16	0.37	2021	2	2	18-Aug-20
SB corr temp/student rate R15 & R16	0.19	2021	2	2	18-Aug-20
SL corr temp/student rate R15 & R16	1.76	2021	2	2	18-Aug-20
SB corr temp/student rate R15 & R16	0.56	2021	2	2	18-Aug-20
SL corr temp/student rate R15 & R16	5.19	2021	2	2	18-Aug-20
CoEng ME Grad Asst Waiver	834	2021	2	2	19-Aug-20
CoEng ME Grad Asst Waiver	834	2021	2	2	19-Aug-20
HR Payroll 2020 BW 19 0	149.63	2021	2	2	29-Aug-20
HR Payroll 2020 BW 19 0	0.15	2021	2	2	29-Aug-20
HR Payroll 2020 BW 19 0	0.08	2021	2	2	29-Aug-20
HR Payroll 2020 BW 19 0	76.61	2021	2	2	29-Aug-20
HR Payroll 2020 BW 19 0	0.23	2021	2	2	29-Aug-20
HR Payroll 2020 BW 19 0	226.24	2021	2	2	29-Aug-20
MCMASTER-CARR	165.14	2021	3	2	10-Sep-20
MCMASTER-CARR	84.55	2021	3	2	10-Sep-20
MCMASTER-CARR	249.69	2021	3	2	10-Sep-20
HR Payroll 2020 BW 20 0	52.5	2021	3	2	12-Sep-20
HR Payroll 2020 BW 20 0	0.05	2021	3	2	12-Sep-20
HR Payroll 2020 BW 20 0	0.03	2021	3	2	12-Sep-20
HR Payroll 2020 BW 20 0	26.88	2021	3	2	12-Sep-20
HR Payroll 2020 BW 20 0	0.08	2021	3	2	12-Sep-20
HR Payroll 2020 BW 20 0	79.38	2021	3	2	12-Sep-20
Year 2 Total	**$166,025.22**				
Project Total (YTD)	**$237,922.94**				
Total Project Request	**$297,597.00**				
Funds remaining	**$59,674.06**				

Appendix 2: Conductivity probe design report

CONDUCTIVITY PROBE DESIGN

Dr. Matthew Cullin

Christina Forbes
Kellyn Mushovic
Luis Marroquin
Megan Wagner
Brandon Adkins
Maria Cucullu

INTRODUCTION

Corrosion is the process whereby materials chemically deteriorate. This deterioration produces oxides that flake away from a base metal. In order for corrosion to occur, there must be a metal, oxygen or a compound that can be reduced, and an electrolyte [1]. The most common types of corrosion which occur in pipelines are uniform corrosion, pitting corrosion, and erosion-corrosion. Uniform and pitting corrosion are common in oil and gas pipelines due to the presence of seawater in the oil-gas mixtures [1]. Some compounds which are present in these mixtures, such as salts and sulfates, create stronger electrolytes which can increase corrosion rates. Pipelines may have a protective inner coating to help prevent corrosion.
Erosion-corrosion occurs when solid particles in the fluid collide with the pipe wall and create an environment for corrosion to occur. The erosion can remove protective coatings allowing the metal and electrolyte to come in contact with each other, or it can increase the rate of corrosion damage by breaking off pipe wall material already affected by corrosion. When not managed properly, corrosion can cause damage leading to leaks and bursts in oil and gas pipelines. Pipeline spills can have a detrimental impact to the environment and be extremely hazardous to people in their vicinity.

There are many methods to protect against corrosion. A relatively expensive measure consists of coating the inside of the piping material with a corrosion resistant film. This coating, however, can be damaged by erosion as mentioned earlier. Corrosion can also be minimized through injection treatments that produce chemical reactions to create a less suitable environment for corrosion to happen. Injection treatments can reduce the level of live organisms, salts, and sulfates, to reduce the presence of effective electrolytes required for corrosive reactions. Injection treatments can be administered both continuously and in batches treatments but must

be done at locations with high accessibility [1]. Despite the methods available for minimizing corrosion, the reaction can almost never be completely eliminated and methods are needed to monitor corrosion rates regularly in oil and gas pipelines.

There are many different methods of inspecting the pipeline for corrosion. These can be divided into two categories: destructive testing and non-destructive testing. Destructive testing involves taking the structure apart to look for corrosion. This method is not widely used as it requires shutting down the line and can be costly. Non-destructive testing (NDT) involves using equipment and instruments to look for corrosion without affecting the structure of the pipeline. These methods require trained experts to analyze and interpret results from the tests [2]. These methods are more commonly used because they can be run while the line is active. One method of NDT is visual inspection, where trained experts look for corrosion and pipe pitting on the exterior of the pipe. Other methods include Magnetic Flux Leakage (MFL), Eddy currents, and Ultrasonic Testing. MFL works by using a powerful magnet to magnetize the pipe and cause a magnetic field [3]. Any defects or flaws, such as metal loss due to corrosion, cause 'leaks' in the magnetic flux which are then recorded by the magnetic sensors [4]. Eddy currents are alternating magnetic fields caused by alternating electric currents being sent through eddy current coils in the assembly. Discontinuities or deformations in the pipe wall cause a change in the flow of the eddy current and are recorded by sensors [5]. Ultrasonic testing uses sound waves to inspect the internal structure of the pipeline [3]. Any cracks, defects in welds, or changes in wall thickness result in some or all of the sound waves to rebound back and be detected by the receiver. NDT methods can be found in probes or can also be incorporated into the pipeline inspection gauges (PIGs) that are mainly used to help clean the interior pipeline.

Corrosion can be detected in numerous ways with different types of equipment, but the main two devices used are corrosion coupon holders and Electrical Resistance (ER) probes. Corrosion coupons are also very commonly used to anticipate problematic corrosion in pipelines. Coupons are pre-weighed metal samples which can be exposed to a corrosive environment to study how they deteriorate. These coupons are removed from the corrosive environment and re-weighed after a predetermined time interval (60- 120 days) [6]. The measured weight loss is then used to calculate the corrosion rate of the metal.

Although coupon holders have been utilized longer, ER probes provide a quicker way to glean similar information. ER probes provide instantaneous measurements that can be read at any time or as frequently as required. These probes measure the change in resistance of an integrated metal sample as it is exposed to corrosive conditions. The corrosion of the metal results in a decrease in cross-sectional area, which causes an increase in electrical resistance [7]. From this relationship the corrosion rate can be determined.

The oil and gas industry is one of the largest economic providers to the state of Alaska [8]. Therefore, adequate maintenance to these pipelines is critical. Corrosion has been linked to a large percentage of pipeline failures across North America. Thus, a simple and efficient way to identify corrosion before it affects structural integrity is a necessity. Generally speaking, most current techniques used to measure corrosion require a very large amount of power. Considering the fact that most of Alaska is rural and uninhabited, with a very hostile winter environment, a high powered corrosion monitoring option is not feasible. In the same way, sending out maintenance teams to such remote locations is not fiscally desirable. For these

reasons, a low powered, wireless corrosion monitoring alternative would be extremely beneficial for pipeline applications in Alaska.

PROJECT STATEMENT

It is the goal of this senior design project to produce a viable conductivity probe design which will be able to operate using environmentally extracted energy. If the design proves promising, a working prototype of the low power conductivity probe will be fabricated. Additionally, finite element analysis will be performed on a model of the in-stream probe in order to further support the viability of the probe's design. The final probe prototype will be designed in such a way that it will be suitable for oil and gas pipeline applications in regions of Alaska where access to power is limited.

Finally, a probe design with all accompanying calculations and specifications used in the design process is expected to be completed. The main probe design will be comprised of a flush mount conductivity sensor. This probe will feature a detachable cage with connections for corrosion coupons. This final design must be able to operate up to maximum pressures of 1000 psi without failure and be retrievable through industry standard 2" NPT access fittings.

SCOPE OF PROJECT

The objective of this senior design project is to develop a conductivity probe which will eventually be duplicated to form a system of low power, wireless probes. These probes will monitor corrosion by providing data which will allow the conductivity of fluids passing through points of interest in pipelines to be determined. It is desirable that these probes run only on energy that can be extracted from their environment. Thus, these probes will be powered by a

trickle-charged capacitor, which will collect any available thermal or solar energy from its environment. This capacitor will eventually be designed by the Electrical Engineering department at the University of Alaska Anchorage. This will result in a cost effective manner of monitoring corrosion in low power areas of pipelines in Alaska.

This Senior Design project is part of a three year project which is scheduled to finish in the summer of 2021. Thus, this senior project will culminate in an initial prototype design which may be adapted as the project proceeds.

METHODS

The project's primary goal was to develop a well supported design for the future construction of a conductivity probe. With this in mind, the majority of time spent on this project was used to research the different components of the probe. The senior design research effort was divided into three different subcategories. These research tasks were: probe body design, seals and pipeline connections, and electrode COMSOL simulations.

I. Probe Body Design

The first step in designing the probe body was looking into industry standards and regulations for inline ER probes and coupon holders. Standard practice documents from the National Association of Corrosion Engineers (NACE) were used to determine the material, testing requirements, and isolation requirements for the probe body [9, 10, 11]. Similar designs from manufacturers within the corrosion monitoring industry were considered and compared alongside the NACE standard practices to identify potential material types and probe dimensions. Based on these references the probe body material was chosen to be 316L

stainless steel. The material choice and dimensions of the probe were then tested using Finite Element Analysis (FEA).

Using standard pipe sizes, the probe was dimensioned to fit flush mounted within a pipeline. This design choice was not only made to allow for the conductivity sensor on the lower probe face to interact with the solution within the pipe, but also to avoid obstructing the flow path for PIGs. The back end of the probe was designed to fit an industry standard 2” NPT access fitting [12]. The body of the probe was designed to be made out of hollow ⅝” 316L stainless steel tubing with 0.065” wall thickness to allow for space for wiring into and out of the probe. To allow for coupon testing in pipe segments where coupons are needed or required, an attachment was designed out of 316L stainless steel. The attachment fits onto the front end of the probe with space to hold two electrically isolated coupons. The cage style attachment shown below in Figure 1(a) is ideal for coupon addition while still maintaining fluid contact with the conductivity sensor on the front face of the probe. Between the cage attachment and the probes, shown in Figure 1(b), are electrically isolating spacers to prevent galvanic corrosion. These spacers are designed to be made out of ABS plastic. The final probe design was created in SolidWorks, a solid modeling computer-aided design and engineering program.

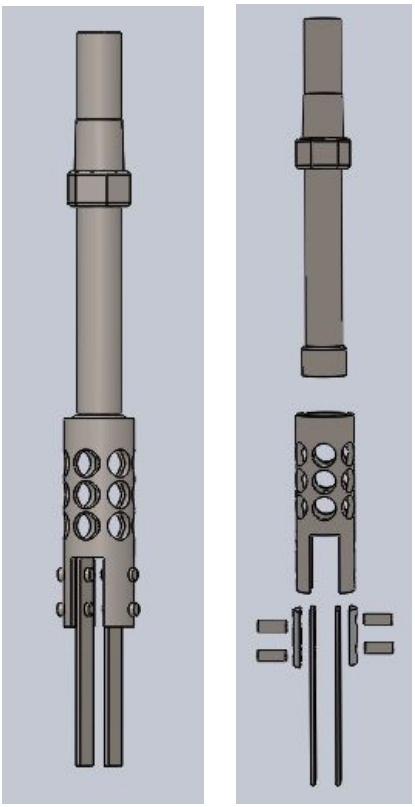

(a) **(b)**

Figure 1: (a) Assembled and **(b)** exploded view of model made in SolidWorks

To test the constructed solid model of the design, the design group of this project conducted a Finite Element Analysis (FEA) study on the probe body design with the cage attachment and coupons. The FEA study considered the fluid flow within the pipe, fluid properties of the oil mixture in worse case scenario situations, and physical dimensions of the probe model to determine the theoretical stresses and strains on the proposed design. The applied loads within the study were compared to the pressure and temperature ratings of the nominal pipe sizes within this projects range of interest (6”-14” nominal size oil and gas pipelines), shown below in Figure 2. Analysis of the study was conducted to determine necessary design adjustments moving forward.

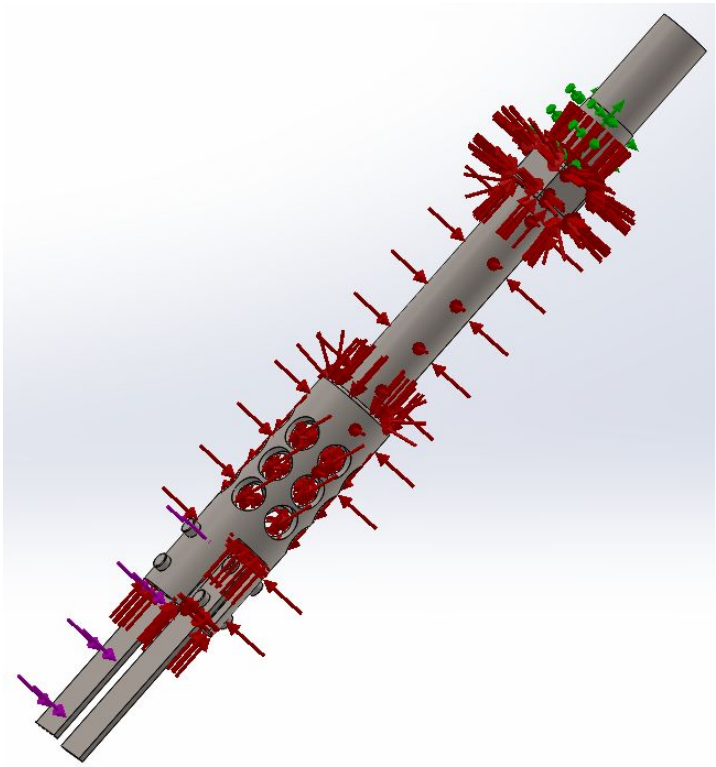

Figure 2: Probe FEA simulation applied boundary conditions

Figure 2 shows the locations where the probe design was fixed and where the applied loads are in order to do the FEA. The green arrows represent where the probe would be fixed for the simulation. This region was designated as the fixed region because it is where the probe body would be screwed in and attached to the access fitting on the pipeline. The red arrows represent the pressure from the inside of the pipeline that would be acting along the body of the probe. The FEA pressure that was used was 1250 psi because it is the pressure at which the prototype will eventually be tested at. This would also yield conservative results because it is above the expected pressure for our nominal pipe sizes of interest [13]. The purple arrows represent the fluid drag force that would act upon the coupons inside the pipeline. It was calculated with worse

case scenario numbers which resulted in 11.9 N. This calculation can be found in Appendix A. The calculation considered the density of crude oil at low, slow moving temperatures and a maximum fluid velocity of 15 ft/s [14].

The FEA simulation produced the stress distribution that can be seen below in Figure 3. From this figure it can be seen that the place of maximum stress is on the main shaft of the probe body. Figure 4 shows the precise location of the maximum stress which is on the inside of the main shaft where it is hollow. The calculated maximum stress came out to be 4.519×10^7 N/m^2, a value significantly lower than 1.7×10^8 N/m^2 yield strength of 316L stainless steel. The maximum stress was an initial concern since it plays a role in what the factor of safety would come out to be. Since the maximum stress was much lower than the yield stress, the calculated factor of safety from the FEA was 3.8. The calculation for this is shown in Appendix B.

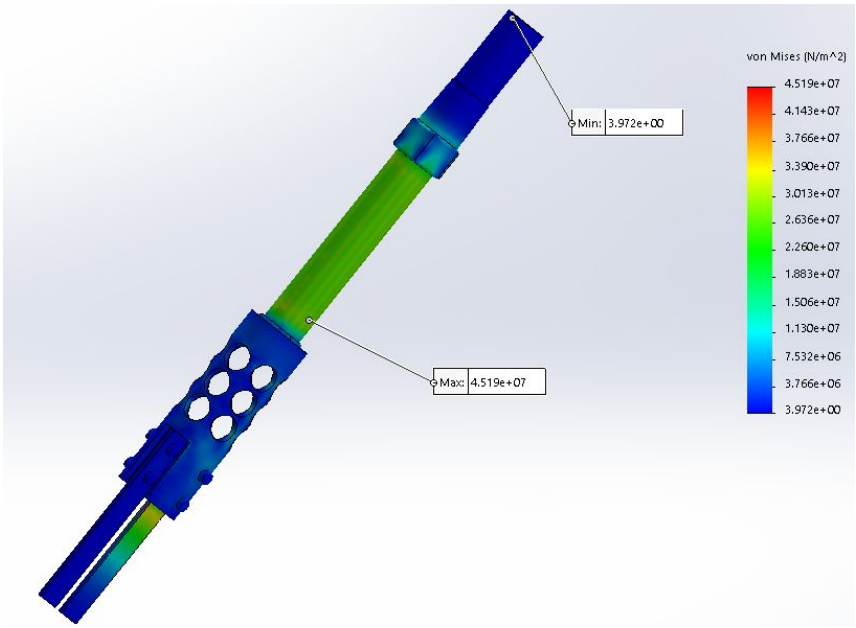

Figure 3: Probe FEA simulation results

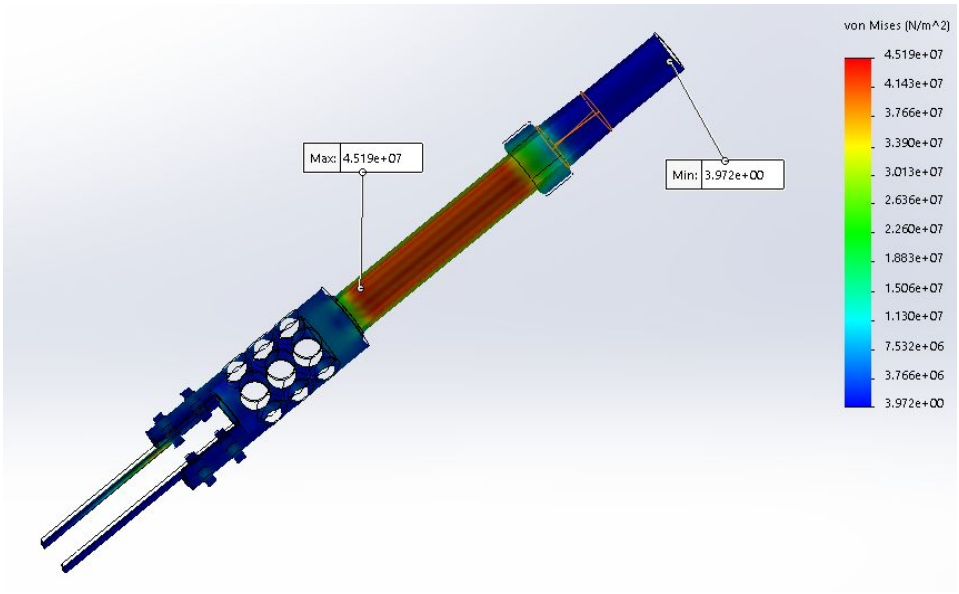

Figure 4: Probe FEA simulation section view results

II. Seals and Pipeline Connections

To properly seal the probe and prevent the fluid from leaking through, the team started by looking at how to seal the electrodes at the probe face. For this task, the team started off by looking at various material types starting with ceramics and then electrically non-conductive thermoplastics such as polytetrafluoroethylene (PTFE) and polyether ether ketone (PEEK) which are commonly used materials in the oil and gas industry. These materials were considered for the electrode seal due to their electrical isolation properties so that the seal doesn't interfere with the probes' measurements. Next, a secondary containment seal was considered for the probe body itself, in case the primary seal fails. For the secondary containment seal, a compression fitting was initially considered to allow the electrode wires to pass through while still providing an adequate seal of the probe body.

After having an understanding of what was required, the team then looked at what other probes on the market were utilizing. Looking at Cosasco, they tend to use either a glass or Ryton element seal along with a secondary glass sealed connector in the body as well as at the end of the probe [15,16,17]. While Metal Samples tends to use either glass or a two part epoxy for their element seal with a glass sealed connector at the end of the probe [18]. Looking at the coupon insulation, both Cosasco and Metal Samples have a large selection of Nylon and Teflon washers and spacers that they offer. The combination of the team's ideas as well as the other currently used methods can then be compared based on the effectiveness and ease of manufacturing to determine what would be the best method for the design moving forward.

For the failure of the electrode seal at the face, the probe body behind the seal will support it so that the seal doesn't fail in shear. Therefore, the main method of failure will likely either be failure of the adhesive bond between the electrode and the seal or a leak. For the case of a leak, the probe prototype will just have to be tested. But for the case of failure between the electrode and the seal, the force exerted on the electrode tip by the pressure differential can be distributed over the area of the mating surface as shown calculated in Appendix C. This calculation shows that the adhesive bond only needs to withstand 81.25 psi which is negligible compared to the strengths of most bonds considered.

For materials considered to seal the electrodes, the team looked at ceramics. Alumina ceramics have excellent strength and electrical isolation properties with a tensile strength of 38,000 psi and volume resistivity of $>10^{14}$ ohm*cm at 25 ^{o}C [19]. But ceramics tend to be harder to manufacture and more expensive than an alternative such as glass [20]. PTFE isn't as strong with a tensile strength of 4000 psi but is much more electrically resistive with a volume resistivity

of >10^{18} ohm*cm [21]. PEEK as compared to PTFE is much stronger with a tensile strength of 13,000-14,500 psi but is less electrically resistive with a volume resistivity of $5x10^{16}$ ohm*cm when tested using ASTM D-257 [22,23]. The major downfall of PEEK is the cost, as it is ten times more expensive than PTFE [22]. Glass seals meanwhile, offer more than adequate strength and electrical resistance with references quoting pressures up to 14,000 psi for compression seals and a volume resistance of <10^{12} ohm*cm at 25 ^{o}C [24,19].Then, taking a look at Ryton, it is a specialty polyphenylene sulfide (PPS) that is seen as an alternative to PEEK and is typically utilized in injection molding or is machined to fit [25]. In order to do compression molding, which we had access to, the raw PPS would have to be acquired and blended with fillers [26]. Lastly, for two part epoxies, EP31 from Master bond was a suitable option with a tensile strength of 6,000-7,000 psi and volume resistivity of >10^{15} ohm*cm at 24 ^{o}C [27]. EP31 also provided a tensile lap shear strength for aluminum to aluminum, which is a failure method that factors in bonding, of 4,000-4,200 psi [27]. All of the materials also have adequate chemical resistance ranging from resistance to fuel, oil, and gas to virtually chemically inert. And since all the materials had volume resistivities over 10^{9} ohm*cm they are all adequate insulators so the differences mainly lie in cost and manufacturing [28]. After comparing all of the materials and talking to companies about manufacturing, it was decided to use a two part epoxy such as the EP31 from Master bond for the electrode seal at the face and a glass seal for the pins at the back of the probe.

Once an appropriate seal for the probe was chosen, the team focused on ways in which the probe could be physically connected to the pipe. For the design, the team had to ensure that the following criteria was fulfilled: the probe needs to sit safely and securely inside the pipe and the probe needs to be easily removable from the standard 2” NPT access fitting. A threaded hollow

plug was chosen for this task, as they are readily available off the shelf and are made to be used with the access fitting systems, allowing for easy installation and removal while the pipe is in operation, as well as providing a solid foundation to ensure the probe is securely fastened to the pipe. This design choice ensures that the probe is able to withstand the high pressures that the probe is exposed to. The hollow plug also allows for wiring to be inserted into the access fitting and reach the probe.

III. Electrode Design and COMSOL Simulations

For the electrode design portion of this project, the multiphysics program COMSOL was utilized. Specifically, steady state electric current simulations were run on prospective designs to see if they could produce the desired characteristics of the conductivity probe. A four electrode design, consisting of a terminal, ground and two reference electrodes, was selected prior to this group's involvement of the project and was used in all simulations. This four electrode design was based on previous research done by Frank Wenner in the 1910s. Wenner's research involved embedding four electrodes into the ground at predetermined distances from each other. Of these electrodes, one was the terminal electrode supplying a known current, one was the ground electrode and two were reference electrodes. Frank Wenner found that he could measure the voltage across the two reference electrodes and calculate the resistivity of the ground using the voltage difference between the two [29]. Since conductivity is simply the inverse of resistivity, it followed logically that this four electrode design could be adapted to suit the demands of a conductivity probe

Initially, two-dimensional simulations were run on preliminary probe geometry. These 2D models were comprised of series of rectangles which were assigned different material

properties and electric boundary conditions. This model was constructed in such a way that it would loosely simulate a vertical cross section of the probe face with its four electrodes. It was determined through the use of these models that the surface surrounding the four electrodes should be non-conductive to maximize the sensitivity of the electrodes. The following image depicts the final two dimensional model generated in COMSOL.

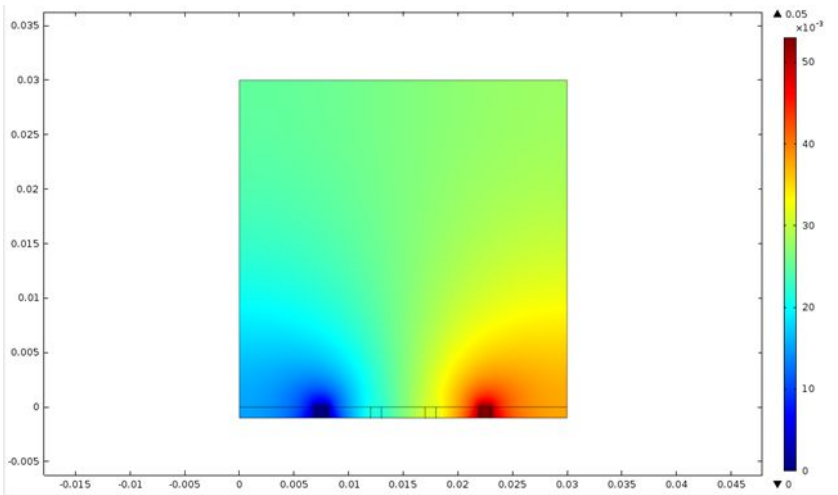

Figure 5: Final 2D electrode simulation depicting voltage distribution across probe surface

The voltage distribution across the surface of the conductivity probe was also plotted to further illustrate the sensitivity of the simulated electrode configuration. The sensitivity of the system of electrodes was considered paramount as the final probe was intended to be installed in an active pipeline. It was reasoned that this pipeline could potentially produce a substantial degree of noise in the designed probe's readings. Therefore, maximizing the sensitivity was determined to be crucial in order to ensure the operating functionality of the probe. The graph displaying the resulting voltage distribution across the probe surface when operating with 0.1 A of current follows in Figure 6.

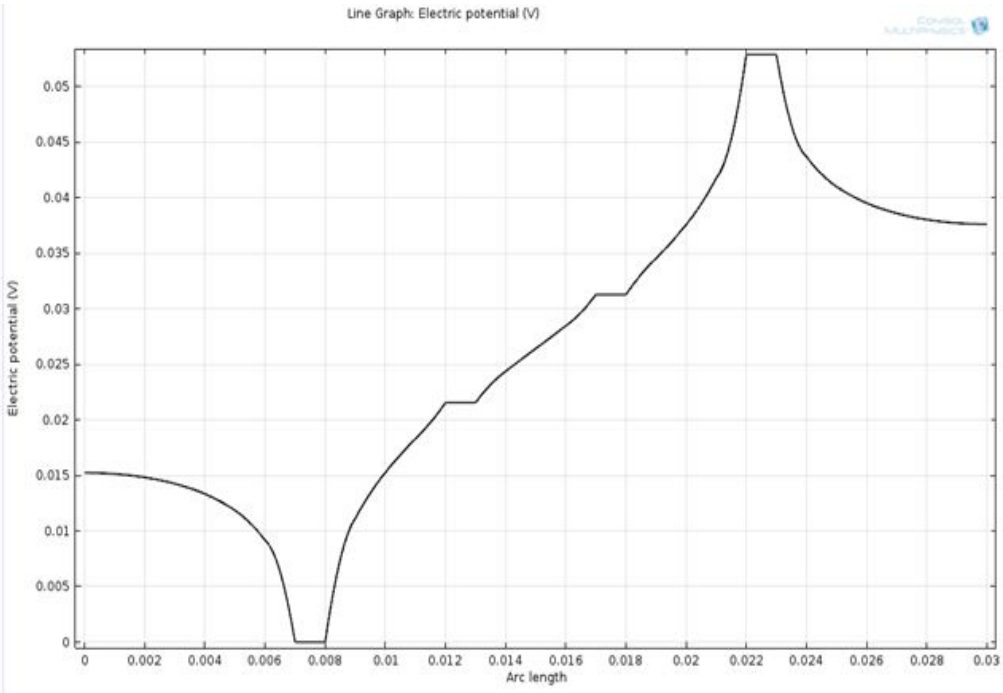

Figure 6: Change in voltage over the probe surface subjected to a current of 0.1 A

Generally, it was noted that measured voltage differences in the order of millivolts would be likely be sufficiently large enough to measure in a noisy system. Thus, since this two dimensional model was returning voltage difference which were measurable, the design process could progress.

After the relevant information was extracted from two dimensional analysis, an initial 3D model was created to determine how it differed from the two dimensional model. It was found that the voltage difference between the reference electrodes was on the order of volts instead of millivolts as it was in the two dimensional model. This was likely due to COMSOL assigning a unit width in two dimensional electrical current studies. With the understanding that the three dimensional model was generally viable, a second 3D design was developed using specific probe dimensions. This limited the maximum probe face diameter to three quarters of an inch.

When developing the three dimensional model, it was determined that the electrode sizes and spacing should be relegated to typical fractions of an inch in order to facilitate machining of the final design. With these considerations in mind, electrodes with a diameter of a sixteenth of an inch set in a probe face with a diameter of three quarters of an inch were chosen for the final probe geometry. Additionally, conductivity electrodes tend to be made with B162 rolled nickel, so this was the metal chosen for simulation purposes. These nickel electrodes were simulated set into a probe face made of glass insulation, which is typical for pipeline applications. Finally, a larger cylinder was modeled which encapsulated the probe face. This cylinder was created to simulate the fluid surrounding the probe face. An image with the final probe face geometry is displayed in Figure 7 below.

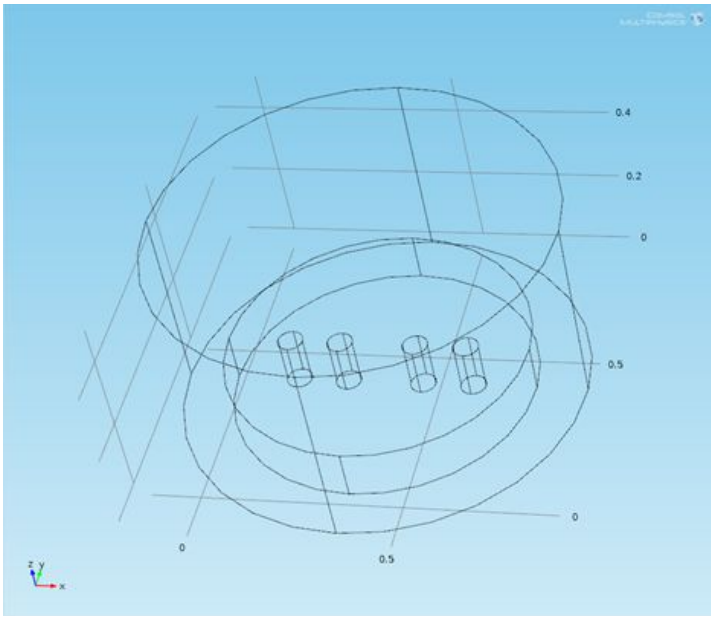

Figure 7: Final probe face geometry simulated in COMSOL

Finally, a simulation in which the probe design was subjected to a current of 0.1 A was run to ensure that the updated design was still viable was performed. The resulting voltage potential plot follows in Figure 8 below.

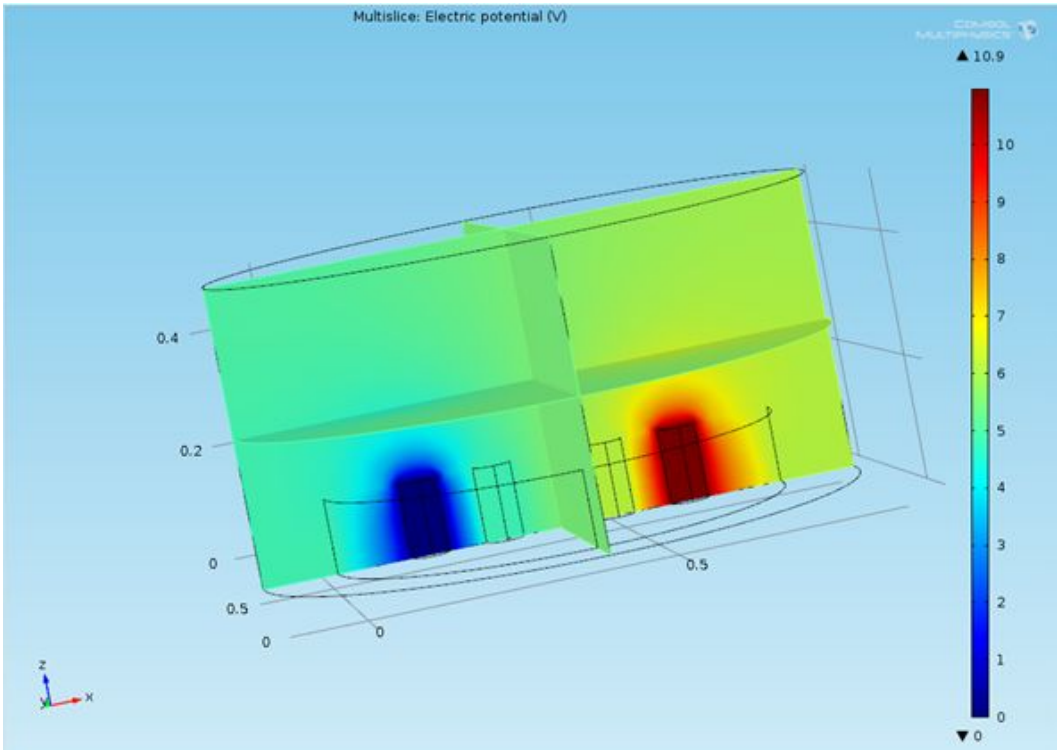

Figure 8: Voltage distribution in final probe face design when subjected to 0.1 A current

The difference in voltages across the two reference electrodes was found to be roughly 1.3 volts. This was determined to be a substantial enough difference to be measurable in a noisy pipeline while still operating with relatively low current. This was therefore chosen as the final probe face design configuration.

Using this model, a parametric array was run to determine the impact of different fluid conductivities on the voltage differences between the reference electrodes of the probe. The graph resulting from this parametric arrays follows in Figure 9 below.

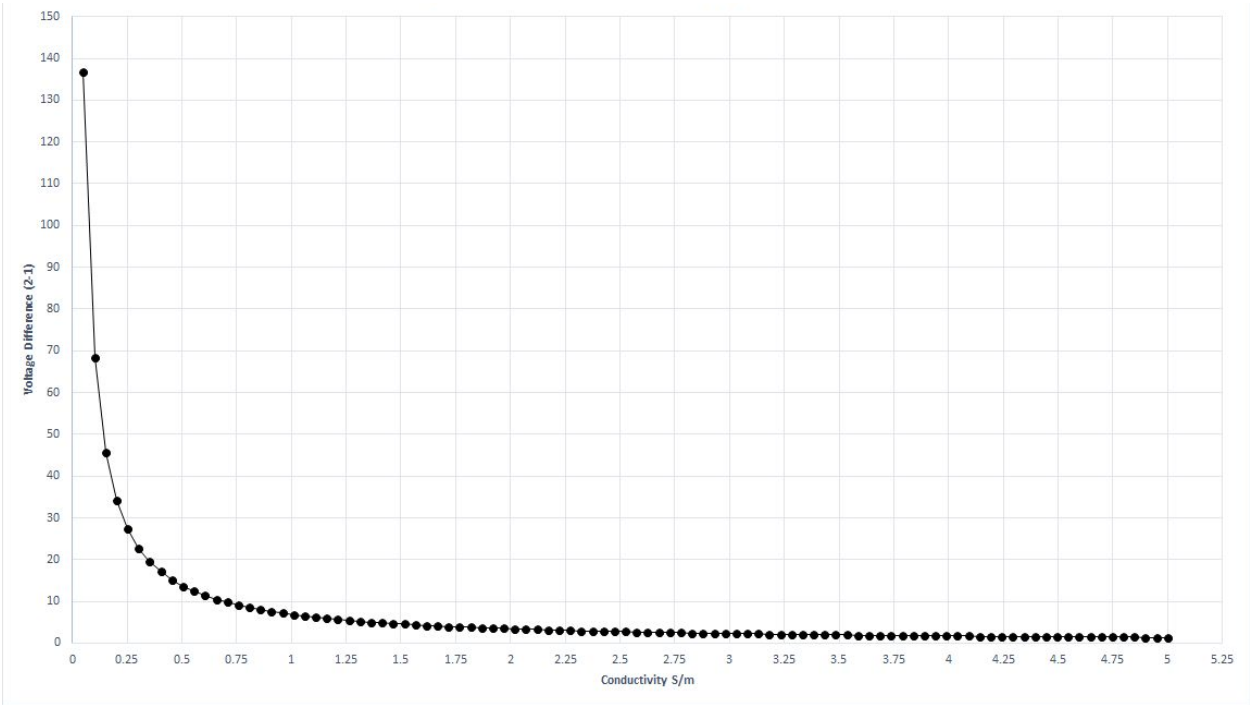

Figure 9: Voltage difference across reference electrodes when subjected to a current of 0.1 A and surrounded by fluids of varying conductivities [S/m]

This conductivity probe is expected to function in fluids with conductivities ranging from approximately 0-5 S/m since oil has a very low conductivity and salt water can have a conductivity of approximately 5 S/m. As can be seen from the graph in Figure 9, there tends to be a significant difference in the electrode voltages in fluids with conductivities substantially below 1 S/m. Conversely, the differences in voltages decrease as fluid conductivity increases.

This was determined to be desirable behavior as there is a substantial change in the voltage differences when the probe is exposed to desirable versus undesirable conductivities. Thus, if the probe is exposed to undesirable fluids, e.g. those which will facilitate corrosion, it will be readable in the form of a small voltage difference between the reference electrodes. Thus, this final probe face design was determined to be suitable overall for the purposes of the conductivity probe design.

CONCLUSIONS

Figure 10 below shows an exploded view of the probe design containing all of the design choice elements made during this project. On the front-facing end of the probe are four linearly spaced B162 Nickel electrodes. These electrodes make up the face of the conductivity sensor and will need to be sealed in a 2-part epoxy. The back-facing end of the probe will have a standard 6 pin connection sealed with glass. The probe was designed with the intent of fitting an industry standard 2” NPT access fitting with the use of a hollow plug. The body of the probe was designed to be made out of hollow ⅝” steel tubing with 0.065” wall thickness to allow for electrical transfer into and out of the probe. To allow for coupon testing in pipe segments where coupons are needed or required a cage attachment fits onto the front end of the probe with space to hold two electrically isolated coupons. The cage is designed to hold a pair of coupons while still maintaining fluid contact with the conductivity sensor on the front face of the probe. Between the cage attachment and the coupons are electrically isolating spacers made of ABS plastic to prevent galvanic corrosion. Both the probe body and cage attachment were designed to be made of 316L stainless steel. The design with the elements stated above, was tested and approved using Finite Element Analysis in SolidWorks.

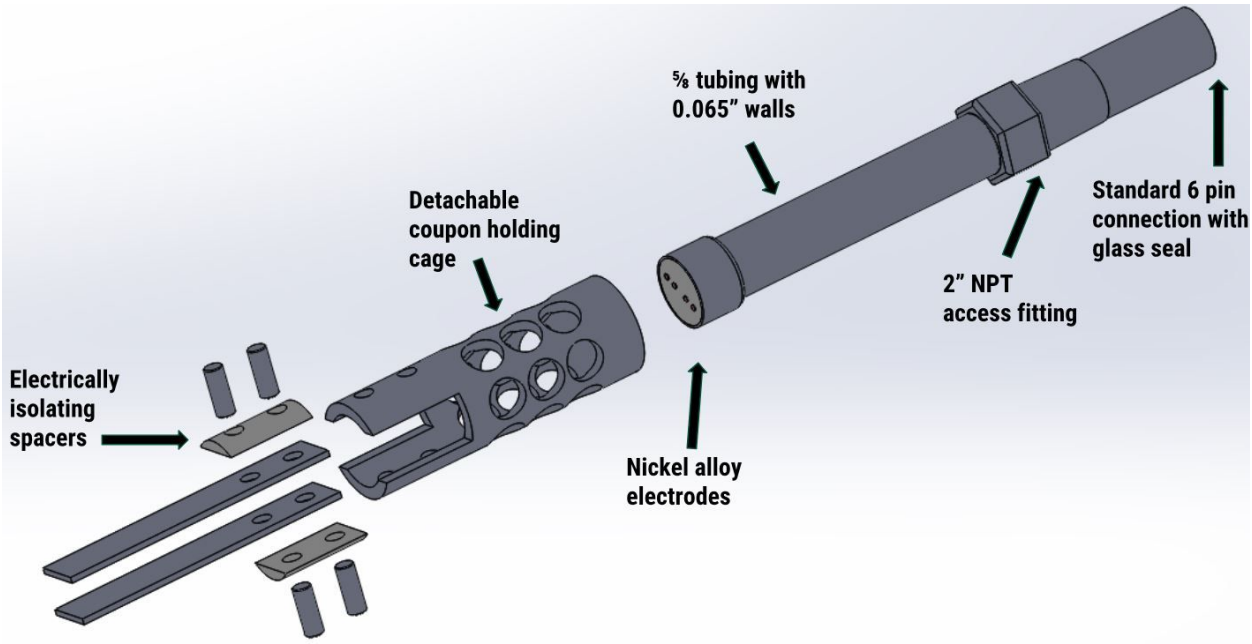

Figure 10: Exploded view of probe design with labels

PROJECT SCHEDULE

The Gantt chart which was proposed at the beginning of this project follows in Figure 11 below.

Task Name	Duration	Start	Finish	Predecessors
Probe Body Research	11 days	Mon 2/4/19	Sun 2/17/19	
COMSOL Simulation	11 days	Mon 2/4/19	Sun 2/17/19	
Seal and Electrical Isolation Research	11 days	Mon 2/4/19	Sun 2/17/19	
Combined Probe Design	16 days	Mon 2/18/19	Sun 3/10/19	1,2,3
Spring Break	6 days	Mon 3/11/19	Sun 3/17/19	4
Prototype (if possible)	16 days	Mon 3/18/19	Sun 4/7/19	5
FEA Analysis	16 days	Mon 3/18/19	Sun 4/7/19	5
Write Senior Design Report	26 days	Mon 3/18/19	Sun 4/21/19	5
Presentation Slides	11 days	Mon 4/8/19	Sun 4/21/19	6,7
Design Poster	11 days	Mon 4/8/19	Sun 4/21/19	6,7
Final Preparation and Presentation	5 days	Mon 4/22/19	Fri 4/26/19	8,9,10

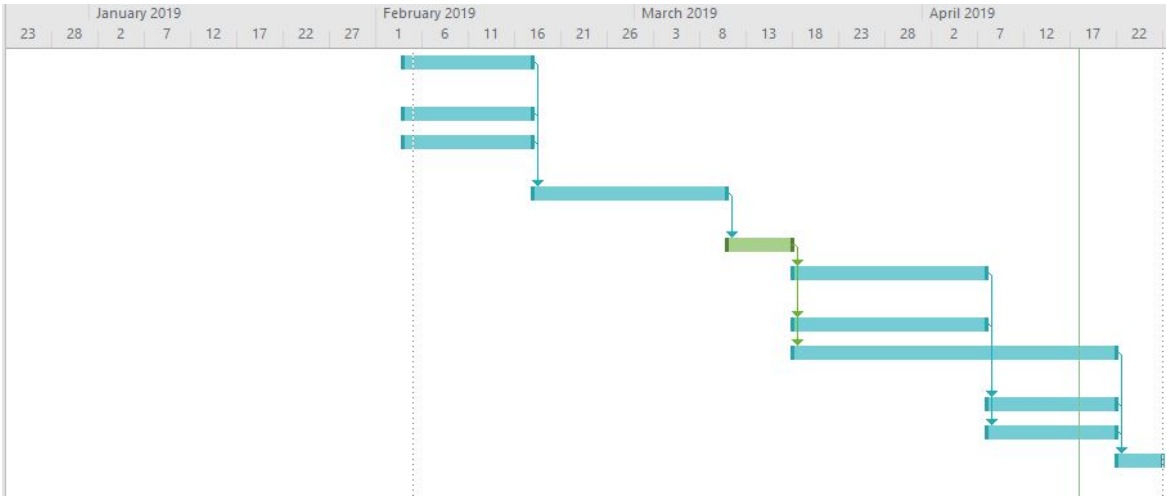

Figure 11: Proposed Gantt Chart for Conductivity Probe Project

Since the primary goal of this senior design project was to produce a well-supported conductivity probe design rather than a physical prototype, the majority of the semester was allotted for research. This included small group research at the beginning of the semester, followed by research which involved the entire team synthesizing the individual research into a coherent, unified design.

During the course of this project, the proposed schedule was generally adhered to. It was unknown at the time that the paper for this project would be worked on throughout the semester. Thus, the two weeks allotted for the paper at the end of the semester were instead incorporated earlier and FEA analysis took up the available time instead. Generally though, the project remained on track throughout the entire semester.

BUDGET

This senior design project was included in a PHMSA grant for designing a low-powered, wireless system of conductivity probes. Therefore, this project was backed with a substantial budget. However, since this project primarily involved research and initial design, this budget was not used during the course of the semester. It was determined that a cost of roughly a thousand dollars per probe was reasonable, given the PHMSA grant. Initial estimates given by Metal Samples indicated that the first iteration of the conductivity probe design would cost about $2000 for the first probe. However, each successive probe would cost substantially less: around $700 per probe. Thus, as long as five probes minimum were manufactured, this proposed design would adhere to the rough budget indicated.

Additionally, design hours were estimated amongst all team members. These hours purely were those spent in active research, and did not include class time. This estimate was collected to determine the rough amount which would be spent in order to pay the participating students for their research efforts. Assuming an average salary of roughly $15/hour and approximately 320 hours spent in research, this would add a total of $4,800 to the overall cost of this senior design project which would need to be figured into a cost estimate. This figure was determined purely as an academic exercise in an attempt to better illustrate realistic project costs.

RESOURCES

Consultants:

Dr. Matthew Cullin	Primary Faculty Advisor
Dr. Raghu Srinivasan	Co-Faculty Advisor
Dr. Todd Petersen	Electrical Engineering Advisor
Dr. Jifeng Peng	Senior Design Instructor
Dave Mulligan	PHMSA Consultant
Cosasco	Industry Reference
Metal Samples	Industry Reference

Industry Standards:

American National Standards Institute (ANSI)

American Petroleum Institute (API)

American Society of Mechanical Engineers (ASME)

National Association of Corrosion Engineers (NACE)

REFERENCES

[1] Revie, R. W., and Uhlig, H. H., 2008, Corrosion and Corrosion Control: An Introduction to Corrosion Science and Engineering, Wiley-Interscience, New York City, NY.

[2] Rifai, Damhuji, Abdalla, Ahmed, Razali, Ramdan, Ali, Kharudin, and Faraj, Moneer. “An Eddy Current Testing Platform System for Pipe Defect Inspection Based on an Optimized Eddy Current Technique Probe Design.” *Sensors (Basel)* Vol. 17 No. 3 (2017): DOI 10.3390/s17030579. www.ncbi.nlm.nih.gov/pmc/articles/PMC5375865/

[3] Huadong, Song, Liang, Yang, Guangheng, Liu, Guiyun, Tian, Denis, Ona, Yunpeng, Song, and Shangging, Li. “Comparative Analysis of In-line Inspection Equipments and Technologies.” *IOP Conference Series: Materials Science and Engineering* 382 (2018): pp.2-5. DOI 10.1088/1757-899X/382/3/032021. iopscience.iop.org/article/10.1088/1757-899X/382/3/032021/pdf.

[4] “Magnetic Flux Leakage (MFL),” *eddyfi*, www.eddyfi.com/technologies/magnetic-flux-leakage-mfl/.

[5] Robers, M.A.,and Scottini,R. “Pulsed Eddy Current in Corrosion Detection.” Vol. 7, No.10 (2002): www.ndt.net/article/ecndt02/251/251.htm.

[6] Unknown,”What are Corrosion Coupons?” Chardon Laboratories, https://www.chardonlabs.com/resources/what-are-corrosion-coupons/

[7] Speight, J. G., 2014, “Corrosion Monitoring and Control”, Science Direct, https://www.sciencedirect.com/topics/engineering/electrical-resistance-probe

[8] Goldsmith, S., 2008, “What drives the Alaska Economy?”, Understanding Alaska, https://iseralaska.org/static/legacy_publication_links/researchsumm/UA_RS_13.pdf

[9] NACE, “Preparation, Installation, Analysis, and Interpretation of Corrosion Coupons in Oilfield Operations” National Association of Corrosion Engineers Standards, (2013), SP0775-2018-SG

[10] ANSI/NACE, “Petroleum and natural gas industries —Materials for use in H2S-containing environments in oil and gas production —Part 1:General principles for selection of cracking-resistant materials” National Association of Corrosion Engineers Standards, (2009), MR0175/ISO 15156-1

[11] ANSI/NACE, “Petroleum and natural gas industries —Materials for use in H2S-containing environments in oil and gas production — Part 3: Cracking-resistant CRAs (corrosion resistant

alloys) and other alloys" National Association of Corrosion Engineers Standards, (2009), MR0175/ISO 15156-3

[12] ASME, "Pipe Threads, General Purpose, Inch" American Society of Mechanical Engineers, (2013), B1.20.1

[13] Pipeline Safety Trust, 2015, "Pipeline Briefing Paper #2" http://pstrust.org/wp-content/uploads/2015/09/2015-PST-Briefing-Paper-02-NatGasBasics.pdf

[14] API, "Recommended Practice for Design and Installation of Offshore Production Platform Piping Systems" American Petroleum Institute, (2013), API RP 14E

[15] Cosasco, 2019, "4700 / 4700-ADJ ER High Pressure Fixed and Adjustable Probe Datasheet", from https://www.cosasco.com/documents/Datasheets/4700_ER_Electrical_Resistance_Probe.pdf

[16]Cosasco, 2018, "ER High Pressure Retrievable Probe 4705 Datasheet", from https://www.cosasco.com/documents/Datasheets/4705_ER_High_Pressure_Adj_Probe.pdf

[17]Cosasco, 2019, Sales Department Representative, private communication

[18] Metal Samples Company, n.d., "Model ER7200", from http://www.alspi.com/er7200.pdf

[19] Coorstek, 2018, "Seal Material Properties Brochure", from https://www.coorstek.com/media/1939/seal-material-properties-brochure.pdf

[20] AZO Materials, 2008, "Ceramic-to-Metal Seals – The Advantages, Benefits and Applications of Ceramic-to-Metal Seals", from https://www.azom.com/article.aspx?ArticleID=4263

[21] Druflon, n.d., "PROPERTIES OF PTFE AND SOME OTHER INSULATING MATERIALS", from http://www.druflon.com/ptfeprop.html

[22] Poly Fluoro Ltd, 2013, "PTFE vs PEEK - A Comparison of Properties", from https://polyfluoroltd.com/blog/ptfe-vs-peek-a-comparison-of-properties/

[23] SSP Seals, n.d., "PEEK Material Properties Data Sheet", from https://www.sspseals.com/pdf/peek%20SSP.pdf

[24] Complete Hermetics, n.d., "Glass-to-Metal Seals and Feedthroughs", from http://www.completehermetics.com/glass-to-metal-seals-and-feedthroughs/

[25] Drake Plastics, n.d., "Why Ryton PPS?", from https://drakeplastics.com/ryton/

[26] Solvay, n.d., “Ryton PPS - Stock Shapes”, from
https://www.solvay.us/en/markets-and-products/featured-products/Ryton-Stock-Shapes.html

[27] Master bond, n.d., “Master bond EP31 Technical Data Sheet”, from
https://www.masterbond.com/tds/ep31

[28] Omnexus, n.d., “Volume Resistivity”, from
https://omnexus.specialchem.com/polymer-properties/properties/volume-resistivity

[29] Wenner, F., “ A Method of Measuring Earth Resistivity” Bulletin of the Bureau of Standards, 12, (1916), 469-478.

APPENDIX A: Fluid Drag Force Calculations

Fluid Drag Force:

$F_d = C_d \rho A \frac{1}{2} v^2$

$F_d = Fluid\ drag\ force$
$C_d = 1.28$ *Drag coefficient for flat plate*
$\rho = 920\ kg/m^3$ *Density for crude oil (worst case scenario)*
$A = (3in)(0.5in)(1ft/12in) = 0.083\ ft^2$ *Flow contact area of* $3x\frac{1}{2}x\frac{1}{16}$ *inch coupon*
$v = 15\ ft/s$ *Max allowable flow velocity for oil pipelines*

$F_d = (1.28)\ (920\ kg/m^3)(0.083\ ft^2)(\frac{1}{2})(15\ ft/s^2)$

$F_d = 11.938\ kgm/s^2$

$F_d = 11.938\ N$

Appendix B: Safety Factor Calculation

Safety Factor:

$$SF = \frac{Material\ Strength}{Maximum\ Stress}$$

$$Material\ Strength\ of\ 316\ Stainless\ Steel = 1.7\ x\ 10^8\ N/m^2$$

$$Maximum\ Stress\ from\ FEA = 4.519\ x\ 10^7\ N/m^2$$

$$SF = \frac{1.7\ x\ 10^8 N/m^2}{4.519\ x\ 10^7\ N/m^2} = 3.8$$

Appendix C: Electrode Seal Failure

Design Pressure:

$$Design\ Pressure\ =\ Factor\ of\ Safety * Operating\ Pressure$$
$$Design\ Pressure\ =\ 1.3 * 1000\ psi$$
$$Design\ Pressure\ =\ 1300\ psi$$

Force Exerted on Electrode Tip:

$$Force\ =\ Area\ of\ Electrode\ Tip * Design\ Pressure$$
$$Force\ =\ \pi * (\tfrac{1}{32}\ in)^2 * 1300\ psi$$
$$Force\ =\ 3.988\ lb$$

Electrode Seal Bond Shear:

$$Shear\ =\ \frac{Force}{Bond\ Area}$$
$$Shear\ =\ \frac{Force}{Circumference\ of\ Electrode * Depth\ of\ Seal}$$
$$Shear\ =\ \frac{3.988\ lb}{2\pi * (\frac{1}{32}\ in) * (\frac{1}{4}\ in)}$$
$$Shear\ =\ 81.25\ psi$$

Pressure Vessel Design

Design of Mechanical Engineering Systems
ME A438

University of Alaska Anchorage
Spring 2019

Faculty Professor: Dr. Peng, Jifeng
Supervising Professor: Dr. Cullin, Matthew
Group Members: Michael Anagick, Brant Bennett, Luke Cooley, Mario Moran, Reese Hanneman

Abstract

This Senior Project is to design a pressure vessel capable of withstanding an internal operating pressure. The vessel must also be able to heat a contained liquid and maintain an internal temperature. In addition, the vessel will also be designed to house a corrosion and conductivity test probe. A steel pipe was cut and on one end was fit with a welded cap while the other end was welded to a weld neck flange that could mate with two different blind flange fittings for the required tests.

The parameters of each test were used to design the specifications behind the pressure vessel. Internal pressure dictated an initial minimum wall thickness, and then comparing that to a table of pipe schedules resulted in API 5L Grade A Schedule 40 carbon steel pipe being selected. Insulation around most of the system was used to slow the effects of heat loss through convection, a heater was selected using factors such as cost, physical size, power rating, ease of connection, etc.

A steady state thermal heat analysis was performed to verify the pressure vessel can achieve the internal temperature design requirement of 200° F. Some other design factors being considered for the pressure vessel is a pressure relief valve with max pressure relief gauge set at 1250 psi in order to accommodate the hydrostatic pressure test.

Table of Contents

Introduction 4
Project Statement 4
Scope of Project 1
Methods 1
Pipe Material and Schedule 2
Flange Selection 3
Gasket Selection 4
Heater Selection 5
Thermal Analysis 5
Heater Specifications 11
Access Fitting Selection 12
Drain / Pressure Release Selection 13
Nuts/Bolts Selection 13
Conclusion 13
Bill of Materials 17
References 18
Appendix 19
Gantt Chart 19

Introduction

Pipelines are instrumental in transporting natural gas, crude oil, and other refined petroleum products from the production wells to the refineries to storage or distribution stations. They are the most practical way to deliver oil and gas from remote producing regions to the country's more populated areas; about 70% of crude oil and petroleum products were shipped by pipeline in the U.S. in 2014. The use of pipe oil transportation started soon after the drilling of the first commercial oil well sometime in the 1860s. Currently there are more than 2.4 million miles of energy pipelines in the United States, with approximately 72,000 of those miles transporting crude oil to regional markets. When properly designed, inspected, and maintained, they provide an economical, safe, and environmentally-friendly way of transporting oil and gas over long distances.

The first pipeline built was a wooden pipeline and engineering has come a long way in the evolution of pipe material used and standard design practices to build safe and efficient pipelines. Most piping now uses carbon steel because of the beneficial effects of strength and toughness of the material. ASME created standards and constantly updates a set of design standards to assure that individuals with competent and concerned interests have an opportunity to participate in the design process.

Corrosion is a substantial concern when maintaining the integrity of a pipeline. Corrosion in a pipeline can cause degradation of the pipe material, weakening the pipe's strength. This leads to mass loss-over-time potentially resulting in cracking and failures in a pipeline. When designing and maintaining pipelines, engineers use data gathered from inside of the pipe using specialized conductivity/corrosion probes to better understand the internal conditions of their pipelines at different locations. With this data they are able perform proper maintenance and avoid pipe failures. These probes must be interchanged from time to time to allow for new test coupons or probes to be fit. The purpose of this project is to design a pressure vessel that is structurally sound to use as a pipeline simulation for the testing of a newly designed conductivity/corrosion probe.

Project Statement

The primary topic of this project is to design a pressure vessel to simulate a section of pipeline. The primary objectives are designing a pressure vessel that can: accommodate a standardized conductivity/corrosion probe, withstand an internal pressure of 1000 psi, and have the ability to heat up to an internal temperature of 200° F while the pressure vessel is full of water and with the external conditions ranging anywhere between –20° F to 100° F.

Scope of Project

The objective of this project is to design a pressure vessel model that simulates a section of pipeline carrying oil. This pressure vessel will be modeled to withstand an internal pressure of 1000 psi and an internal temperature of 200° F while maintaining the integrity of the vessel with external conditions ranging from -20° F to 100° F. The model will also be able to house a standard conductivity probe. In order to produce an internal temperature of 200° F, the pressure vessel design will incorporate a heater within the vessel to heat the simulation liquid. The heater will be able to adequately heat the system between the limits from temperatures as low as -20° F up to and maintaining 200° F. The vessel design will also incorporate a pressure release valve. A thermal analysis will be performed on the model via SolidWorks to support the design decisions and illustrate how the design will perform. Both tests will be performed individually. The vessel must be able to withstand an internal pressure of 1250 psi while undergoing a hydrostatic pressure test. In a separate test, the contents of the test vessel must be heated up to and maintained at 200º F while experiencing external temperatures as low as -20º F. A tangible prototype will not be required due to time and material shipping constraints.

Methods

Upon initial consideration of the vessel, and how it would be deployed in a real-world working environment, considerations needed to be made for how the vessel would be laid out. The requirement of incorporating a test probe and a heater into a 6-in. nominal pipe suggested that the vessel would generally have a long, skinny profile. It was then determined that attaching a welded flange to one end of the pipe would allow for interchangeable heater/pressure blind flange configurations to be bolted to the welded flange, while preserving the ability to inspect, service, and maintain the probe and the interior of the vessel. The opposite end of the pipe

It became obvious that there were two reasonable orientation options for the vessel; vertical, and horizontal. Initially, it was theorized that a vertical orientation might allow for more even heating of the fluid contents, due to the convection effect in a tall column of water. However, this would have required that access to the flange and heater would be positioned underneath the vessel, making it very difficult to install/adjust/interchange the heater, as well as fill/drain the vessel. Because of these considerations, it was decided that a horizontal orientation would be ideal.

Pipe Material and Schedule

The next step was to determine the material and wall thickness of the pipe, given an internal operating pressure of 1000 psi and a nominal pipe size (NPS) of 6 in. API 5L carbon steel was chosen, shown in Figure 1, as it is a commonly used material for transportation of gas, water, and oil due to its variety of grades, resistance to crack propagation and relatively low cost. Grade A was selected because it had a sufficient minimum yield strength when considering the internal operating pressure. The minimum nominal wall thickness was calculated using an equation for nominal wall thickness of straight sections of steel pipe [1]:

$$t_n \geq t + A \tag{1}$$

where

t_n = nominal wall thickness (psi)
t = pressure design wall thickness (in.)
A= sum of allowances for threading, grooving, corrosion, and erosion.

The value of A is zero for the design, as there is no threading or grooving on the piping that would not be reinforced, and the effects from corrosion and erosion are negligible. The pressure design wall thickness, t, is calculated using equations:

$$t = \frac{P_t * D}{2 * S} \tag{2}$$

$$S = F * E * S_y \tag{3}$$

where

P_t = internal design gage pressure (psi)
D = outside diameter of pipe (in.)
S = applicable allowable stress value (psi)
F = design factor based on nominal wall thickness
E = weld joint factor
S_y = specified minimum yield strength of the pipe (psi).

Using values

P_t = 1000 psi (internal operating pressure)
D = 6.625 in. ([2])
F = 0.72 (Sec. 403.2.1 [1])
E = 1.00 (Table 403.2.1-1 [1])
S_y = 30,000 psi (API 5L Grade A Carbon Steel [1])

the calculated minimum nominal wall thickness was found to be 0.1534 in. Rounding up to the nearest common pipe schedule wall thickness, it was determined that Schedule 40 pipe would be the minimum requirement which has a wall thickness of 0.280 in. [2].

Figure 1 – 6-in. NPS, Schedule 40, API 5L Grade A Carbon Steel

Flange Selection

The internal pressure test was the biggest constraint when deciding what type of flange should be attached to the pipe. Upon the suggestion from BP Piping Engineer Kyle Emery, a weld neck style flange, shown in Figure 2, was chosen because it was considered the industry standard for a pipe undergoing similar conditions. Each blind flange configuration could then be bolted to the welded flange for each separate test. When considering the internal pressure of 1000 psi and the external/internal temperature requirements, a 600-class flange is the smallest classification that can safely handle the pressure/temperature requirements from Table II-2.1.1 [3].

A center bore hole less than 2.5 in. in diameter is allowable in the back of a blind flange with a 6-in. NPS. Threads in the counter bore shall be chamfered to the diameter of the counter bore at an angle of approximately 45° with the axis of the threads. The counter bore and chamfer shall be concentric with the thread [3]. This information allows each blind flange to have a 1 ¼” NPT and ½” NPT threading drilled center bore into the back of each of the blind flange connections for the heater and hydrostatic test respectively, while maintaining the set standard.

Figure 2 – Class 600 Weld Neck Flange

Gasket Selection

Spiral Wound Gasket Specifications
Temperature Limits of Common Metals

Material	Minimum °C	Maximum °C	Abbreviation		Guide Ring Colour Code per ASME B16.20
304 SS	- 195	760	304		Yellow
304L SS	- 195	760	304L		No Colour
316 SS	- 100	760	316		Green
316L SS	- 100	760	316L		Maroon
321 SS	- 195	760	321		Turquoise
Carbon Steel	- 40	540	CRS		Silver
INCOLOY® 800	- 100	870	IN 800		White
INCOLOY® 825	- 100	870	IN825		White
INCONEL® 600	- 100	1,090	INC 600		Gold
INCONEL® 625	- 100	1,090	INC 625		Gold
INCONEL® X750	- 100	1,090	INX		No Colour
MONEL® 400	- 130	820	MON		Orange
Nickel 200	- 195	760	NI		Red
Titanium	- 195	2,000	TI		Purple

Figure 3 - Spiral Wound Gasket Specifications

Carbon steel operating at the temperature range defined by the temperature test are within the range of tolerance and can therefore be selected from the chart below based off of the flange classification and external temperatures the vessel will be expected to experience.

Gaskets in accordance with ASME B 16.20,
flanges according ASME B 16.5, measurements in inch
Gasket Type CG/CGI

NPS	OD of Sealing Element Class 150 300 400 600	OD of Sealing Element Class 900 1500 2500	d2 ID of Sealing Element Class 150	d2 300	d2 400	d2 600	d2 900	d2 1500	d2 2500	d4 OD of Centering Ring Class 150	d4 300	d4 400	d4 600	d4 900	d4 1500	d4 2500
1/4	7/8	-	1/2	1/2	1/2	1/2	-	-	-	1 3/4	1 3/4	1 3/4	1 3/4	-	-	-
1/2	1 1/4	1 1/4	3/4	3/4	3/4	3/4	3/4	3/4	3/4	1 7/8	2 1/8	2 1/8	2 1/8	2 1/2	2 1/2	2 3/4
3/4	1 9/16	1 9/16	1	1	1	1	1	1	1	2 1/4	2 5/8	2 5/8	2 5/8	2 3/4	2 3/4	3
1	1 7/8	1 7/8	1 1/4	1 1/4	1 1/4	1 1/4	1 1/4	1 1/4	1 1/4	2 5/8	2 7/8	2 7/8	2 7/8	3 1/8	3 1/8	3 3/8
1 1/4	2 3/8	2 3/8	1 7/8	1 7/8	1 7/8	1 7/8	1 9/16	1 9/16	1 9/16	3	3 1/4	3 1/4	3 1/4	3 1/2	3 1/2	4 1/8
1 1/2	2 3/4	2 3/4	2 1/8	2 1/8	2 1/8	2 1/8	1 7/8	1 7/8	1 7/8	3 3/8	3 3/4	3 3/4	3 3/4	3 7/8	3 7/8	4 5/8
2	3 5/8	3 5/8	2 3/4	2 3/4	2 3/4	2 3/4	2 5/16	2 5/16	2 5/16	4 1/8	4 3/8	4 3/8	4 3/8	5 5/8	5 5/8	5 3/4
2 1/2	3 7/8	3 7/8	3 1/4	3 1/4	3 1/4	3 1/4	2 3/4	2 3/4	2 3/4	4 7/8	5 1/8	5 1/8	5 1/8	6 1/2	6 1/2	6 5/8
3	4 3/4	4 3/4	4	4	4	4	3 3/4	3 5/8	3 5/8	5 3/8	5 7/8	5 7/8	5 7/8	6 5/8	6 7/8	7 3/4
3 1/2	5 1/4	5 1/4	4 1/2	4 1/2	4 1/8	4 1/8	4 1/8	4 1/8	-	6 3/8	6 1/2	6 3/8	6 3/8	7 1/2	7 3/8	-
4	5 7/8	5 7/8	5	5	4 3/4	4 3/4	4 3/4	4 5/8	4 5/8	6 7/8	7 1/8	7	7 5/8	8 1/8	8 1/4	9 1/4
4 1/2	6 1/2	6 1/2	5 1/2	5 1/2	5 5/16	5 5/16	5 5/16	5 5/16	-	7	7 3/4	7 5/8	8 1/4	9 3/8	9 1/8	-
5	7	7	6 1/8	6 1/8	5 13/16	5 13/16	5 13/16	5 5/8	5 5/8	7 3/4	8 1/2	8 3/8	9 1/2	9 3/4	10	11
6	8 1/4	8 1/4	7 3/16	7 3/16	6 7/8	6 7/8	6 7/8	6 3/4	6 3/4	8 3/4	9 7/8	9 3/4	10 1/2	11 3/8	11 1/8	12 1/2
8	10 3/8	10 1/8	9 3/16	9 3/16	8 7/8	8 7/8	8 3/4	8 1/2	8 1/2	11	12 1/8	12	12 5/8	14 1/8	13 7/8	15 1/4
10	12 1/2	12 1/4	11 5/16	11 5/16	10 13/16	10 13/16	10 7/8	10 1/2	10 5/8	13 3/8	14 1/4	14 1/8	15 3/4	17 1/8	17 1/8	18 3/4

Figure 4 – Flange Gasket Fittings

Heater Selection

Thermal Analysis

Considering the design requirement of being able to heat the liquid contents of the test vessel to at least 200° F, it was determined that some type of immersion heater would be needed. Both screw plug and bolt-on flange-mounted immersion heater configurations were considered, with the screw-plug style ultimately being chosen due to its cost and flexibility of mounting options.

The next step was to determine the power output required from the heater in order to meet the design requirements. The assumptions for the thermal design were as follows:

<u>Steady State:</u>

Faculty Advisor Dr. Cullin specified that the startup time for the test vessel (time for vessel to heat cold contents and cold vessel from minimum ambient temp to full temp) was not of concern, and therefore a transient thermal analysis was not necessary.

<u>Boundary Conditions:</u>

The given boundary conditions for the thermal analysis of the vessel, as discussed in the project statement, were as follows: an internal complete fluid temperature of 200° F, and an external

ambient air temperature of temp of –20° F. This means that the surface of the interior of the vessel was assumed to be 200° F, and the ambient air outside of the insulation and flange were assumed to be –20° F.

Heat Loss Considerations:

Considering that the vessel was to be constructed primarily out of steel components and placed in a cold environment, primary heat loss would occur through convection. The heat loss due to radiation and conduction were evaluated and considered negligible. For our thermal analysis, an assumption was made that the internal liquid would maintain a constant temperature throughout the inside of the test vessel given its steady state. 3-in. polyurethane foam was added in a clam-shell configuration surrounding the piping portion of the vessel to reduce the effects of convective heat loss. In SolidWorks, each component of the vessel was assigned a specific material, and corresponding thermal conductivity value, k. It was assumed that the assigned k values would remain constant throughout their respective materials. Finally, the last assumption was that wind had no additional effect on convection therefore only natural convection was used. Other properties that needed to be accounted for were the surface temperature of the vessel and the convective heat transfer coefficient, h, which is characterized by the shape and orientation of the vessel along with the thermophysical properties around the vessel.

Thermal Analysis and Natural Convection Coefficient, h:

The natural convection coefficient equation was derived from the Nusselt equation. The derived natural convection coefficient equation [4] can be seen below:

$$h = \frac{Nu*k}{L_c} \tag{4}$$

where

h = natural convection coefficient ($W/m^{2*}K$)
Nu = Nusselt Number
k = thermal conductivity (W/m*K)
L_c = characteristic length of geometry, (m).

L_c and k were determined from Tables 9-1 and TA-15 [4], respectively. The average Nusselt number was calculated using the equation below [4]:

$$Nu = \left\{0.6 + \frac{0.387*Ra^{1/6}}{\left[1+(0.559/Pr)^{9/16}\right]^{8/27}}\right\}^2 \tag{5}$$

where

Pr = Prandtl number

Ra = Raleigh number

The Prandtl number is a thermophysical property found in Table A-15 [4]. The Raleigh number is a ratio of buoyancy forces and product of thermal and momentum diffusivities. The Raleigh number can be calculated using the following equations below [4]:

$$Ra = \frac{g*\beta*(T_s - T_a)*{L_c}^3}{\nu^2} * Pr \tag{6}$$

$$\beta = \frac{1}{t_f} \tag{7}$$

$$t_f = \frac{(T_s + T_a)}{2} \tag{8}$$

where

g = acceleration due to gravity (m/s^2)

t_f = film temperature (K)

T_s = surface temperature of vessel (C or K)

T_a = ambient air temperature (C or K)

ν = dynamic viscosity (m^2/s).

Note: T_s and T_a can use either all Kelvin values or all Celsius values because Kelvin has the same amplitude as Celsius so the difference whether in Kelvin or Celsius will not affect the outcome of heat loss because the amplitude difference of Kelvin and Celsius will be the same.

From Equations 4, 5, and 6 it is apparent that since h is reliant on Nu, and Nu is dependent on Ra; h is ultimately reliant on T_s, which can be calculated through the heat loss equation for heat conduction in cylinders [4]:

$$Q = \frac{(T_1 - T_a)}{R_t} \tag{9}$$

where

Q = heat loss from cylinder to surroundings (W)

T_1 = thermal temperature of center of cylinder (C or K)

T_a = ambient air temperature of surroundings (C or K)

R_t = total thermal resistance (C/W).

Note: Same Amplitude difference for temperature applies for Q as it does for Ra, therefore either all Kelvin values can be used or all Celsius values.

From Eq. 9, the total thermal resistance is calculated using properties of the materials, surrounding air, and dimensions of the different materials that comprise the cylinder [4]. The thermal resistance equations are:

$$R_t = R_{cyl} + R_{ins} + R_{conv} \tag{10}$$

$$R_{cyl} = \frac{\left(ln\frac{r_{po}}{r_{pi}}\right)}{2*\pi*L*k_p} \tag{11}$$

$$R_{ins} = \frac{\left(ln\frac{r_{io}}{r_{ii}}\right)}{2*\pi*L*k_i} \tag{12}$$

$$R_{conv} = \frac{1}{2*\pi*r_{io}*L*h} \tag{13}$$

where

R_t = total thermal resistance (C/W)
R_{cyl} = thermal resistance of pipe (C/W)
R_{ins} = thermal resistance of insulation (C/W)
R_{conv} = thermal resistance from convection (C/W)

r_{po} = outer radius of pipe (m)
r_{pi} = inner radius of pipe (m)
L = total length of cylinder of pressure vessel (m)
k_p = thermal conductivity of pipe material (W/m*K)

r_{io} = outer radius of insulation (m)
r_{ii} = inner radius of insulation (m)
k_i = thermal conductivity of insulation material (W/m*K)

Even though the surface temperature of the cylinder isn't apparent in Eq. 9, it can be calculated after Q is solved by subtracting the ambient air temperature and ambient air thermal resistance from Eq. 9 itself. The reason for this is because Q will always remain the same when each layer of temperature and thermal resistance is subtracted from Eq. 9.

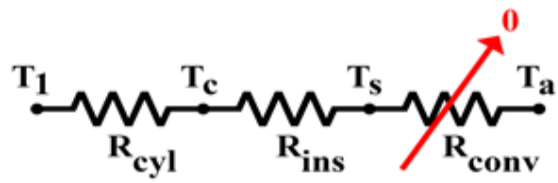

Figure 5 - Thermal Resistance circuit diagram

From Figure 5 it can be noted that when T_a and R_{conv} are canceled out Eq. 9 becomes:

$$Q = \frac{(T_1 - T_s)}{R_m} \tag{14}$$

$$R_m = R_{cyl} + R_{ins} \tag{15}$$

where

R_m = total thermal resistance of materials.

Further manipulation of Eq. 14 results in a formula for T_s of the vessel which is:

$$T_s = T_1 - (Q * R_m) \tag{14}$$

As mentioned, h is dependent on the Nusselt number which is dependent off the Raleigh number. The Raleigh Number is dependent off the film temperature, which was the average of the surface temperature of the vessel and the ambient air temperature. From Eq. 14 the surface temperature became dependent on the heat conduction loss in a cylinder, Q. From Eqs. 9-13, it is evident that Q is dependent upon h through the thermal resistance from convection, R_{conv}. Therefore, the dilemma presented is a loop of dependency of thermal values and equations that can never be calculated on paper due to h and T_s never having an actual value. An iterative process using SolidWorks helped solve this loop. The iterative process consisted of an initial calculation of Ra using a surface temperature of 200º F in Eq. 6. Once Eq.6 was calculated, h was determined from the Nusselt number. This h value was then applied into the thermal analysis of SolidWorks which gave a different T_s value than the initial value of 200º F. The new T_s value was a lot lower, being closer to the ambient air temperature of –20º F rather than the initial T_s value of 200º F. The reason for this difference was that SolidWorks accounted for the material properties of k which brought the actual T_s value to a more realistic number. The h value was still off due to a high initial T_s, so the new Ts value from SolidWorks was plugged back into the derivation of Eq. 4 which resulted in a new h value to be plugged back into SolidWorks to get a new T_s value. After several iterations, the h value and the surface temperature converged to a point where both values stopped deviating from previous values. The final converged value of h was 4.1944 and

the final T_s of the pressure vessel was –13º F. Once the values of h and T_s, converged, a power output was found by running a simulation in SolidWorks with the given h, k, and T values.

For an accurate thermal analysis to be performed a complete model of the test vessel was built in SolidWorks, using the parts and specifications of the components listed.
The visual results of this steady-state thermal analysis can be seen in Figure 6, with temperatures mapped in temperature (Kelvin):

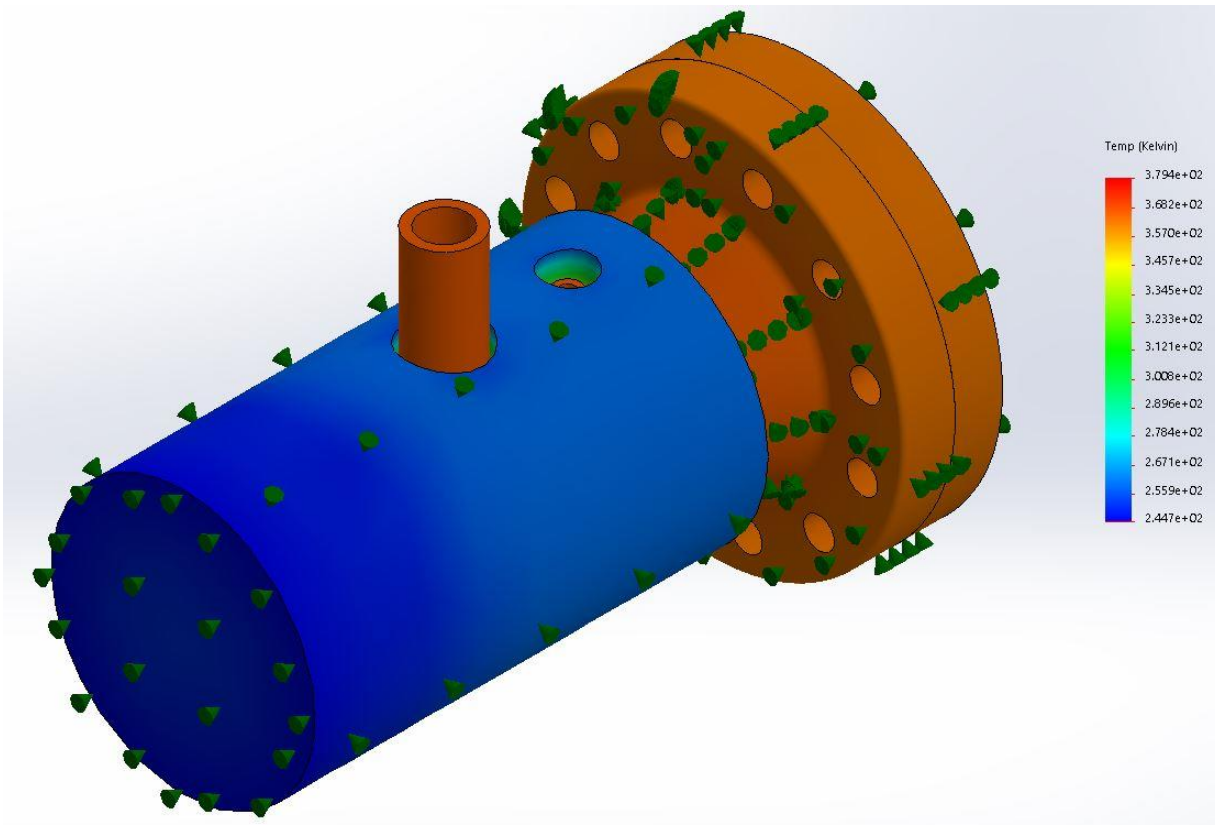

Figure 6 – Thermal Analysis of Test Vessel with Insulation

The numerical results of this thermal analysis showed that a heater with power output of at least 210 W was required to maintain the liquid's internal temperature of 200º F with an ambient temperature of –20º F, given the specific vessel design, and components with their respective material properties. This required power output for a heater was significantly higher in SolidWorks then the heat loss conduction power calculation because heat loss through the flange in SolidWorks was taken into account as opposed to heat loss through the cylinder being the only component taken into account in the equation.

In addition to the power requirements of the heater, several other geometrical and practical requirements presented themselves. It was desired that the heater be able to be powered from a 120 V power supply, so that a simple wall outlet and extension cord would be adequate to run

the test vessel's heater. It also became obvious that an integrated thermostat would be extremely helpful, as it would drastically simplify the operation of the test vessel by allowing the operator to set a desired temperature and be done, opposed to manually regulating the temperature and power application. Because of the very reasonable chance the test vessel would be operated outdoors, it was desired that the heater's thermostat be enclosed in a housing that would protect it from the ambient outdoor environment, i.e., be rated to withstand any rain, snow, dust, and other environmental conditions that could be expected.

The heater also had some geometrical restrictions, due to the specific design of the pressure vessel. Since the test probe would be situated near one end of the pipe, and the heater must be inserted through the flange mounted to the other end of the pipe, with a primary risk that the heater would be too long and therefore interfere with the probe. Upon researching commercially available screw-plug immersion heaters, it became apparent that almost all of the heaters available had insertion lengths far too long for this application, while also being generally designed for much higher power outputs. The first few heaters that were found required insertion lengths around 24 in. and above, which was far too large for the configuration of this vessel. Upon more thorough research, by calling and emailing with many commercial heater suppliers and manufacturers, a heater was found having roughly a 10 in. immersion length that would satisfy all other design requirements for this project. The selected heater will look nearly identical to the one shown in Figure 7 below:

Heater Specifications

<u>Screw Plug Immersion Heater</u>

- Manufactured custom by Gordo Sales
- Screw Plug Immersion Heater
- NPT 1 ¼ in. threads
- 304SS screw plug
- 2 elements, 10.00in. immersed length
- 0.315 in. diameter parallel element config.
- 1 in. cold length
- Conformal Coating 1-2577 end seal
- Incoloy 800 sheath
- 120V 750W
- NEMA 4 housing, type 2T, Steel,
- Standard housing gasket
- Immersion medium: Water
- UR requirement pending engineering approval.

Figure 7 - Screw Plug Immersion Heater

Access Fitting Selection

The access fitting for the test probe was one of the primary design features that the test vessel needed to accommodate. The spec for the size and type of access fitting to be used was supplied by Faculty Advisor Dr. Cullin. However, the method of attachment, positions and make and model needed to be determined. Ultimately, the test vessel was designed to fit a standard model 50 Flarweld access fitting assembly, manufactured by Cosasco. The layout and section view of this Cosasco Flarweld fitting, along with the test probe and its test coupons, can be seen in Figure 8:

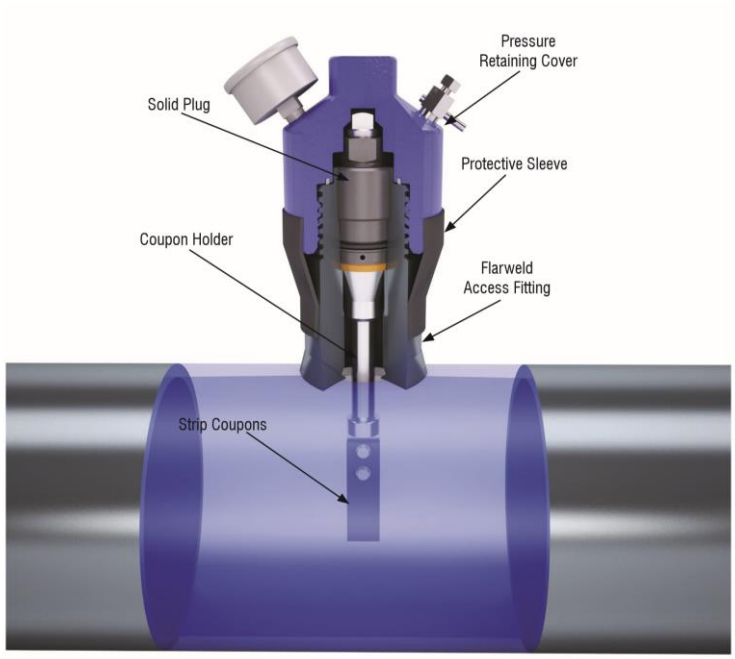

Figure 8 – Cosasco Flarweld Access Fitting Assembly Model 50

Drain / Pressure Release Selection

It was determined that placing a drain and a fitting for a pressure release valve somewhere on the vessel would be very helpful in the operation of the test vessel, to ease in the filling/draining of the vessel and protect against unwanted excess pressure buildup during each test. Adding these features required tapping holes into the section of pipe itself. When tapping holes into pipeline for branch connections, a device called an olet is commonly used in the commercial piping industry. An olet is a simple device used for joining relatively low pressure, 90° branch pipe fittings. The olets are welded into position, and one of their primary functions is to sufficiently reinforce the section of pipe that is opened. Olets come in many sub-configurations for their outlet junction, including threaded, butt-welded, press-fit, and others. For this application, the threaded olet configuration, commonly referred to by the trade name "Threadolet", was chosen. Threadolets come in two classifications, class 3000 or 6000, being designed to handle internal pressures of up to 3000 psi and 6000 psi respectively.

The design of the vessel requires 2 Threadolets to be attached at opposite sides of the pipe; one for the pressure release valve in the 12-o'clock position, and one for the drain in the 6-o'clock position. The two opposing Threadolets were selected to be class 3000 with a fitment curve for schedule 40 pipe.

Nuts/Bolts Selection

The material used for the nuts and bolts selected to join the weld neck and blind flanges was chosen to be A194 steel given the pressure and temperature limits of the vessel. This vessel requires twelve Grade B7 Stud Bolts, 1 in. in diameter, 6.125 in. length, and twelve Grade B7 Heavy Hex nuts A194 grade 2H [5].

Conclusion

In conclusion, a test vessel was designed in order to house an access fitting inside a 6-in. NPS that was able to withstand internal operating pressures of up to 1000 psi. In addition, under separate testing conditions, the vessel was designed to be able to have the inner contents heat up to and maintain a temperature of 200 F over long periods of time.

Overall, the final vessel design meets the requirements of the proposal by having a pipe large enough to fit the corrosion coupon access fitting with a 6 in. nominal pipe size, a class 600 weld neck flange was designed to be able to handle the internal pressure expected from the hydrostatic test. The hydrostatic test will be conducted through a 0.5 in. NPT threading drilled into the back of one configuration of the weld neck flange inlet, with two 3000 class threadolets fit onto opposing sides of the pipe in order to drain the water/air from the vessel during the pressure test. According to ASME standards, the class 600 flange requires 12 B7 Stud Bolts, 1 in. in diameter, 6.125 in. length, A193 Grade B7 steel with 12 Heavy Hex nut A194 grade 2H. The pipe size was

determined by analyzing the internal stresses experienced by the pressure test, using known material properties and ASME Code for Pressure Piping B31.4, the minimum wall thickness was calculated to be 0.1534 in. thick, which is most closely manufactured into schedule 40 piping of API 5L Grade A carbon steel.

The heater selected to fit into the back of the flange has more than enough power output to sufficiently heat up the vessel as determined by the thermal analysis. With the required power output determined to be roughly 200 W, the 750 W heater selected has more than enough power to overcome the heat loss expected through convection. In order to further combat the heat loss expected from the lowest temperature external testing condition, a polyurethane clamshell insulation was fitted to the outside of the vessel.

A side-view drawing of the final test vessel design with a few critical dimensions is shown in Figure 9 below:

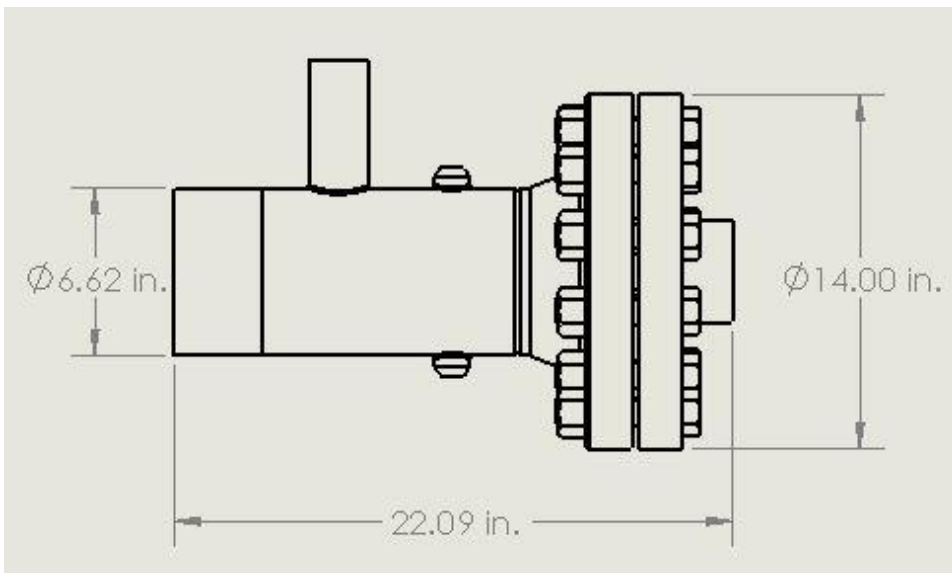

Figure 9 – Side view drawing of test vessel assembly with total length, pipe diameter, and flange diameter dimensions.

A rendering of the final test vessel is shown below in Figure 10:

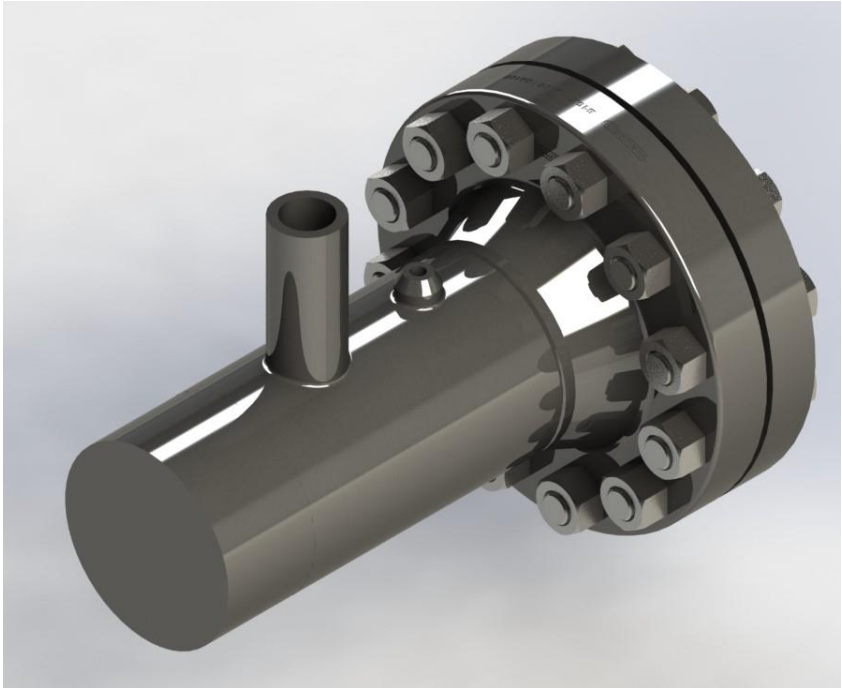

Figure 10 – Complete View of the Test Vessel, without insulation

A rendering of the final test vessel, including insulation, is shown below in Figure 11:

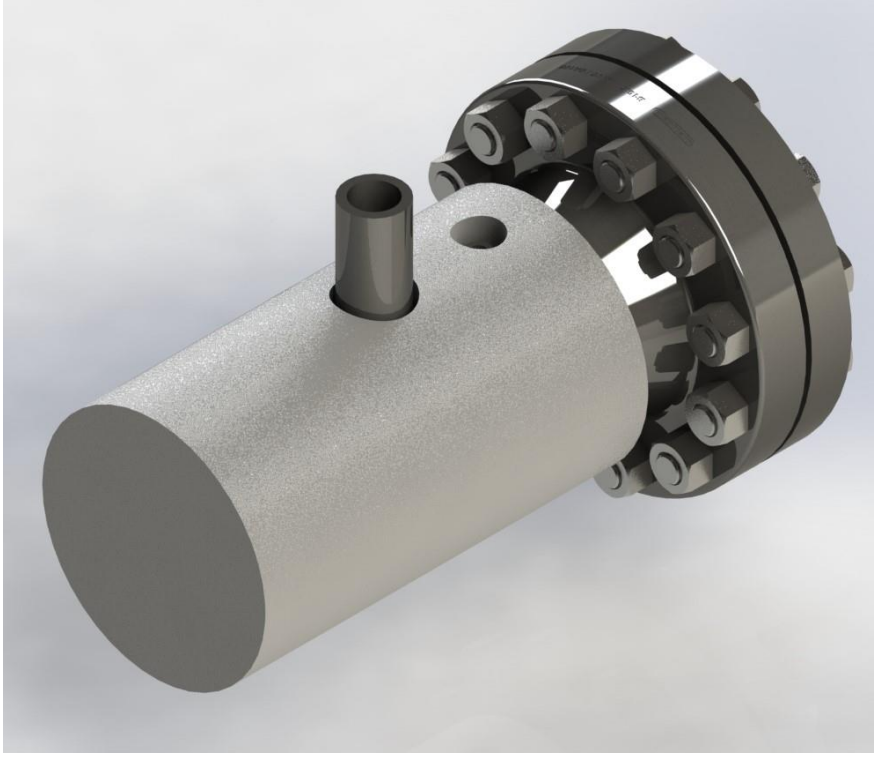

Figure 11 – Complete View of the Test Vessel, with insulation

A section-view rendering of the final test vessel, including insulation, is shown below in Figure 12:

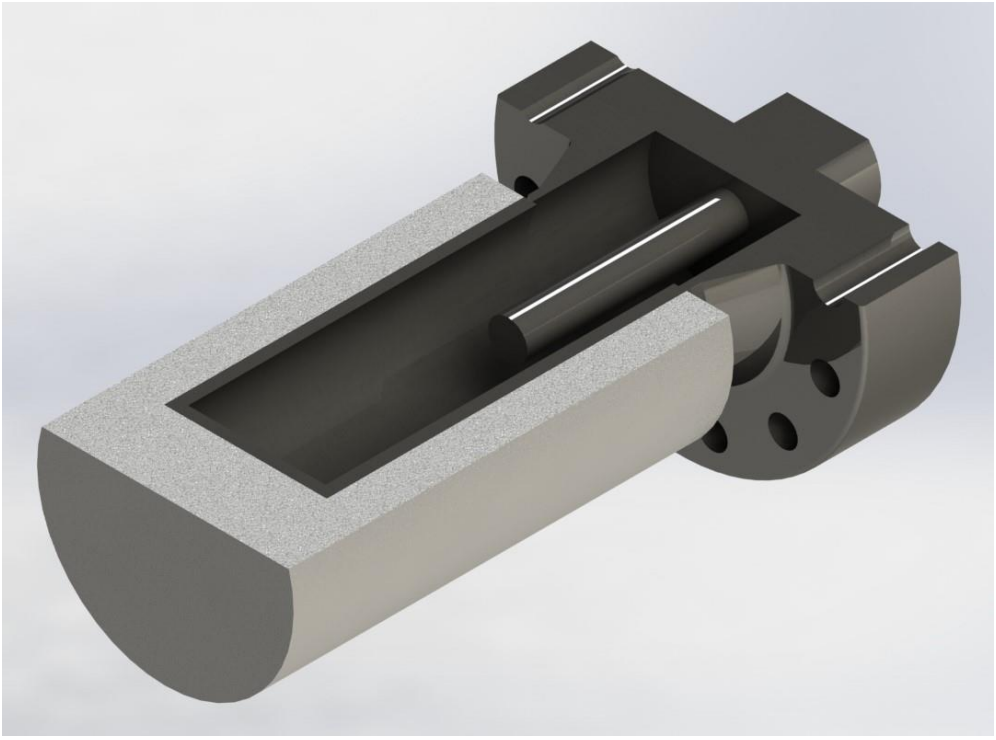

Figure 12 – Section View of the Test Vessel and Insulation

A multi-view projection drawing of the final test vessel, without insulation, is shown below in Figure 13:

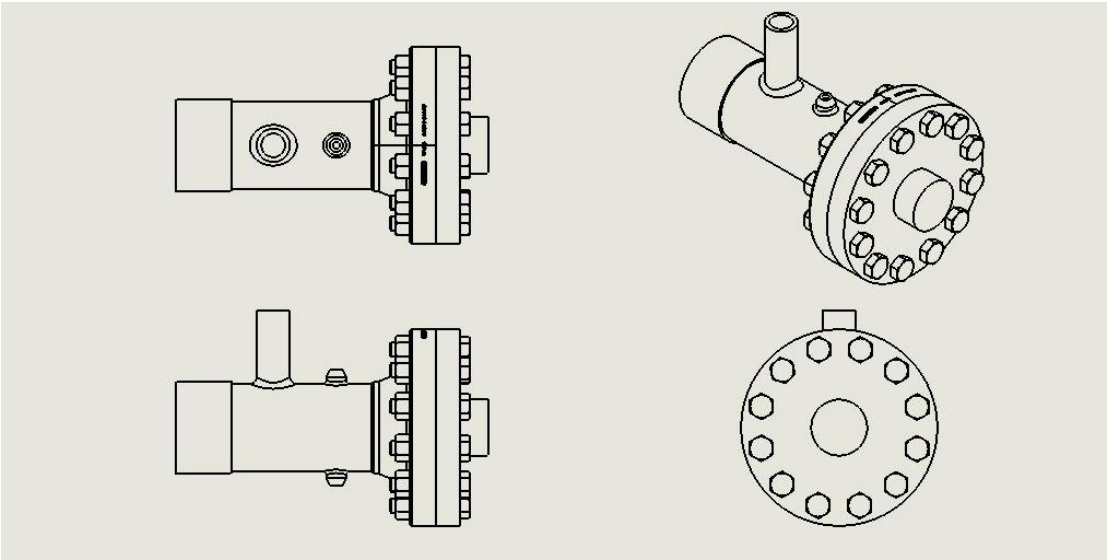

Figure 13 – Section View of the Test Vessel and Insulation

Bill of Materials

A complete list of the individual components required to build the test vessel, including component cost, is shown below in Figure 14:

Quantity	Price	Subtotal	Item	Description	Supplier	Part #
21	$ 30.65	$ 643.65	Pipe	Schedule 40, 6" nominal pipe size, 10" length (minimum purchase length 21')	Puget Sound Pipe	
1	$ 165.00	$ 165.00	Weld Neck Flange	Class 600, Weld Neck Flange, Manufactured by Weldbend	Puget Sound Pipe	14107
2	$ 195.30	$ 390.60	Blind Flange	Class 600, Blind Flange	Puget Sound Pipe	FCB3R-60
1	$ 91.04	$ 91.04	Bolts	B7 Stud Bolts, 1" diam, 6.125", A193 Grade B7, Minimum order 30	Coburn Meyers	100C625SB7
1	$ 24.08	$ 24.08	Nuts	1-8 HEAVY HEX NUT A194 GRADE 2H	Coburn Meyers	100CN2H
1	$ 92.75	$ 92.75	Cap	6" nominal pipe, Cap, Schedule 40, Manufactured by Weldbend	Puget Sound Pipe	WCBXH60
1	$ 625.00	$ 625.00	Heater	750W 1.25" NPT SS fitting, 120V supply, Incoloy element, custom 10" immersion	Gordo Sales	GG-1-0052-M1
1	$ 200.00	$ 200.00	Insulation	3" thick Polystyrene Foam Insulation, custom clam shells		
2	$ 7.60	$ 15.20	Threadolets	3000#, Anvil, 0.5" threaded-out Threadolet	Frontier Supply	TOL 3M .5
1	$ 804.00	$ 804.00	Probe Access Fitting	Flarweld Access Fitting Assembly 50, non-tee	Cosasco	50-111-0-06-K03504-10
1	$ 72.50	$ 72.50	Pressure Relief Valve	Brand Hydraulics RL50-1250 Adjustable Relief Valve 1/2 NPT/0-20 GPM/1250 PSI	Shop Cross	RL50-1250
1	$ 13.12	$ 13.12	Male to Male adapter	NPT PIPE MALE NIPPLE (STAINLESS), 316 Stainless Steel, 1/2 to 1/2	Titan Fittings	SS-5404-08-08

Estimated Project Cost	**$3,136.94**

Figure 14 – Bill of Materials

References

[1] ASME, 2016, “Pipeline Transportation Systems for Liquids and Slurries,” B31.4

[2] ASME, 2018, “Welded and Seamless Wrought Steel Pipe,” B36.10M

[3] ASME, 2013, “Pipe Flanges and Flanged Fittings: NPS 1/2 through NPS 24 Metric/In. Standard,” B16.5

[4] Cengel, Y. A. and Ghajar, A. J., 2015, *Heat and Mass Transfer; Fundamentals & Applications,* McGraw Hill, New York, NY.

[5] ASME, 2013, “Guidelines for Pressure Boundary Bolted Flange Joint Assembly,” PCC-1

Appendix

Gantt Chart

At the beginning of the project, a project schedule was outlined that assisted in the timely completion and management of tasks. This schedule was outlined in a Gantt chart, which is included below in Figure 14:

	Task Mode	Task Name	Duration	Start	Finish
1		Reseach ASME B31	4 days	Mon 1/28/19	Thu 1/31/19
2		Consultation with Cullin	5 days	Fri 2/1/19	Thu 2/7/19
3		Create Gantt Chart	5 days?	Fri 2/1/19	Thu 2/7/19
4		Spec a Heater	5 days	Fri 2/8/19	Thu 2/14/19
5		Design Pressure Vessel in SolidWorks	5 days	Fri 2/15/19	Thu 2/21/19
6		Status Report 1	5 days?	Fri 2/15/19	Thu 2/21/19
7		Handwritten Calcs for Design	5 days	Fri 2/22/19	Thu 2/28/19
8		Run FEA	10 days	Fri 3/1/19	Thu 3/14/19
9		Perform Transient Thermal Analysis	10 days	Fri 3/1/19	Thu 3/14/19
10		Status Report 2	5 days?	Fri 3/15/19	Thu 3/21/19
11		Review Design	10 days	Fri 3/22/19	Thu 4/4/19
12		Finalize Report	10 days?	Fri 4/5/19	Thu 4/18/19
13		Design Project Poster	10 days?	Fri 4/5/19	Thu 4/18/19
14		Final Project Presentation	6 days?	Fri 4/19/19	Fri 4/26/19

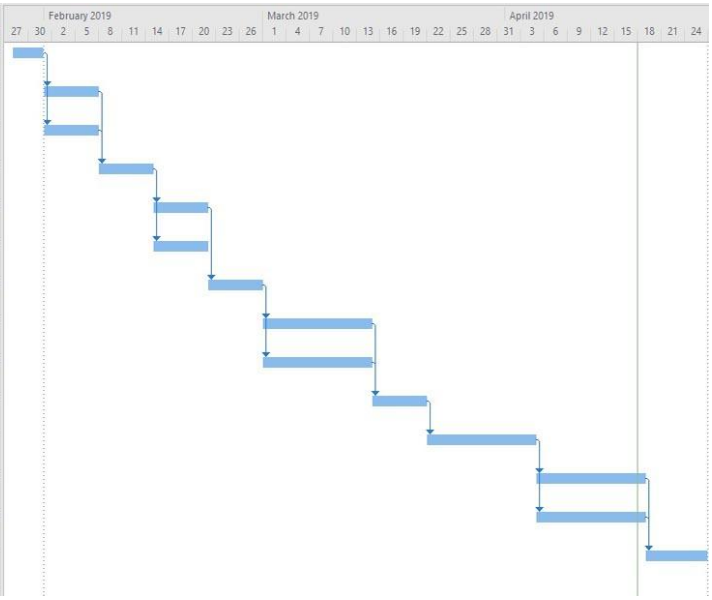

Figure 14 – Design Project Gantt Chart

Appendix 4: MSME thesis

DEVELOPMENT OF A LOW-POWERED WIRELESS SENSOR NETWORK OF CONDUCTIVITY PROBES TO DETECT THE PRESENCE OF FLUIDS THAT CAUSE INTERNAL PIPELINE CORROSION

By

Christina Fumiko Forbes, B.S.

A Thesis Submitted in Partial Fulfillment of the Requirements

for the Degree of

MASTER OF SCIENCE

in

Mechanical Engineering

University of Alaska Anchorage

August 2020

APPROVED:

Matthew Cullin, Ph.D., Committee Chair
Raghu Srinivasan, Ph.D., Committee Member
Todd Petersen, Ph.D., Committee Member
Anthony Paris, Ph.D., Committee Member
Jifeng Peng, Ph.D., Chair
Department of Mechanical Engineering
Jennifer Brock, Ph.D., Associate Dean for Academics
College of Engineering
John Stalvey, Ph.D., Acting Dean
Graduate School

ProQuest Number: 28029893

All rights reserved

INFORMATION TO ALL USERS
The quality of this reproduction is dependent on the quality of the copy submitted.

In the unlikely event that the author did not send a complete manuscript
and there are missing pages, these will be noted. Also, if material had to be removed,
a note will indicate the deletion.

ProQuest 28029893

Published by ProQuest LLC (2020). Copyright of the Dissertation is held by the Author.

All Rights Reserved.
This work is protected against unauthorized copying under Title 17, United States Code
Microform Edition © ProQuest LLC.

ProQuest LLC
789 East Eisenhower Parkway
P.O. Box 1346
Ann Arbor, MI 48106 - 1346

Abstract

This thesis details the production of a prototype of a low-powered wireless sensor network of conductivity probes to indicate if there are fluids present in a pipeline which could cause corrosion. Currently, most methods of monitoring pipelines for corrosion require substantial power consumption or require considerable manpower to maintain the system and gather data. These systems are not ideal for use in remote locations. This is primarily due to difficulties in routing power to these locations and costs in transporting technicians. It was the aim of this project to produce a system which could be operated efficiently in these rural areas and complement existing corrosion monitoring techniques. Experiments were performed using a multiphysics simulation program and lab grade sensors to determine parameters for potential prototypes. The scope of this thesis work involved creating a prototype consisting of three different components. These were a probe with accompanying circuitry to take conductivity readings, a heating unit to simulate hot pipeline temperatures, and a sealed water test cell. These components will be combined into one system node which can then be integrated into the complete wireless sensor network.

The prototype system was constructed with a graphite-epoxy probe and an Arduino controller. This probe was determined to have a probe factor of approximately 33 m^{-1} which could be used to directly relate resistance to solution conductivity. In final tests of the prototype system, the probe was able to detect fluids of differing conductivities. This included various saline solutions mixed with oil. Mixtures of this nature are what the final probe will see when installed in an active pipeline. Thus, the probe is able to perform its desired function.

Table of Contents

Page

Title Page....i

Abstract....iii

Table of Contents....v

List of Figures....ix

List of Tables....xi

List of Appendices....xiii

Acknowledgments....xv

Chapter 1 Introduction....1

Chapter 2 Background....3

2.1 General Corrosion Background....3

2.2 Economic Impact of Corrosion....4

2.3 Forms of Corrosion....4

2.4 Internal Pipeline Corrosion....5

2.5 Multiphase Flow in Pipes....6

2.6 Methods of Preventing Internal Corrosion in Pipelines....8

2.6.1 Inhibitors....8

2.6.2 Pipeline Coatings....8

2.6.3 Pipeline Design....9

2.7 Internal Corrosion Inspection and Monitoring Techniques....9

2.7.1. In-Line Inspection....9

2.7.2. Internal Monitoring Technique Classifications....9

2.7.3. Common Internal Monitoring Techniques....10

2.8 Conductivity Measurement Theory and Literature Survey....11

2.8.1. The Double-Layer Polarization Effect....12

2.8.2. General Conductivity Measurement Theory....12

2.8.3. Two-Electrode Conductivity Cells....12

2.8.4. Four-Electrode Conductivity Cells and the Wenner Theory....14

2.8.5. Electrochemical Potential Noise....17

2.8.6. AC and DC Measurement Techniques....17

2.8.7. Electrode Materials....18

2.8.8. Water Distribution and Conductivity Measurements....19

2.9 Sensor Node Background....19

2.9.1. Powering Sensor Nodes....19

2.9.2. The Zensor™ Network....20

2.10 Background Summary....21

Chapter 3 Experimental Methods....23

3.1 Preliminary Research and Design....23

3.2 Initial Multiphysics Simulation....24

3.3 Probe Material Selection....24

3.4 Copper Probe Construction and Testing....25

3.5 Copper-Epoxy Probe Construction and Testing....25

3.5.1 Galvanostatic Test....25

3.5.2 Instant-Off and Instant-On Tests....26

3.5.3 Environmental Factor Tests....26

3.5.4 Potentiostatic Electrochemical Impedance Spectroscopy Tests....27

3.6 Graphite-Epoxy Probe Construction and Testing....27

3.7 Arduino Microcontroller....28

3.8 Heating Apparatus and Peltier Thermoelectric Generator....29

3.9. Water Test Cell....31

Chapter 4 Results and Discussion....33

4.1 Multiphysics Simulations Results....33

4.2 Copper Probe Experiment....35

4.3 Copper-Epoxy Probe Experiment....37

4.4 Graphite-Epoxy Probe Experiment....38

4.4.1 Instant-Off Tests....39

4.4.2 Probe Factor Determination....39

4.4.3 Arduino Controller Tests....40

4.4.4. Graphite Probe and Controller Test....42

4.5 Heater and Thermoelectric Generator Experiments....43

4.6 Water Cell Experiment....45

Chapter 5 Conclusion....47

References....49

Appendices....51

List of Figures

Page

Figure 1: Transfer of Electrons in the Presence of an Electrolyte....3

Figure 2: Oil and Water Dispersion Patterns....7

Figure 3: Two-Electrode Cell Circuit Approximation....13

Figure 4: Four-Electrode Cell Circuit Approximation....15

Figure 5: Proposed Undergraduate Conductivity Probe Design....23

Figure 6: Clip and Final Graphite-and-Epoxy Probe....27

Figure 7: Circuit Diagram for Arduino Controller....28

Figure 8: Modeled and Actual Heating Apparatus and Peltier Generator Setup....31

Figure 9: Liquid Test Cell Setup....32

Figure 10: 3D Wireframe Model for Multiphysics Simulation....33

Figure 11: 3D Potential Graph....34

Figure 12: Plot Displaying Difference in Reference Probe Potentials....35

Figure B-1: Graphical Representation of Table 1 Data....53

Figure B-2: Graphical Representation of Table 2 Data....53

Figure B-3: Graphical Representation of Table 3 Data....54

Figure B-4: Graphical Representation of Table 4 and 5 Data....54

Figure B-5: Graphical Representation of Table 6 Data....55

Figure B-6: Graphical Representation of Table 7 Data....55

Figure B-7: Graphical Representation of Table 8 Data....56

List of Tables

Page

Table 1: Copper Probe Galvanostatic Test Results....36

Table 2: Copper Probe Instant-Off Test Results....37

Table 3: Copper-Epoxy Potentiostatic EIS Test Results....38

Table 4: Graphite-Epoxy Probe Instant-On and Multimeter Test Results....39

Table 5: Probe Factor Determination Results....40

Table 6: Controller and Resistor Circuit Test Results....41

Table 7: Controller and Resistor Circuit Test with Lower Current Results....42

Table 8: Controller and Graphite-Epoxy Test Results....43

Table 9: Omega CN 7523 PID Settings....44

Table 10: Oil and Salt Water Test....46

List of Appendices

Page

Appendix A: Code for Arduino Microcontroller.....51

Appendix B: Graphs of Tabular Data.....53

Acknowledgments

I would like to acknowledge the Pipeline and Hazardous Materials Safety Administration for funding this project through their Competitive Academic Agreement Program and allowing me this opportunity to learn and grow professionally.

I would like to acknowledge and express my sincerest gratitude to the members of my graduate committee: Dr. Matthew Cullin, Dr. Raghu Srinivasan, Dr. Todd Petersen, and Dr. Anthony Paris. Their support, instruction, and constructive criticism have been invaluable to me throughout this process.

I would like to thank all of my professors at the University of Alaska Anchorage who supported me throughout my undergraduate and graduate career. I enjoyed every class I took, and learned more than I ever thought I was capable of understanding.

I would finally like to thank Corbin Rowe for his support throughout my academic career. Working in the prototyping lab was an incredible opportunity, and I greatly appreciate his guidance and assistance.

Chapter 1 Introduction

Corrosion is a pressing issue encountered in all industries which utilize metal components. It is the cause of a significant amount of damage in equipment and the source of considerable expense. The total annual cost attributed to corrosion in the United States is approximately 276 billion dollars [1]. Therefore, it is necessary to implement and constantly improve methods minimizing the effects of corrosion. It has been estimated that roughly 25-30% of the annual costs due to corrosion could be saved if corrosion combating practices were improved [1].

Pipeline corrosion is a considerable source of expense in the oil and gas industry. Pipes must be either repaired or replaced when damaged by corrosion. This can necessitate temporary shutdown of the pipeline [2]. Corrosion can also affect the condition of the product in the pipeline, and can contaminate it with the byproducts of the corrosive process. Additionally, ruptures and leaks can impact the health and safety of individuals located near the pipeline and their environment [2]. Internal corrosion, in particular, is a pressing issue in the oil and gas industry. The interior of pipelines are routinely exposed to corrosive substances during operation which can cause the inside surface to deteriorate. However, this kind of corrosion can be difficult to detect since it is not readily visible.

Currently, there are many methods of combating the effects of internal corrosion and even preventing it before it occurs. However, these methods all require substantial power consumption or manpower. In rural areas particularly, these are resources which come at a high cost. Power is difficult to provide in rural areas due to the distance from power plants. Manpower has to be transported to these remote locations, and transportation has to be factored into cost assessments.

The goal of this thesis work was to determine a cost-effective prototype probe node to identify corrosive conditions inside pipelines for use in these remote areas. This node would be incorporated into a wireless system to monitor the interior of pipelines for corrosive conditions

while operating with minimal power consumption. It was designed to consist of a sensor with a microcontroller, a heating unit to simulate the hot siding of a pipeline, and a water cell to simulate a pipeline in operation. During the course of this work, the elements of this prototype node were created and tested. In the future, it will be incorporated into the desired wireless system as a power-efficient, low-maintenance means of identifying corrosive conditions in pipelines.

Chapter 2 Background

2.1 General Corrosion Background

Metals are widely utilized due to their desirable mechanical properties. However, metals are not mined in a pure state. Instead, these mined ores must be processed using substantial amounts of energy. In this way, alloys with the necessary properties for the desired application are produced. When metals are mined, generally they exist in a stable, oxidized state in which they possess relatively few electrons. They are provided with more electrons and become less stable upon purification. Whenever an electrolyte is present, the metal's additional electrons can be expelled as it attempts to return to a lower energy oxidized state. Energy must constantly be expended to prevent these materials from expelling electrons and corroding. A figure depicting an example of this corrosive transfer of electrons is shown below:

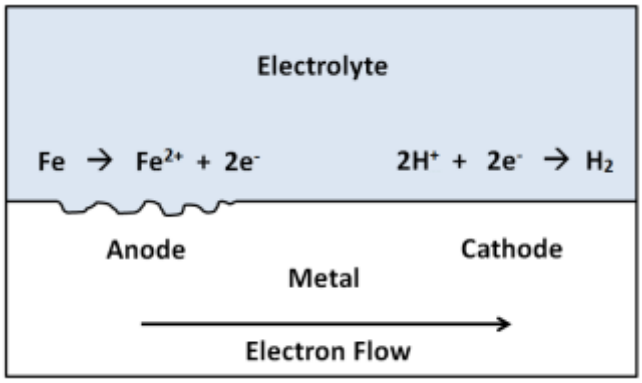

Figure 1: Transfer of Electrons in the Presence of an Electrolyte [3]

The reaction at the anode in Figure 1 illustrates the release of the iron's electrons in the presence of an electrolyte. In the figure, the anode and cathode occur on the same piece of metal; however, they can also exist as separate structures. There are different corrosive reactions which can occur at the cathodic site during this transfer of electrons [3]. In figure 1, a hydrogen evolution reaction in the presence of an acidic solution is depicted [3]. Other possible forms of cathodic

reactions include oxygen reduction which can occur in acidic, basic, or neutral solutions, and hydrogen evolution in neutral water [3].

Oxidized metals have undesirable mechanical properties. When structural components revert to their oxidized state, they can often fail due to reduced elasticity and load bearing capacity. To maintain the desired structural properties, these metal alloys must not be exposed to conditions in which this electron transfer can occur.

2.2 Economic Impact of Corrosion

The substantial costs due to corrosion were illustrated in a 2019 study by Koch et al. [1]. These costs were attributed to corrosion preventing techniques and repairing damages due to corrosion. The study posited that more than a quarter of the total costs due to corrosion could be eliminated if proper corrosion preventing techniques were utilized. As of 2019, in the United States, there were 528,000 km of natural gas pipeline, 119,000 km of crude oil pipeline and 132,000 of hazardous material pipeline [1]. The cost to equip these pipelines with anti-corrosion technology and to repair the effects of corrosion was about 13 billion dollars [1]. There are many factors which impact the cost of corrosion. Some of these are government regulations, the cost of developing techniques to prevent corrosion, how hostile the environment is, and delaying maintenance [2]. Companies have to allocate considerable funds for preventative maintenance and over-designing in an attempt to combat corrosion before it occurs [2]. Controlling these costs after the fact can be costly and the difficulties arising from corrosion can be hard to predict. Preventing corrosion before it occurs is generally the most fiscally responsible option.

2.3 Forms of Corrosion

There are many forms of corrosion. Corrosion rates can be impacted by different factors including environmental conditions, temperature, velocity of fluids, and stress [2,3]. Corrosion can also manifest in many ways. Combinations of different forms of corrosion can occur simultaneously

in a single location [3]. For these reasons, it is difficult to classify corrosion in simple categories. However, in an attempt to classify corrosion distinctions have been made. Corrosion is generally characterized by the physical appearance of the material being corroded, the properties of the fluid causing the corrosion, and the particular kind of reaction which is occurring [2].

There are two forms of corrosion called sweet corrosion and sour corrosion. Sweet corrosion is corrosion which occurs when carbon dioxide is exposed to water and results in the production of carbonic acid [3]. This kind of corrosion is very common in oil and gas pipelines [3]. Sour corrosion, on the other hand, results when hydrogen sulfide is exposed to water and produces sulfuric acid [3]. Sour corrosion causes pipe metals to become more brittle [3]. Oxygen amplifies the effects of sweet and sour corrosion and will react with metal oxide byproducts [3]. This is particularly problematic as it is difficult to isolate most structures from oxygen.

Another form of corrosion which must be considered while designing metallic parts is galvanic corrosion. Galvanic corrosion occurs when two different metals with different electronegativities come into direct electrical contact [3]. Other forms of corrosion include crevice corrosion, erosion corrosion, microbiological corrosion, and stress corrosion [3]. These forms of corrosion are distinguished from each other by their physical appearance. The appearance of corroded metal is critically studied in the case of pipeline failure to prevent future occurrences of the corrosion form [2].

2.4 Internal Pipeline Corrosion

Pipelines are used to transport many different substances such as the desired product, impurities, and byproducts generated during production. Examples of these substances include crude oil, natural gas, fuel gas, sour gas, and water of varying salinities [4]. These different fluids have different properties and produce corrosive effects to varying degrees. Crude oil is one of the least corrosive of these fluids. However, it is frequently accompanied by byproducts and other fluids

which are more corrosive, such as salt water. These corrosive fluids can impact the structural integrity of the pipeline interior.

In a report produced in Alberta by the Energy and Utilities Board, pipelines were analyzed for performance and causes of failure [4]. It was determined that internal corrosion was the cause of 57.7% of the pipeline failures experienced in Canada during the 15-year time frame in which this study was conducted [4]. The failures in this study included both leaks and ruptures. As defined in the report, a leak is a failure which results in a loss of the product being transported without affecting pipeline operation. On the other hand, a rupture is defined as a pipeline failure which results in loss of product and impacts the operation of the pipeline [4]. Ruptures can cause large scale shut downs and can have considerable associated costs [2].

2.5 Multiphase Flow in Pipes

Many pipelines utilized in the oil and gas industry are required to transport multiphase flow. This presents a problem when sections of the pipe come in contact with corrosive phases [4]. Oil and natural gas are not electrolytes and do not facilitate corrosion. However, water containing dissolved salts and other compounds, is an electrolyte and will cause corrosion. Multiple studies have been performed to identify different phases and where they occur in active pipelines. Understanding how different phases will disperse throughout a pipeline is critical to implementing effective corrosion prevention techniques. This information allows pipeline sections judged to be most susceptible to corrosion to be suitably protected. A study performed by Tan et al. used conductivity and capacitance electrodes to identify and map flow regimes in multiphase pipe flow [5]. This study was particularly interested in characterizing oil-water flow in horizontal pipes. Sketches of the dispersion patterns observed during this study are displayed in Figure 2 below.

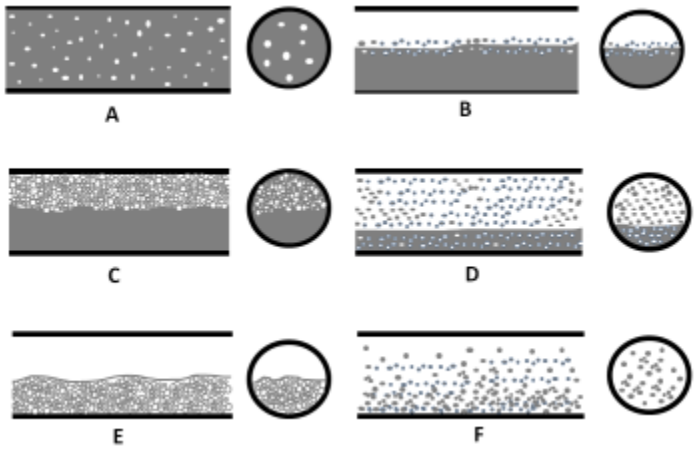

Figure 2: Oil and Water Dispersion Patterns [5]

In this image, the darker sections represent water, and the light sections represent oil. As can be seen, corrosion prevention techniques need to vary according to the dispersion of the phases throughout the pipe. For instance, in images B and E, water primarily makes contact with the bottom of the pipe. Thus, corrosion monitoring will be more critical for the lower half of the pipe which makes contact with the corrosive, electrolytic phase. Additionally, a study was performed which noted that, after water begins to form droplets in the oil phase instead of remaining a separate phase, the overall fluid conductivity drops substantially [6]. Thus, in a pipeline experiencing phase flow similar to image f, less aggressive corrosion monitoring techniques could be used.

Generally, in industrial pipelines, the amount of water in a pipeline is not allowed to exceed 30% of the total volume [6]. However, a study performed by Bruce Craig noted that this water cut could sometimes exceed 50% before notable corrosion was observed [6]. He also noted that corrosion could occur in as little as a 1% water cut. It was noted that depending on the concentration of polarizable hydrocarbons reacting with the water, corrosive tendencies could vary significantly in pipes containing identical water cut percentages [6].

2.6 Methods of Preventing Internal Corrosion in Pipelines

Some common means of preventing corrosion include adding inhibitors, adding protective coatings, cathodic protection, system design, and proper monitoring and inspection techniques, [2, 3]. Additionally, choosing materials which will not corrode in the desired environment or choosing a material which will corrode at a slower, acceptable rate can reduce the occurrence of corrosion [2, 3].

2.6.1. Inhibitors

Inhibitors are chemicals which are injected into an active pipeline in order to slow the rate of a corrosive reaction occurring within the pipeline. These inhibitors are usually silicates, chromates, or amines [2]. Inhibitors are generally only used in environments where their concentrations are easily controllable.

2.6.2. Pipeline Coatings

Pipeline coatings can be made of either organic or inorganic materials. These materials are chosen to have a resistance of approximately $10^{10}\,\Omega/\mathrm{cm}^2$ [7]. Coatings can be composed of metals, resins and waxes [7]. Metal coatings are designed with metals which are nobler than the structure they are protecting and less susceptible to corrosion. Conversely, less noble metal coatings can be chosen so that they will corrode sacrificially to protect the pipeline [2]. Inorganic coatings used to protect pipelines are generally made of ceramics, glass, carbides or cement. These inorganic materials are generally more corrosion resistant than metals [2]. Pipeline coatings can be installed before the pipeline begins operation, or with the application of current, a coating can be formed along the inside of the pipeline during operation [7]. An example of this current-induced coating would be allowing hard water in a pipeline to form a carbonate layer along the interior surface to protect the metal beneath [7]. These coatings will degenerate over time due to exposure to the product in the pipeline, trace chemicals, biological contaminants, and mechanical stress [7]. Inhibitors and coatings are especially effective when paired together in a pipeline system [3].

2.6.3. Pipeline Design

The initial design of a pipeline can impact how much corrosion it will see in its lifetime. During the designing phase, features which are more prone to corrosion should be minimized. For instance, crevices and low points should be avoided wherever possible as they are more prone to corrosive activity [2]. Low points, bends, and any pipeline sections that see decreased flow rate are particularly susceptible to corrosion since water is likely to collect in these areas. Additionally, inhibitors may not distribute properly in these areas of variable flowrate. If these pipeline features cannot be altogether eliminated, they must be constantly monitored to ensure that water is not accumulating in them.

2.7 Internal Corrosion Inspection and Monitoring Techniques

Internal corrosion inspection and monitoring techniques attempt to identify corrosive conditions inside a pipeline before it sustains damage. Inspection techniques are used to search for signs of corrosion in pipelines whenever a problem is suspected. These techniques involve the use of instruments which are not integrated into the pipeline [8]. Monitoring techniques involve instruments which are installed in a pipeline and collect data over time [8].

2.7.1. In-line Inspection

The techniques generally used for in-line inspection are magnetic flux leakage, eddy current testing, ultrasonic testing, and acoustic emission testing [9]. Sensors for these tests can be attached to pipeline inspection gauges, or PIGs, to examine the pipeline interior and relay data regarding the thickness of the pipeline walls [3].

2.7.2. Internal Monitoring Technique Classifications

Internal monitoring techniques can be categorized in many ways [8]. The first distinction which can be made is whether the technique measures general or localized corrosion. A second distinction is whether the technique is direct or indirect. A technique is direct if it monitors corrosive

effects; it is indirect if it monitors conditions which could cause corrosive effects. A third distinction is whether the technique is online, which does not require removal of the instrument from the pipeline, or offline. A fourth distinction which can be made is whether the monitoring technique can relay data in real time or if it is a lagging technique. In the case of a lagging technique, corrosive effects can only be identified after a set amount of time. A fifth distinction is whether the technique is intrusive and must be installed inside the pipeline, or non-intrusive. A sixth distinction is whether the technique is destructive or non-destructive. If the technique is destructive, the instrument which measures the corrosive effects can only be used once. If it is non-destructive, the instrument does not degrade during measurement and can be reused. The last distinction is whether the monitoring technique is based on data which is gathered from the corrosion of a probe inserted into a pipeline or the corrosion of the structure itself [8].

2.7.3. Common Internal Monitoring Techniques

There are two techniques in particular that are routinely used in oil and gas pipelines to monitor for corrosive conditions. These are mass loss monitoring with corrosion coupons and electrical resistance monitoring.

Mass loss monitoring with corrosion coupons involves attaching a coupon to a probe which can be inserted into a standard access fitting. A corrosion coupon is a piece of metal, frequently the same material as the pipeline, with a known mass. This coupon is left in an active pipeline for a set amount of time based on the expected corrosion rate. The coupon is then removed and weighed to determine the amount of mass which has been lost due to corrosion and erosion [8]. Often, multiple coupons are installed at different heights in a given pipeline section. These coupons are installed at different heights so that the coupons are exposed to the different phases present in the pipeline flow [8].

Electrical resistance monitoring utilizes a probe with an embedded metal strip made of the same material as, or similar to, the pipeline. The probe is inserted into the pipeline and the resistance across this metal strip is monitored. The resistance measured across this metal strip will increase as the metal strip loses mass and its cross sectional area decreases [8]. The relationship between these variables is illustrated in Equation (1) below [8].

$$R = \sigma_{metal} \frac{L}{A} \tag{1}$$

In this equation, R represents the measured resistance, σ represents the resistivity of the metal, L represents the length of the strip, and A represents the cross-sectional area [8]. In this equation, L and σ will be constant for the particular metal strip. Thus, if the resistance is measured across the metal strip, the cross sectional area can be determined mathematically. In this way, the reduction in cross sectional area can be determined and related to the probable amount of corrosion seen by the pipe.

These two methods are very common and are utilized frequently in the oil and gas industry as they can function in both conductive and non-conductive fluids. There are other methods which can be used to monitor internal pipeline corrosion. Some of these techniques are linear polarization resistance (LPR), zero resistance ammetery (ZRA), electrical field mapping (EFM), electrochemical impedance spectroscopy (EIS), and hydrogen probe techniques [8]. However, these monitoring techniques are far less widely used in the field due to power consumption, installation costs, excessive noise, and poor reliability [8].

2.8 Conductivity Measurement Theory and Literature Survey

Determining conductivity is an area of interest in multiple disciplines. In corrosion studies, conductivity is studied due to its relationship to electron movement which is pivotal in corrosive reactions. Many studies have been performed to determine the most effective way of experimentally determining conductivity and the most efficient sensors to produce the desired data.

2.8.1. The Double-Layer Polarization Effect

One of the primary considerations which must be taken into account when making conductivity measurements is the double-layer polarization effect. The double-layer effect occurs when an electrode makes contact with an electrolyte [10]. When current flows through the electrode and passes into the electrolyte, an electrochemical capacitor forms at their interface [10]. This kind of capacitor was first recorded by Hermann von Helmholtz in 1957 while he was performing experiments on a porous carbon electrode [10]. This effect was particularly noticeable due to the use of a porous electrode. Capacitor performance is related to surface area, and porous materials have a larger surface area than non-porous materials. Thus, there was more surface area which was in contact with the electrolyte and it could store more energy [10]. However, porosity only influences capacitance when the pores are relatively large. If the pores are not large enough, the ions cannot contribute to energy storage due to their restricted movement [10]. This double-layer polarization effect is utilized in the creation of supercapacitors. However, it becomes a hindrance in the case of electrodes and can conceal the properties which are intended to be measured.

2.8.2. General Conductivity Measurement Theory

The conductivity of a substance is equal to the reciprocal of the substance's resistivity. Resistivity is measured in units of Ohm-meters. The inverse of an Ohm is called a Siemen (S). Thus, conductivity is measured in units of Siemens per meter (S/m) [11]. Electrical conductivity can be measured in a variety of ways. The most common of these methods are measurement with two and four-electrode conductivity cells.

2.8.3. Two-Electrode Conductivity Cells

Two-electrode conductivity cells are simple instruments for determining conductivities of materials and are particularly useful when the material has a low conductivity [12]. Current is pushed

from one electrode to the other through the sample of interest. The voltage drop across them is measured. The conductivity of the sample can be then determined through Equation (2) below.

$$\kappa = \frac{IL}{VA} \tag{2}$$

In this equation, κ is conductivity, V represents voltage, A represents the cross sectional area of the sample, I represents the current, and L represents the length of the sample [12]. Though the simplicity of this cell is advantageous, there are significant downsides to this method of measuring conductivity. Particularly, the two-electrode conductivity cell should not be used if fouling of the electrodes is a concern. Substance buildup on the electrodes in a two-electrode cell can cause significant errors in measurement [11].

In a two electrode cell design, the electrodes are used to both supply the current across the sample and measure the resulting voltage drop which causes them to develop an electrochemical double-layer and polarize [13]. This double-layer effect on the electrodes can be modeled as capacitors in parallel with the existing resistances of the electrodes [14]. This is modeled as a circuit approximation in Figure 3.

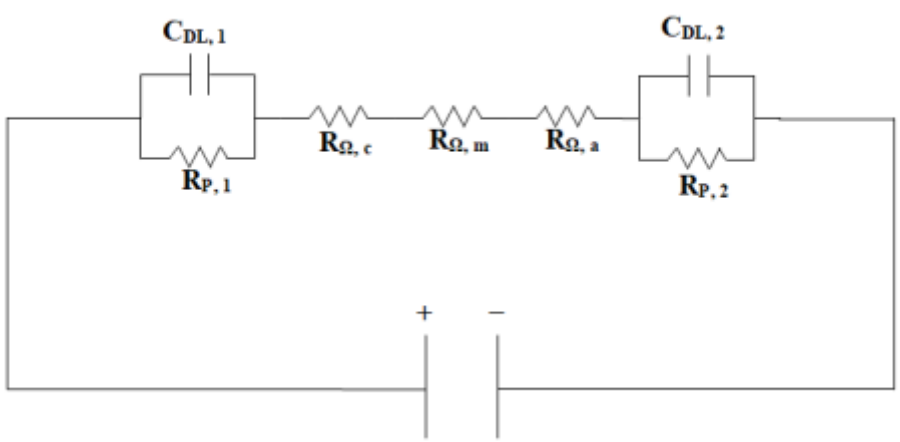

Figure 3: Two-Electrode Cell Circuit Approximation [14]

This figure displays the approximate circuit for a two-electrode conductivity cell in a conductive fluid. The resistivity of this fluid is represented by the three resistors joining the two cells together. The capacitors in parallel with the electrode resistors represent the double-layer effect. These capacitors initially behave as a short when the voltage source is turned on. However, over time, they will gradually gain charge, polarize the electrodes and affect the circuit.

2.8.4. Four-Electrode Conductivity Cells and the Wenner Theory

The problem of double-layer polarization was addressed by separating the current source and voltage measuring electrodes which resulted in the four-electrode conductivity cell. The four-electrode conductivity cell has four equally spaced electrodes: two outer electrodes to supply current and two inner electrodes to measure potential. Some four electrode cells function by maintaining a constant voltage across the two middle electrodes. This is achieved by supplying the necessary current to maintain this voltage across the outer electrodes [15]. This will minimize polarization of the two measuring electrodes [15]. However, the system must have enough power to provide the necessary current.

The four-electrode conductivity cell can also be approximated as a circuit as seen in Figure 4.

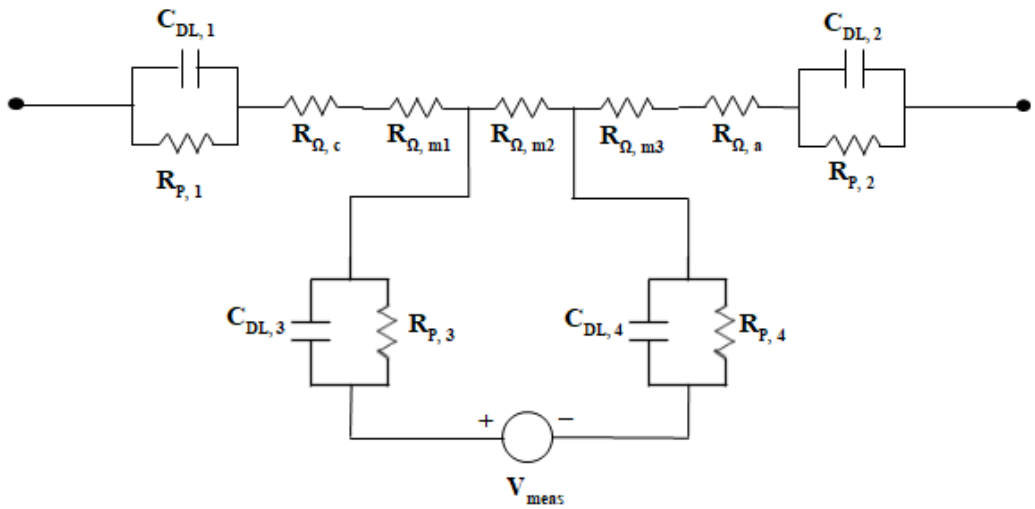

Figure 4: Four-Electrode Cell Circuit Approximation [14]

The addition of the two additional probes in this circuit reduces the polarization effects seen by the measuring electrodes. It also increases the cell's resilience against fouling and problems resulting from the material properties of the electrodes themselves.

The four electrode design was originally presented by Frank Wenner. He suggested the four electrode conductivity measuring technique as a means of measuring earth resistivity [16]. Wenner's design consisted of four linearly, equally spaced electrodes. A voltage was applied across the two outermost electrodes and the two center electrodes were used to measure the voltage potential at their respective locations. Using this potential difference, and with a known current applied to the sensor, Wenner found that earth resistivity could be determined using the following equation [16]:

$$\rho = 2\pi a R \tag{3}$$

In Equation (3), ρ represents resistivity which is the inverse of conductivity. R represents the resistance between the two center electrodes, found by dividing the voltage difference between them by the system current. The a in the above equation is the distance between the centers of the electrodes. Wenner noted that this equation only was valid if the depth of the electrodes in the earth

was small in comparison to a. The two in the above equation can be adjusted according to the depth at which the electrodes are placed. For instance, if the depth of the electrodes is equal to the spacing between them, the two becomes 3.37. If the depth is large in comparison to the electrodes, the two in the equation above would need to be replaced by a four in order for the relationship between resistance and resistivity to hold [16].

For measuring earth resistivity, Wenner suggested that the diameter of the electrode holes in the ground be no greater than 10% of the distance between the electrodes and that only the bottom surfaces of the electrodes make contact with the earth [16]. His equation for resistivity depended on this relationship in order to maintain the accuracy of his simplifying assumptions. In light of this relationship, he could assume that the electrodes behaved as point charges in the derivation of the governing equations. Wenner noted that his equations would only strictly hold as long as the distance between the electrodes was much greater than the diameter of the electrodes [16]. He further noted that a larger distance between the electrodes would allow resistivity to be measured at greater depths. Additionally, Wenner only considered these equations accurate if uniform resistivity between the electrodes could be assumed [16].

Wenner noted that a shortcoming of this four electrode method was the fact that the electrodes would encounter some polarization when current passed through them. However, he did not consider this a significant issue. Frank Wenner noted that the effects of the polarization would not affect the ability to determine earth resistivity as a high degree of accuracy would not be necessary [16]. In the case of measuring earth resistivity, electrode polarization does not affect a sensor's ability to gather meaningful data. However, this problem becomes considerably more pronounced when studying conductive fluids.

2.8.5. Electrochemical Potential Noise

Electrochemical potential noise (EPN) is another technique which can be used to study conductivity. This method utilizes two electrodes placed in a fluid with no applied current. This monitoring technique can feature electrodes of the same material, or of different materials depending on the desired output voltage range [14]. An EPN method measures potential difference and accompanying current between these electrodes over time [17]. The corrosion rate can be approximated using a factor called the noise resistance [17]. This noise resistance can be found using the standard deviations of the recorded potential and current signals. The equation for noise resistance is given below.

$$R_n = \frac{\sigma V_n}{\sigma I_n} \tag{4}$$

In this equation, σV_n stands for the standard deviation of the potential and σI_n stands for the standard deviation of the current [17]. Since no applied current is required for this method, it is one of the lowest power conductivity monitoring options. However, this method can only reveal if there is an electrolytic pathway between the electrodes and cannot provide more detailed data [14].

2.8.6. AC and DC Measurement Techniques

An effective method of combating double-layer polarization effects is powering conductivity probes with AC power at a high frequency [15]. High frequency AC power effectively prevents the capacitive effects of the double-layer polarization from occurring. In the case of Figures 3 and 4, usage of AC power would cause the capacitive C_{DL} elements to behave as shorts, leaving only the resistances of the electrodes [14]. In the case of AC power usage, the capacitive effects are negated and a two-electrode cell becomes nearly as useful as the four-electrode cell [14]. In addition, using AC techniques can reduce perceived noise in a system and improve overall measurement accuracy [14].

There are, however, disadvantages associated with AC measurement techniques. AC power requires complex circuitry to supply and measure [14]. Additionally, it takes substantial power to produce an AC waveform for the instrumentation. When limited voltage is available, this voltage must be split in order to be able to provide the necessary waveform amplitudes centered at ground [14]. Whenever power is readily available, however, AC techniques are commonly utilized to power conductivity sensors [11].

The advantages of DC measurement techniques primarily lie in their simplicity. An oscillator, which is needed to provide AC current, can be avoided in techniques utilizing DC power [13]. DC measurements are substantially easier to make than AC root mean square (RMS) measurements [14]. Thus, when power consumption or ruggedness is a priority, DC power can be preferable to AC power.

2.8.7. Electrode Materials

In order to lessen the double-layer polarization effect, the proper electrode must be chosen for the electrolyte which it will be exposed to [10]. Electrodes can be manufactured out of various conductive materials. The material selection depends on the desired application of the electrode. Factors to consider when choosing the electrode material are conductivity, hardness, machinability, and corrosion resistance [18]. Some common materials used for electrodes are copper, platinum, brass, silver, titanium and graphite [18]. Graphite, platinum, and titanium are very corrosion resistant, and are, therefore, very desirable materials for electrodes designed for use in corrosive environments. All of these materials have sufficient conductivities for use in electrodes, with copper, brass, and silver being the most conductive materials. Graphite and silver are both very soft materials, so they can only be utilized when they will not be subjected to significant wear. On the other hand, titanium, platinum, copper and brass are stronger materials and can be used in harsh

environments. However, this can also make them more difficult to machine. All of these properties must be considered when determining electrode material for a particular application.

2.8.8. Water Distribution and Conductivity Measurements

A study conducted by Oystein et al. aimed to determine the percentage of water present in a pipeline using multiphase meters [19]. Multiphase meters can be used to measure the flow rates of individual phases in a flow regime. However, these meters tend to be very expensive and not very accurate. Additionally, they require manpower for interpretation and calibration and are therefore time consuming [19]. The study results noted that conductivity is difficult to measure with reasonable accuracy in the field.

A study performed by Wang et al. sought to determine locations in which water was being held up in pipelines. They proposed a system which would indicate locations where water was collecting in a pipeline using water conductivity in a vertical column using a two electrode system [20]. It was noted, however, that since conductivity is a function of temperature and salinity, this quantity needed to be known before the amount of water collection could be determined.

2.9 Sensor Node Background

Sensor nodes are frequently used to take data readings over systems spanning a large area. Generally, these nodes remain on a low-power mode until they are instructed to activate and take readings [21]. These readings can be gathered from the nodes when desired.

2.9.1 Powering Sensor Nodes

In a study by Sudevalayam and Kulkarni, the benefits and possible complications of data collection with sensor nodes powered by harvested energy were considered [22]. It was noted that battery powered nodes were generally problematic and not suited for widespread usage. Battery powered nodes are difficult to design so that they provide enough power for the desired purpose while remaining cost effective and reliable for the lifetime of the device [22]. This study maintained

that energy collecting nodes were a viable alternative. These nodes would harvest energy from the surrounding environment and convert it into usable electrical energy. However, available environmental energy varies according to location and season. This variation adds complexity to sensor design since available power must be considered. Thus, the fluctuation of available energy produced by the environment presents a significant design problem.

The easiest, reliable way to address the problem of providing sufficient power is to add energy storage to the node system. A power storage unit is able to charge when excess environmental energy is available and can be tapped whenever there is a shortage [22]. These storage units are generally connected directly to the source of power and are trickle charged. Pulse charging is also possible; however, this requires a high amount of current and requires an additional battery or circuitry to supply the current [22]. Nodes expend the greatest amount of energy when transmitting [22]. Thus, it is important to regulate the transmission times to make efficient usage of the available power.

An understanding of the percentages of consumed power in a sensor node system is necessary to minimize less critical processes and maximize energy efficiency. In a study by Torfs et al., a system of wireless sensor nodes was used to measure earthquake activity [21]. Each of the nodes required about 2 mW of power to operate. More than 25% of this energy was expended on sampling and storage [21]. These processes required the most power in the operation of the sensor. Sensing and readout were the next largest cause of power consumption followed by processing. Standby mode consumed the least amount of energy at about 0.1 mW [21].

2.9.2. The Zensor™ Network

One particular sensor network system, Zensor™, was designed by Lund and Petersen to be exceptionally resilient and flexible [23]. The system is composed of nodes, a wireless transceiver, solar panels, a capacitor circuit, a controller, and an analog to digital converter [23]. This sensor

system was designed to have a long lifespan of over 50 years. The purpose of this system was to be able to collect data over large areas with minimal cost. This system was designed to cost about $40 per node, which is approximately 1/30th of the cost of typical wireless nodes [23]. Each of these nodes has a range of 50 to 100 meters. A significant benefit of this system is that each of the nodes stores the information of the entire system. This allows for redundancy in the case of a single node's failure. Additionally, only one node needs to be pinged to collect the data of the entire system [23]. This saves significant time as data collection from multiple nodes can take several minutes per node [21].

2.10 Background Summary

There are many existing methods for identifying and monitoring pipelines for internal corrosion. These processes excel in certain aspects while they fall short in others. From the information gathered in this literature review, it can be concluded that no existing methods particularly suit the unique challenges presented by a rural environment. Instead, it was determined that a DC powered, four-electrode conductivity probe could be integrated into a Zensor™ Network as a novel means of monitoring pipelines for internal corrosion. This system would incorporate energy gathering and storage to create a rugged, low-power, low-maintenance system which could be deployed in rural areas. To minimize the effect of double-layer electrode polarization while minimizing power consumption, an instant-on technique would be utilized. With such a technique, the probe would be subjected to only short bursts of power, during which time the readings would be taken. This would give the electrochemical double-layer insufficient time to develop and allow the probe to take readings with minimal power usage.

This proposed system would have its own shortcomings as well. Being a low-powered system, it would experience a lack of resolution in certain conditions. However, its utility in rural areas, in particular, could be exceptional. In remote areas, the proposed system could potentially

indicate the presence of corrosive conditions long before they would have been identified otherwise. The pipeline sections could then be further examined using more rigorous methods if the situation warranted. When paired with existing techniques, internal corrosion could be more easily identified and greatly reduced in these rural pipelines.

Corrosion is a costly and sometimes unpredictable process. Thus, preventative techniques are highly beneficial to both the oil and gas industry and the environment. They should be constantly adapted and improved upon. The proposed system would be a valuable addition to this endeavor.

Chapter 3 Experimental Methods

In order to produce a prototype conductivity node for the desired system, three apparatuses were designed and manufactured. These were the conductivity probe and associated control system, a heating apparatus, and a water test cell. These three apparatuses were necessary components of a probe prototype test cell. This three-element cell, once created, would be paired with identical cells and integrated into the final wireless communication system.

3.1 Preliminary Research and Design

It was determined from the beginning of the project that a four electrode configuration for the conductivity probe was desirable based on the work of the aforementioned Wenner research. Additionally, research was conducted to determine the body design of the final probe. It was determined that a flush mount probe with an optional corrosion coupon attachment would suit the design requirements of the project. An image depicting the proposed probe geometry follows in Figure 5 below.

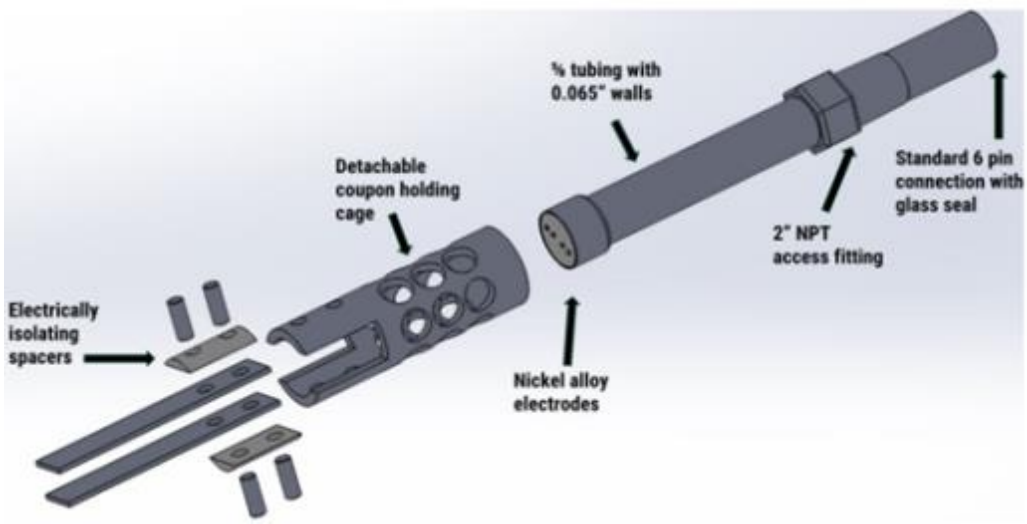

Figure 5: Proposed Undergraduate Conductivity Probe Design

3.2 Initial COMSOL Multiphysics Simulation

The first task undertaken during this study was to simulate the conductivity probe face with a multiphysics program called COMSOL. One purpose of these simulations was to determine how different geometrical configurations of the electrodes would impact the performance of the probe. Primarily, the potential difference between the two middle electrodes was studied to determine if it would be measurable using the desired low-powered techniques. Additionally, simulations were performed to ensure that the electrical field produced by the probe would not be impacted by the steel pipeline. Both 2D and 3D simulations were performed to ensure that the probe could function as desired with the planned geometry. The primary constraint during these simulations was the size of commercially-available hydraulic access fittings. The probe was simulated with a diameter which could fit into such fittings.

3.3 Probe Material Selection

It was necessary to determine the materials from which to construct this probe. Common materials to construct electrodes were researched to determine the materials which would be used for the electrodes and for the probe face. It was necessary to choose a material for the probe face which had a conductivity value of roughly 1 to 2 orders of magnitude smaller than the electrode material. If this requirement was met, the casting material would not impact the readings taken across the electrodes. Multiphysics simulations were also performed using constant geometries with varying materials to see how the different materials would impact the probe's performance. Nickel was used as the electrode material for the majority of the multiphysics simulations due to its conductivity properties and due to the fact that it is a common electrode material. In these simulations, the nickel electrodes were set in non-conductive epoxy resin.

Once the 3D probe geometry and materials had been modeled, the operation of the probe face was simulated in fluids of varying conductivities. The potential at each of the middle electrodes

was measured and the difference was taken to determine how sensitive the controller for the system would need to be.

3.4 Copper Probe Construction and Testing

After the initial simulations had been run, the first prototype was constructed using copper wire electrodes set 5mm apart. Copper was chosen due to its excellent conductivity properties and its availability in the form of solid copper wire. However, it was noted that copper would not likely be the final material chosen for the probe due to its tendency to form an oxide layer. The first experiment using this prototype involved the application of a set voltage across the outside electrodes and the measurement of the applied current across the system and the induced voltage across the two center electrodes. This experiment was repeated in fluids of various conductivities. The probe factor of the prototype was also studied at this time. From Ohm's law, resistivity was found by dividing the voltage across the two middle electrodes by the applied current in the system. Conductivity is the inverse of resistivity and was found accordingly. The probe factor of the prototype is based on its geometry and allows for a relationship between measured resistance and solution conductivity.

3.5 Copper-Epoxy Probe Construction and Testing

The second prototype face consisted of copper electrodes set in epoxy resin. Simulations were run to determine the impact that casting the electrodes in epoxy would have on the system. At this point in the prototype testing, it was determined that double layer effects were significantly impacting test results. This electrochemical phenomenon was causing a capacitive effect at the electrode faces and impacting voltage readings. Thus, testing techniques were adjusted accordingly.

3.5.1. Galvanostatic Test

The next type of test performed on the prototype was a DC Galvanostatic test. In this test, a potentiostat was used to supply a constant current across the outside electrodes of the probe in

solutions of varying conductivities. The potential difference across the two center electrodes was measured and then related to conductivity using Wenner's theories (eq. 3) for four electrode conductivity probes.

3.5.2. Instant-Off and Instant-On Tests

Next, instant-off tests were performed in a further attempt to combat double layer effects while reducing necessary power consumption. This involved supplying a constant voltage across the outer electrodes of the probe, allowing the system to stabilize, and then shut off the power supply. The voltages across the internal electrodes were measured before and after the power supply shut off to determine the instant voltage jump. This difference in internal voltage differences was then used in Wenner's formulas (eq. 3) to determine experimental conductivity.

Instant-on tests were also performed in order to compare the two methods. In the instant-on method, the probe was powered off and then turned on to take a reading. After the data was collected, the power was cut off to reduce the double-layer effects on the electrodes. This method was easier to record and code and was, therefore, adopted for future tests.

3.5.3. Environmental Factor Tests

Experiments were next conducted to determine which environmental factors would impact the performance of the prototype probe. The probe was tested in beakers of varying diameters and depths to see if the proximity of the beaker walls would impact the performance of the probe. These tests were repeated in the COMSOL simulation software to ensure that the results were consistent. The probe was also studied while the solution being measured was agitated to determine if this affected conductivity readings. While these tests were being performed, measures were taken to ensure that the temperatures of the solutions were constant, due to the fact that temperature has a significant impact on solution conductivity.

3.5.4. Potentiostatic Electrochemical Impedance Spectroscopy Tests

Potentiostatic electrochemical impedance spectroscopy (EIS) tests were then conducted using the copper and epoxy probe. These tests studied the complex impedance when probe electrodes were subjected to sinusoidal waveforms of different frequencies. The ideal result of this test was to ensure that the phase angle remained close to zero over the spectrum of frequencies. This would indicate that the current and voltages recorded during the tests were in phase and that the capacitive effects experienced by the electrodes were negligible [14]. This test was performed in beakers of varying diameters and at varying depths to determine if either of these conditions would affect the phase angle.

3.6 Graphite-Epoxy Probe Construction and Testing

The final tested prototype for this study used 3mm diameter graphite electrodes set in epoxy resin. In order to set the graphite electrodes at the desired spacing in the epoxy resin, a clip was designed using SolidWorks 3D modelling software. This clip was printed using an UPrint SE Plus filament 3D printer using ABS plastic. This plastic is nonconductive and was chosen because it would not affect the electrical properties of the probe. The clip was inserted into the casting mold and held the electrodes as the resin set. An image depicting the clip and an image of the final probe face prototype follows in Figure 6.

Figure 6: Clip and Final Graphite and Epoxy Probe

The aforementioned tests which were performed on the copper and resin probe face were then repeated on the graphite and epoxy probe face.

3.7 Arduino Microcontroller

Once the final prototype probe face had been manufactured, the Arduino controller for the probe was designed and tested. The final circuit diagram utilized for the controller follows in Figure 7.

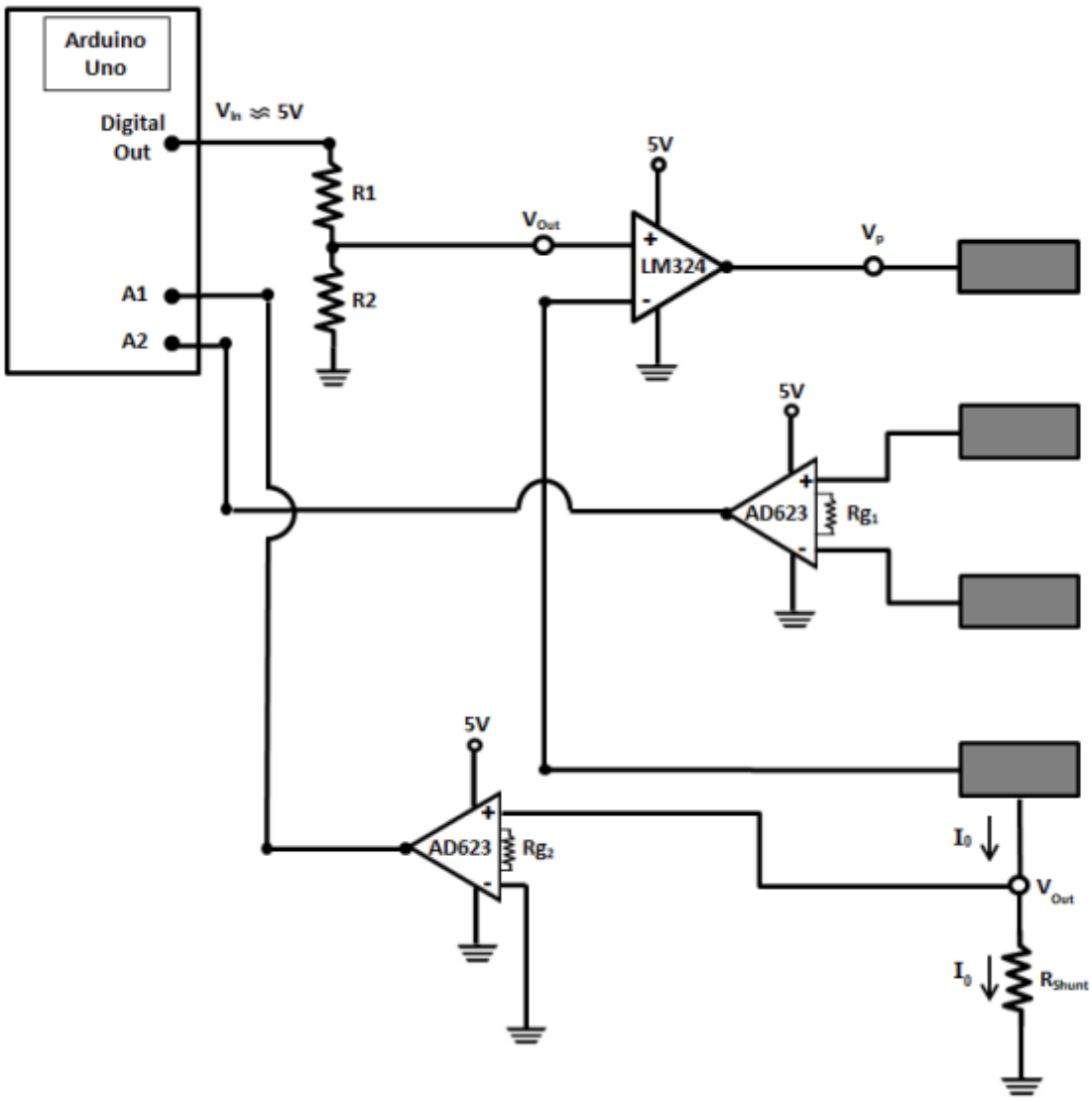

Figure 7: Circuit Diagram for Arduino Controller

Various gains were tested by adjusting R1 and R2 in the circuit in an attempt to maximize sensitivity in the voltage measurements taken between the two middle electrodes. To magnify the voltages and current read by the Arduino, LM324 and AD623 amplifiers were incorporated into the circuit. A shunt resistor was added to the circuit in order to supply values from which the current could be determined.

It was considered that only a certain degree of sensitivity would be manageable due to the nature of the Arduino. The Arduino UNO controller used for this study has a 10 bit analog to digital converter (ADC) and allowed for a 5V input. This meant that the Arduino could only sense increments of 5V divided by 1024, which is the number of discrete levels measurable by a 10 bit ADC. Thus, it was taken into consideration that a precision of less than 4.9 mV would be unattainable by the Arduino. This probe was tested in various fluids of varying conductivities to determine where the probe would see the greatest degree of sensitivity, and to determine what the probe would be able to identify once deployed.

This circuit was coupled with code that automated an instant-on test. The code began with the system powered off. Then, the Arduino was coded to wake up and push five volts across the outside probe electrodes. A measurement of the potential across the middle electrodes and the current across the shunt resistor was taken before the Arduino relayed the results to a serial monitor screen. It then powered down for an amount of time determined by the user to allow the electrode double-layer effects to dissipate before the process was repeated. This code is included in Appendix A.

3.8 Heating Apparatus and Peltier Thermoelectric Generator

The second testing apparatus which was constructed for the complete system node was a heating apparatus to simulate the hot side of a pipeline. Thermal analysis was performed to determine the appropriate size for a strip heater to heat the apparatus. The apparatus was then built

using 2 in. polystyrene foam, silicone, a steel plate and a 6 in. square 90 W strip heater. An Omega CN 7523 proportional-integral-derivative (PID) controller was attached to a K-type thermocouple and the strip heater so that the temperature of the steel plate could be controlled. A Marlow Industries EHA-PA1AN1-R02-L1 Thermal Electric Generator (TEG) Power Management Evaluation Board was purchased and studied along with this apparatus to determine the power generation that could be expected from environmental sources. A 1 farad supercapacitor was attached to this generator and was intended to simulate the power storage for the final sensor node. Figure 8 displays a SolidWorks rendering of the intended heater and the actual final heating apparatus, with the attached thermoelectric generator and PID controller.

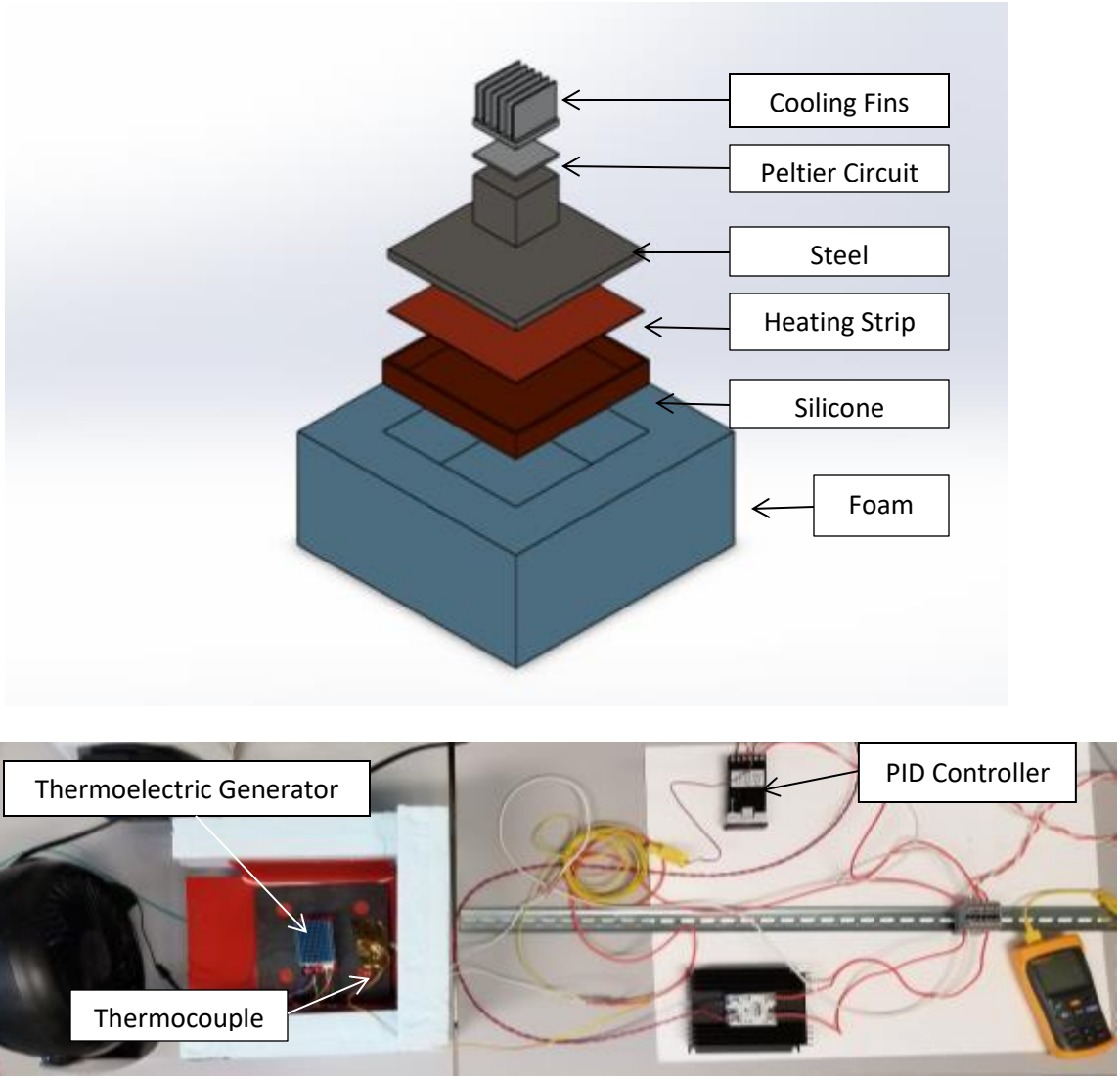

Figure 8: Modeled and Actual Heating Apparatus and Peltier Generator Setup

3.9. Water Test Cell

The last apparatus which was constructed to complete the individual sensor node was a water test cell. This cell was used in conjunction with a peristaltic pump in order to simulate the performance of the prototype probe system when exposed to various fluids of varying conductivities and viscosities and at different flow speeds. This water test cell is displayed in Figure 9.

Figure 9: Liquid Test Cell Setup

As can be seen in the figure, the conductivity probe was installed flush with the bottom of the liquid test cell in the way that it would be installed in a pipeline.

Chapter 4 Results and Discussion

4.1 COMSOL Multiphysics Simulations Results

COMSOL multiphysics simulations were performed on both 2D and 3D simulations. Mesh refinements were performed to ensure accuracy of produced data. The 2D simulations were performed to produce a general idea of the necessary spacing of the electrodes on the probe face. This was to ensure that the potential distribution across the electrodes would not be disrupted by their proximity to each other or to the edges of the probe face. Next, a 3D simulation was performed to gain a more accurate approximation of how the prototype probe would function. An image depicting the 3D model of the probe face in a 250 mL beaker is shown below. In Figure 10, the smaller circle represents the outside of the probe face and the large cylinder represents the diameter of the beaker.

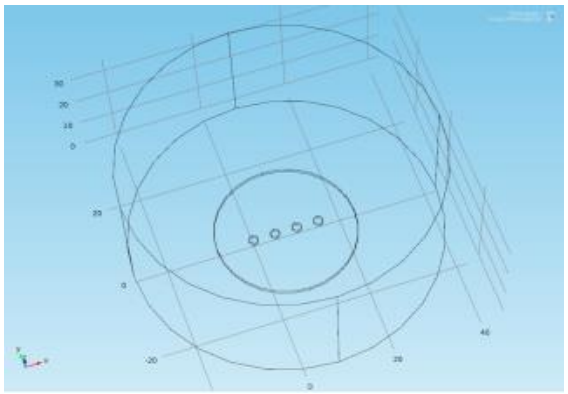

Figure 10: 3D Wireframe Model for Multiphysics Simulation

Tests were run using this model to simulate the behavior of the proposed probe face. One of the most notable tests performed involved inducing a current of 0.02 amps on one of the outside electrodes and determining the potential distribution across the inside electrodes in fluids of various conductivities.

One of these potential graphs is displayed in Figure 11.

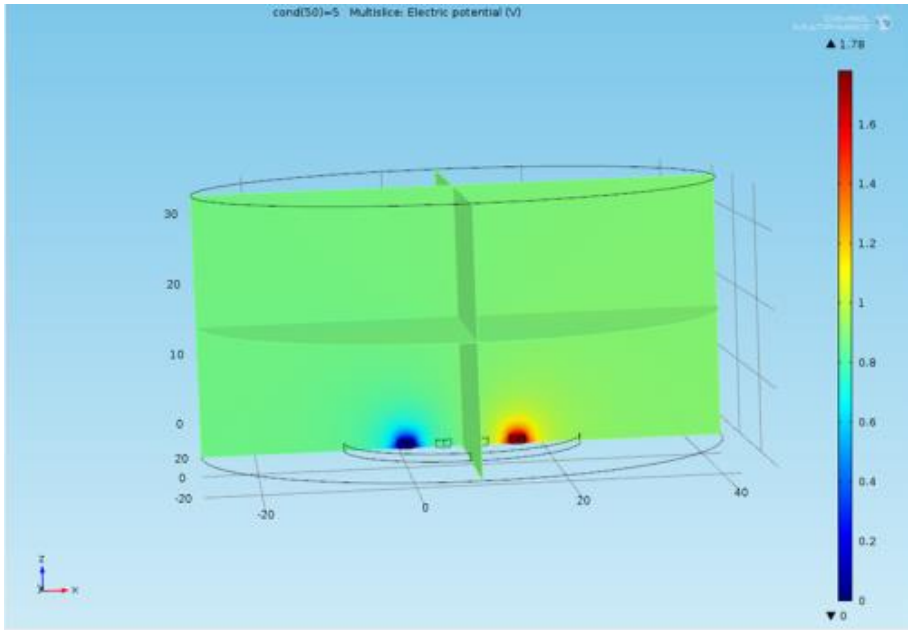

Figure 11: 3D Potential Graph

It was noted in this simulation that the majority of the generated potential and current rested within the bounds of the probe face. This was desirable as it indicated that the pipeline itself would not likely interfere with the performance of the cell.

Two simulation probes were placed in the 3D model to read the potential at each of the middle electrodes. These electrodes were copper in the simulation and were therefore equipotential across their faces. Thus, only one probe was necessary per electrode. These probes were placed at the center of the electrodes. These simulation probes were read at each fluid conductivity and the difference in their potentials was graphed as can be seen in Figure 12.

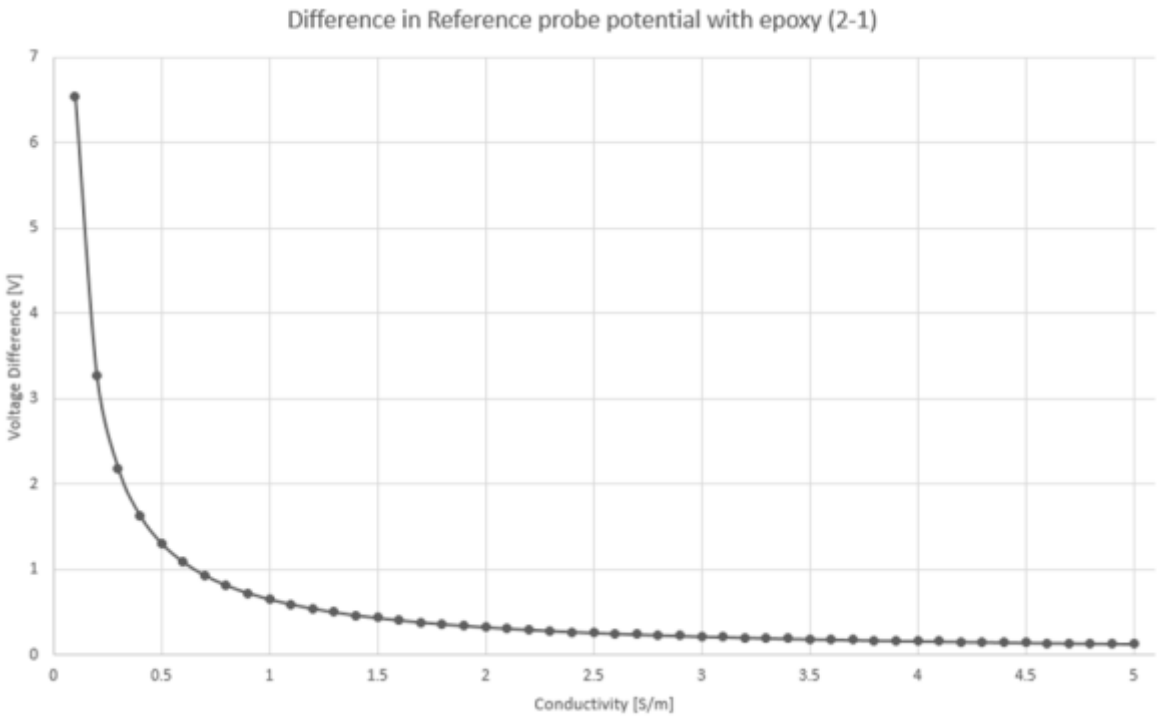

Figure 12: Plot Displaying Difference in Reference Probe Potentials

As can be seen by the slopes between the points on this graph, a low level of instrument sensitivity was expected at very low and very high conductivities. The most accuracy was expected at approximately 0.25 to 1 Siemens per meter. However, it was noted that there would be a considerable difference in the readings at high and low conductivities which was the most crucial aspect in the performance of the prototype conductivity probe.

4.2 Copper Probe Experiment

The first test performed on the copper probe prototype was a galvanostatic test. This test was performed on copper wire probes set at 5mm apart. A current of 0.2mA was induced in one of the outside electrodes and the potential difference across the inside electrodes was measured. The conductivity approximation was calculated using Wenner's formula (Equation 3) to determine if, given the voltage difference measured by the probe, the conductivity of the fluid could be

determined. The percent error was calculated, as well. The results of this test are shown in Table 1 below. Graphical versions of relevant tabulated data are available in Appendix B.

Table 1: Copper Probe Galvanostatic Test Results

Conductivity (S/m)	Voltage Difference (mV)	Wenner Conductivity Approximation (S/m)	Percent Error (%)
0.023	51.90	0.123	440.365
0.413	25.00	0.255	38.342
0.973	11.00	0.579	40.520
1.906	5.40	1.179	38.147
3.290	3.00	2.122	35.500
5.190	1.98	3.215	38.049

As can be seen in the table, there was a large degree of error in the approximation versus the true conductivity values. At this point, it was determined that the double-layer effects were greatly impacting the potential measurements. Thus, the next series of tests which were performed were instant-off tests. These tests were performed allowing the double-layer effects to dissipate between individual readings to combat their impact on the voltage readings. Current was determined in these tests through the measurement of voltage across a shunt resistor in series with the system. The results of one of these tests follow in Table 2.

Table 2: Copper Probe Instant-Off Test Results

Conductivity (S/m)	Resistor Voltage (mV)	Current (mA)	Voltage Jump (mV)	Wenner Conductivity Approximation (S/m)	Percent Error (%)
0.370	8.1	0.368	26	0.451	21.89
0.590	11.0	0.500	22	0.723	22.54
0.940	14.4	0.650	20	1.035	10.05
1.186	15.8	0.718	15	1.524	28.50
1.484	18.0	0.818	11	2.367	59.51
2.031	20.0	0.910	11	2.633	29.64

This series of tests generally had lower percent errors compared to the galvanostatic tests. The instant-off test voltage jumps were determined by taking the average of four readings. It is interesting to note that in the test run at 1.484 S/m displayed in the fifth column in Table 2, there was an unusually varied spread of voltage jump values which varied from 9 to 13 mV. If 13 mV is substituted for the recorded average of 11 mV in the Wenner formula, the percent error for this conductivity becomes 35% which is more consistent with the other readings.

4.3 Copper-Epoxy Probe Experiment

A copper and epoxy probe face was next fabricated and tested to more closely emulate the final probe face. Setting the wires in epoxy ensured that the electrodes remained at their desired configuration. It was postulated that the previous tests conducted on the copper wire prototype probe could have been subjected to errors due to the movement of the electrodes. A potentiostatic EIS test was run on the copper/epoxy probe face to study the phase angle and amplitudes of the probe system at varying frequencies and depths. The results of this test follow in Table 3 below.

Table 3: Copper-Epoxy Potentiostatic EIS Test Results

Depth (cm)	θ Low (degrees)	θ High (degrees)	Average Amplitude (kΩ)
0.5	-2.396	-4.233	20.87
1.0	-2.244	-4.363	21.55
1.5	-2.601	-4.343	22.02
2.0	-2.958	-4.504	22.28
2.5	-2.470	-4.474	22.59
3.0	-3.208	-4.787	22.88
3.5	-3.777	-6.175	23.22
4.0	-4.643	-7.829	24.00
4.5	-4.809	-8.236	24.35
5.0	-5.527	-10.510	24.97
5.5	-5.601	-11.330	25.05

The angles measured during this test were much larger than desired. Angles less than one degree from zero were considered acceptable. The large negative angles which were encountered demonstrated a considerable capacitance in the probe electrodes. This was determined to be due to the copper wires being used.

4.4 Graphite-Epoxy Probe Experiment

Graphite was determined to be a better probe material with a lower disposition to double-layer polarization effects. A probe was constructed with 3mm diameter graphite rods in epoxy. This reduced the angles of the potentiostatic EIS tests to the desired range of less than a degree from zero.

4.4.1. Instant-Off Tests

At this point, the probe was behaving predictably according to the Wenner theoretical equations and with acceptable accuracy for the purposes of its intended function. A run of instant-off tests across different fluid conductivities using a Gamry Reference 600 potentiostat was performed and the results are noted in Table 4.

Table 4: Graphite-Epoxy Probe Instant-Off and Multimeter Test Results

Actual Conductivity (µS/cm)	Low Voltage (mV)	High Voltage (mV)	ΔV (mV)	I (mA)	R =ΔV/I (Ω)
25.25	32.80	2437.00	2404.20	0.26	9358.51
84.5	21.87	1634.00	1612.13	0.40	4030.33
219.6	51.30	658.50	607.20	0.40	1518.00
776	37.27	210.50	173.23	0.40	433.08
2443	30.85	85.39	54.54	0.40	136.35
25760	8.42	13.58	5.16	0.40	12.90
69200	17.68	19.63	1.95	0.40	4.88

It was determined that given the constraints of the double-layer effects and minimal power consumption, that an instant-off test had considerable benefits. However, it would be difficult to code. For these reasons, an instant-on technique was adopted for the prototype conductivity probe node as it incorporated the benefits of the instant-off tests while being easier to implement in code.

4.4.2. Probe Factor Determination

From the test results displayed in Table 4, the probe factor for the graphite probe face was determined by multiplying the experimental resistance by the actual conductivity. The average probe factor was determined for all of the experimental runs. Using this average factor, an experimental

conductivity was determined by multiplying it by the resistances. The absolute error was then determined between the actual conductivity and the conductivity derived from the average probe factor. These results are displayed in Table 5.

Table 5: Probe Factor Determination Results

Actual Conductivity (µS/cm)	Probe Factor (1/m)	Conductivity from average probe factor (µS/cm)	Absolute Error (%)
25.25	23.63	34.33	35.97
84.50	34.06	79.72	5.66
219.60	33.33	211.65	3.62
776.00	33.61	741.88	4.40
2443.00	33.31	2356.37	3.55
25760.00	33.23	24906.32	3.31
69200.00	33.74	65905.96	4.76

In the first test run for the fluid with a conductivity of 25.25 µS/cm, the potentiostat was unable to supply the desired current which affected the results. However, the calculated probe factor was relatively consistent for the rest of the fluid conductivities at about 33 m^{-1}.

4.4.3. Arduino Controller Tests

The Arduino controller was then designed to take current measurements and potential differences across the middle electrodes of the manufactured probe face. The controller was tested using a test circuit with three resistors in series to determine if it would perform in an ideal environment before being exposed to the electrochemical effects and imperfections of the prototype probe. The results of this test follow in Table 6.

Table 6: Controller and Resistor Circuit Test Results

Actual Resistance (Ω)	Current (mA)	Experimental Resistance (Ω)	Absolute Error (%)
20	0.165	6.06	69.70
330	0.165	284.85	13.68
1000	0.165	945.00	5.50
2200	0.165	2151.52	2.20
4700	0.165	4600.00	2.13
5600	0.165	5418.18	3.25
6800	0.153	6764.71	0.52
7500	0.141	7368.79	1.75
10000	0.109	9878.35	1.22

As can be seen, at about 6000 ohms, the system's operational amplifiers became unable to provide the desired current across the system. Thus, a lower operational current of 0.1 mA was chosen for the operation of the controller. The results of the test with the adjusted current follow in Table 7.

Table 7: Controller and Resistor Circuit Test with Lower Current Results

Actual Resistance (Ω)	Current (mA)	ΔV (mV)	Experimental Resistance (Ω)	Absolute Error (%)
47	0.105	1	9.51	79.77
100	0.105	7	66.60	33.40
180	0.105	15	142.72	20.71
330	0.105	31	294.96	10.62
680	0.105	67	637.45	6.26
1500	0.105	156	1484.30	1.05
3000	0.105	317	3016.18	0.54
4700	0.105	490	4662.23	0.80
6800	0.105	725	6898.19	1.44
7500	0.105	791	7526.17	0.35
8200	0.105	873	8306.37	1.30
10000	0.105	1059	10076.11	0.76
15000	0.079	1183	15009.00	0.06

Decreasing the current allowed the controller to read a larger range of resistances without railing the operational amplifiers. This also led to an increase in sensitivity and a decrease in instrument error.

4.4.4. Graphite Probe and Controller Test

Finally, this controller was tested using the actual prototype probe face once it could behave predictably and acceptably under ideal conditions. The gains of the controller were adjusted by changing the resistors in an attempt to maximize sensitivity. It was determined that the amount of

time that it took for the controller to power on and take a measurement was approximately 0.3 milliseconds. The results from the test of the actual probe face in fluids of varying conductivities are displayed in Table 8.

Table 8: Controller and Graphite-Epoxy Test Results

Actual Conductivity (µS/cm)	Measured Conductivity (µS/cm)	Absolute Error (%)
186	185	0.54
686	629	8.26
1183	1151	2.70
2328	2961	27.21
5080	6296	23.93
7910	7391	6.56
10990	14813	34.79
41000	14483	64.68

As can be seen in Table 8, the controller starts to lose accuracy at about 10,000 (µS/cm). However, at this point, the controller displays that current is flowing with a negligible difference in voltage between the two middle electrodes. This indicates the presence of a conductive and, therefore, corrosive fluid. The lack of sensitivity at these conductivities was expected due to the nature of the controller's data storage abilities. At these higher conductivities, it was determined that it was sufficient for the controller to indicate the presence of the conductive fluid.

4.5 Heater and Thermoelectric Generator Experiments

The heating unit which was intended to simulate a hot pipeline was created using an Omega CN 7523 proportional-integral-derivative (PID) controller, a 90 Watt strip heater, and a commercially available Marlow Industries EHA-PA1AN1-R02-L1 Thermal Electric Generator

(TEG) Power Management Evaluation Board. The PID controller was autotuned to ensure that the heating unit could remain at the desired temperature of 180°F with little variation and without substantially overshooting the target temperature. The final CN 7523 PID settings, which were able to suitably maintain the desired temperature, are listed in Table 9.

Table 9: Omega CN 7523 PID Settings

Pid0	Su0	P0	i0	d0	i0F0
110	110	10.7	227	56	3.7

Tests were performed with the thermoelectric generator to ensure that once the University of Alaska Anchorage's Electrical Engineering department produced a prototype Peltier circuit for the system that the heating unit would be ready for operation. It was found that, using a fan and these PID settings, a temperature difference of approximately 30°F was obtainable. From the specifications sheet which accompanied the manufactured thermoelectric generator, this temperature difference would be enough to produce approximately 1.25 mW of power [24].

Upon creation of the final Peltier circuit, it will be determined if one generator coupled with a 1 farad supercapacitor will be sufficient to take readings with the prototype probe system at the desired time interval between measurements. If it is not sufficient, multiple Peltier generators will be joined together to produce the necessary power. Also, these circuits could be paired with other forms of environmental energy collection to produce the necessary power for the system. The design of this power system is ongoing and is not included in the scope of this thesis.

4.6 Water Cell Experiment

The peristaltic pump used for these tests could not exceed speeds of 300 RPM. This difference in speeds did not affect the reading of conductivities by the prototype controller and probe.

The probe's performance was tested when it was exposed to oil to see if it would be able to indicate the presence of salt water when mixed with oil. The test began with a mixture of salt water with a conductivity of approximately 41,000 μS/cm and oil in the test chamber. This mixture was then allowed to separate. After the phases separated, the peristaltic pump was attached to the cell and another mixture of tap water with a conductivity of approximately 180 μS/cm and oil was pumped into the chamber. The water and salt solutions were intentionally chosen with different conductivities to see how the sensor would react to the mixing of the two solutions. The results of this test follow in Table 10.

Table 10: Oil and Salt Water Test

Event	Sensor Reading (µS/cm)
Cell Agitated	0
Phases Begin to Separate	4761
	8332
	8195
Pump Turned On at 250 RPM	8470
	8470
	11110
	8332
	8332
	8332
	16665
	-1
	16390
	11110
	16665
	11293
Pump Stopped	185
	181

As can be seen in Table 10, the sensor was able to indicate the presence of the different corrosive fluids in the presence of oil when they settled out of the oil phase.

Chapter 5 Conclusion

The purpose of this graduate work was to create a working prototype which would be able to indicate the presence of corrosive fluids in an active pipeline. It was desired that this probe be able to meet this requirement while consuming a minimal amount of energy. This conductivity probe would be able to operate using environmentally available energy and would be suited for use in rural areas. This probe would supplement currently available corrosion monitoring techniques to supply more comprehensive data in rural areas.

A working prototype of this low-powered conductivity probe has been constructed. The probe can operate using a microcontroller which can perform quick, power efficient readings which reveal the presence of corrosive fluids. The probe, as expected, loses accuracy in the case of highly conductive fluids, though it can still indicate that they are present. At the point that the probe loses accuracy, about 0.1 S/m, the fluid would already be cause for concern if it were pooling in the pipeline.

The created prototype simulates how one individual node would operate in a wireless sensor network consisting of many of these nodes. The prototype is ready for incorporation into a wireless Zensor™ system, at which point it can be field tested.

References

1. Koch, G.H., Brongers, M.P., Thompson, N.G., Virmani, Y. P., Payer, J., 2001,"Corrosion Cost and Preventative Strategies in the United States," NACE International, TX.

2. Davis, J.R., 2000, Corrosion: Understanding the Basics, ASM International, OH.

3. Popoola, L.T., Grema, A. S., Latinwo, G. K., Gutti, B., Balogun, A.S., 2013 "Corrosion problems during oil and gas production and its mitigation," International Journal of Industrial Chemistry 4(1), pp. 1-15.

4. "Report 2007-A: Pipeline Performance in Alberta, 1990-2005," 2007, Alberta Energy and Utilities Board, Calgary, Alberta.

5. Tan, C., Li, P., Dai, W., Dong, F., 2015, "Characterization of Oil-Water Two-Phase Pipe Flow with a Combined Conductivity/Capacitance Sensor and Wavelet Analysis," Chemical Engineering Science, 134, pp. 153-168.

6. Craig, B., 1998, "Predicting the Conductivity of Water-in-Oil Solutions as a Means to Estimate Corrosiveness," Corrosion, 54(8), pp. 657-662.

7. Branko, N. P., 2015, Corrosion Engineering: Principles and Solved Problems, Elsevier, MA.

8. Papavinasam, S., 2014, Corrosion Control in the Oil and Gas Industry, Gulf Professional Publishing, Houston, TX.

9. Bickerstaff, R., Vaughn, M., Stoker, G., Hassard, M., Garrett, M. , 2002, "Review of Sensor Technologies for In-Line Inspection of Natural Gas Pipelines," Sandia National Laboratories, Albuquerque, NM.

10. Sharma, P., Bhatti, T.S., 2010, "A Review on Electrochemical Double-Layer Capacitors," Energy Conversion and Management, 51(12), December, pp. 2901-2912.

11. Brodgesell, A., Fletcher, K. S., Gray, J. R., 2017, "Conductivity Measurement," Instrument and Automation Engineers' Handbook, 5th ed., Liptak, B. G., ed., CRC Press, Boca Raton, FL, pp. 235-247.

12. Singh, Y., 2013, "Electrical Resistivity Measurements: A Review," International Journal of Modern Physics: Conference Series, 22, pp. 745-756.

13. Winslow, J. D., 1976, Conductivity Measurement Probe, United States, 3,936,729.

14. Jones, D. A., 1992, Principles and Prevention of Corrosion, 2nd ed., Macmillan Publishing Company, MI.

15. "Conductivity Theory and Practice," 2004, Radiometer Analytical, France.

16. Wenner, F. 1916, "A Method for Measuring Earth Resistivity," Bulletin of the Bureau of Standards,12, pp. 469-478.

17. Britton, C. F., 2010, "Corrosion Monitoring and Inspection," Shreir's Corrosion, vol 4., Cottis, B., Graham, M., Lindsay, R., Lyon, S., Richardson, T., Scantlebury, D., Stott, H., eds., Elsevier Science., Philadelphia, PA, pp. 3117-3166.

18. "Electrodes and Electrode Materials Information," accessed September 9, 2019,https://www.globalspec.com/learnmore/materials_chemicals_adhesives/electrical_optical_specialty_materials/electrical_contact_electrode_materials/electrical_contact_electrode_materials.

19. Oystein, L.B., Nyfors, E., 2002, "Application of Microwave Spectroscopy for the Detection of Water Fraction and Water Salinity in Water/Oil/Gas Pipe Flow," Journal of Non-Crystalline Solids, 305(1), pp. 345-353.

20. Wang, D.Y., Jin, N.D., Zhai, L.S., Ren, Y.Y., 2018, "A Novel Online Technique for Water Conductivity Detection of Vertical Upward Oil-Gas-Water Pipe Flow Using Conductance Method," Meas. Sci. Technol. 29(10).

21. Torfs, T. et al., 2013, "Low Power Wireless Sensor Network for Building Monitoring," IEEE Sensors Journal, 13(3), pp. 909–915.

22. Sudevalayam, S., Kulkarni, P., 2011, "Energy Harvesting Sensor Nodes: Survey and Implications," IEEE Communications Surveys & Tutorials, 13(3) pp. 443–461.

23. Lund, J., Petersen, T., 2016, Long Lifespan Wireless Sensors and Sensor Network, U.S. Patent 9,257,036 B2, filed May 10, 2013, and issued February 9, 2016.

24. Marlow Industries, Inc., "Thermal Energy Harvesting Demo Unit Solid to Air," EHA-PA1AN1-R02-L1, accessed September 26, 2019, https://cdn2.hubspot.net/hubfs/547732/Data_Sheets/EHA-PA1AN1-R02-L1.pdf.

Appendix A:

Code for Arduino Microcontroller

```
const int inner = A0; //A0 connected inner electrodes
const int resist = A1; //A1 connected to shunt resistor for calculating current

int inner_voltbefore = 0; //variable to store voltage between inner electrodes before current jump
int inner_voltafter =0; //variable to store voltage difference between inner electrodes after current jump
int resistor_volt = 0; //variable to store resistor voltage
int current = 0; //variable to store calculated current
int jump = 0; //variable to store voltage jump

void setup() {
  // put your setup code here, to run once:

Serial.begin(9600);    //serial port
pinMode(8,OUTPUT);    //declare digital pin 8 an OUTPUT. Will be set to 5V
pinMode(inner, INPUT);  //declare inner an INPUT
pinMode(resist, INPUT);  //declare resist an INPUT
}

void loop() {
  // put your main code here, to run repeatedly:

inner_voltbefore = analogRead(inner);//read voltage across inner electrodes before current applied


Serial.println("Turn on");
digitalWrite(8,HIGH); //Sets pin 8 to 5v

inner_voltafter = analogRead(inner); //read voltage across inner electrodes
resistor_volt = analogRead(resist); //read voltage going into shunt resistor

// records the actual voltage jump. 10kohm resistor across 623 --> gain 11 4.9 mV from 5v/1024
jump = ((inner_voltafter*4.9) - (inner_voltbefore*4.9))/11;


current = (resistor_volt*4.9); //take voltage across shunt
Serial.print("Current (mA x3000) =");//gain 3.15 across 1kohm resistor (3*1000)
Serial.println(current);
Serial.print("Voltage Inner before (mV x11) =");
Serial.println(inner_voltbefore*4.9);
Serial.print("Voltage Inner after (mV x11) =");
Serial.println(inner_voltafter*4.9);
Serial.print("Actual voltage jump (mV)= ");
Serial.println(jump);
Serial.println("To calculate resistance divide voltage jump by (current/3000)");


Serial.print("Arduino current Conductivity with 330000(cell constant/resistance) (microsiemens/cm) = ");
Serial.println((330000*current/3000)/jump); //cell constant = 330000.

//The following section is intended to allow for the user to experiment with other cell
//constants without changing the established 330000 constant
//Serial.print("Arduino current Conductivity with 300000(cell constant/resistance) (microsiemens/cm) = ");
//Serial.println((300000*current/3000)/jump); //cell constant = 300000.

Serial.println("   ");

digitalWrite(8,LOW); //Turn off pin 8
delay(120000); //wait 120 seconds (this number is in milliseconds)
```

Appendix B:

Graphs of Tabular Data

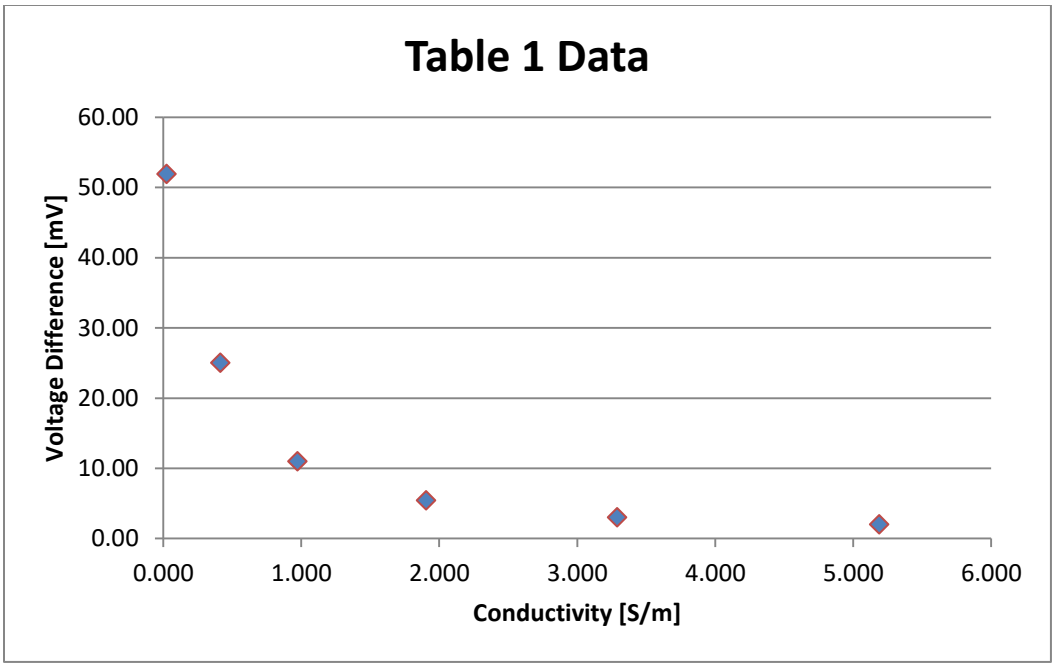

Figure B-1: Graphical Representation of Table 1 Data

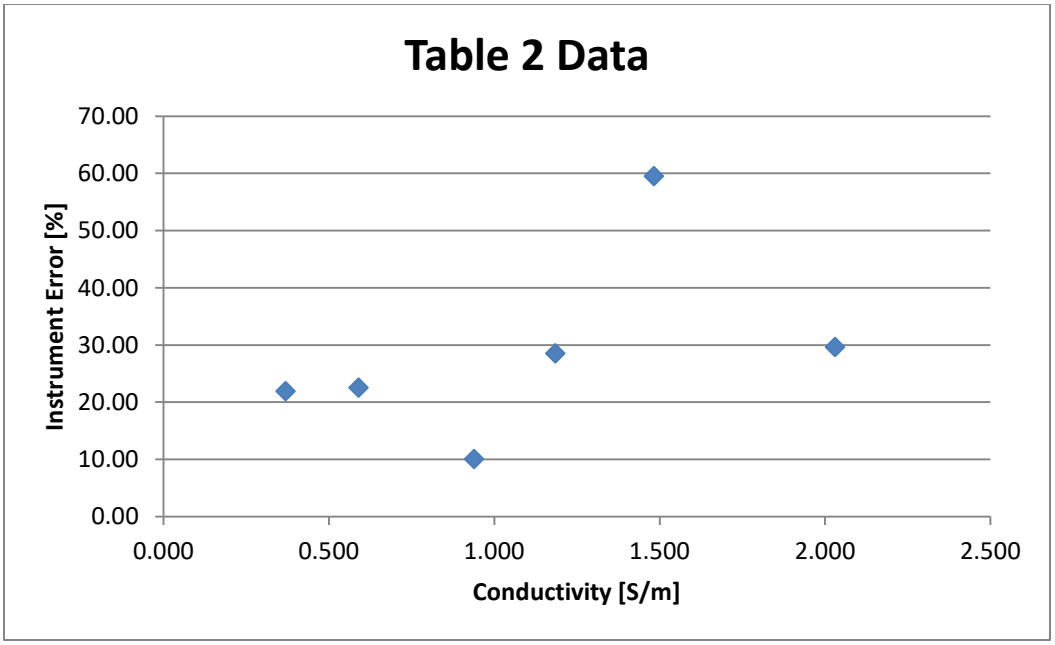

Figure B-2: Graphical Representation of Table 2 Data

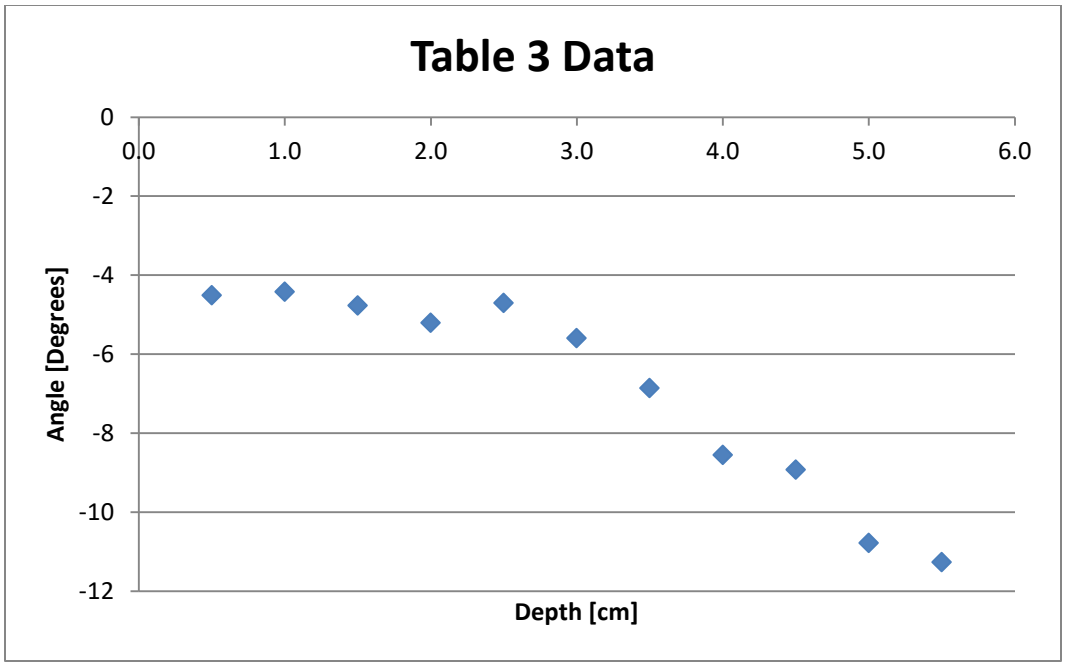

Figure B-3: Graphical Representation of Table 3 Data

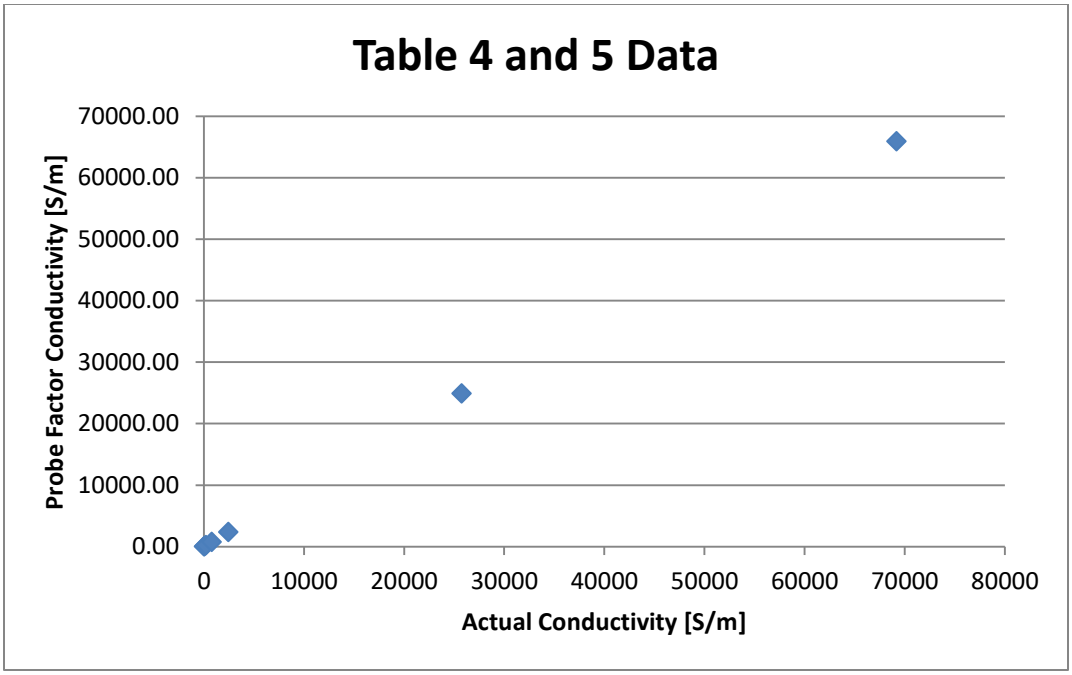

Figure B-4: Graphical Representation of Table 4 and 5 Data

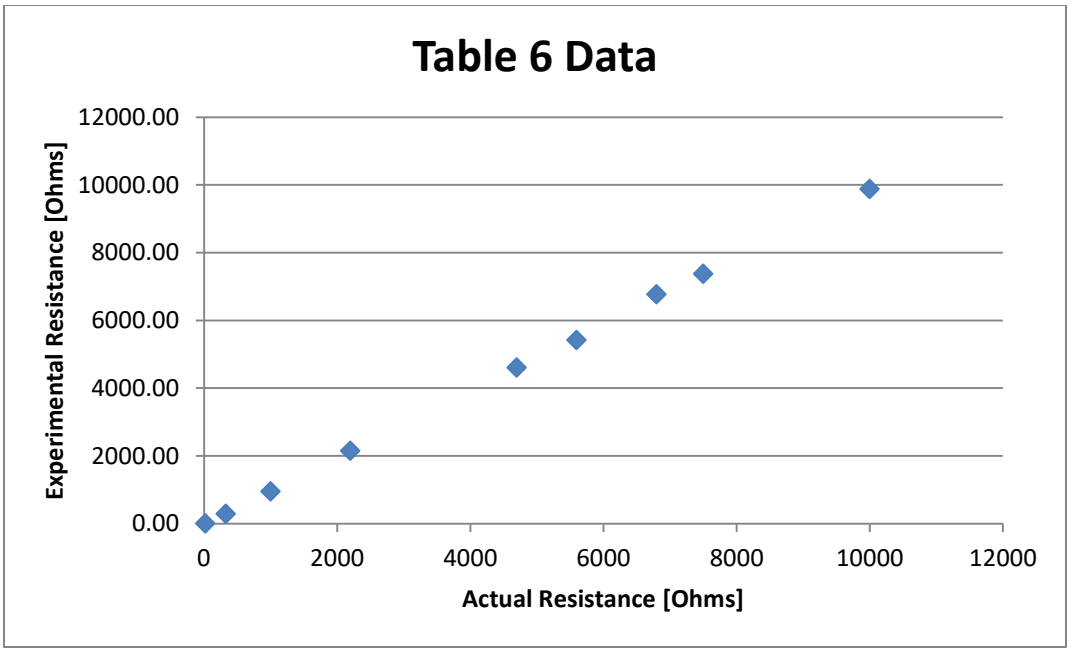

Figure B-5: Graphical Representation of Table 6 Data

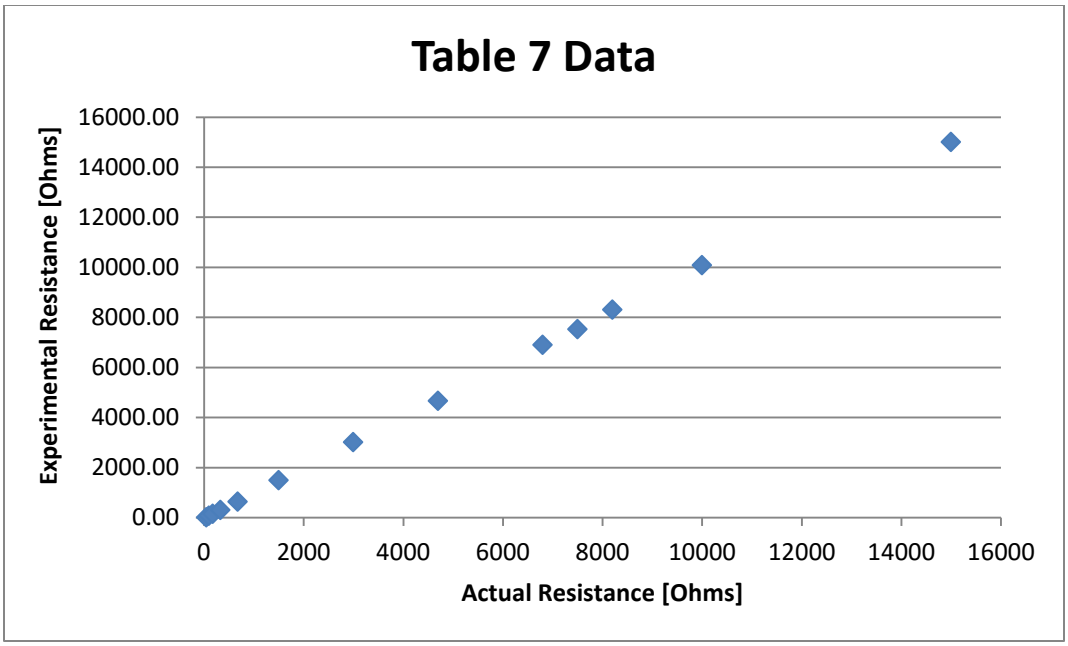

Figure B-6: Graphical Representation of Table 7 Data

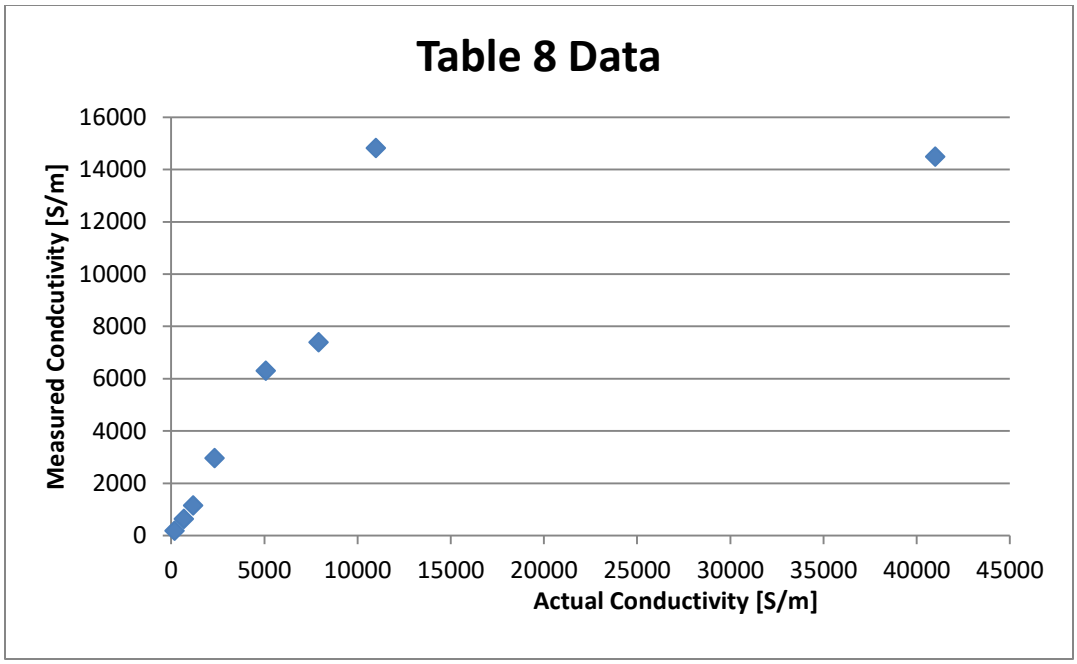

Figure B-7: Graphical Representation of Table 8 Data

Appendix 5: Thermoelectric generator report

Low Power Conductivity Sensor

Todd Petersen, Jacob Stirling

Abstract:
These trials served the purpose of developing a low power conductivity sensor for collecting data on the Alaska oil pipeline. The first trial was concerned with determining the maximum voltage the Peltier junctions were capable of producing. The second set of trials were conducted to prototype different boost conversion circuits for the purposes of powering the Arduino Uno Wifi. The third set of trials were conducted to determine if the power supplied by the Peltier junctions was sufficient to charge the supercapacitors that would function as the batteries for the Arduino unit.

1. Introduction

The purpose of these experiments was to develop a low current, power source for a microcontroller that would serve as the control unit for a measurement device to monitor the electrical conductivity inside of a large pipe. This was to be done by using *Marlow TG12-6 82078* [1] Peltier junctions as thermoelectric generators to produce electrical power from excess heat on the pipeline in conjunction with boost converter circuits to step the voltage and current into levels appropriate for powering the Arduino Uno WIFI, which is to be used as the microcontroller unit.

2. Procedure

A. Testing Peltier junctions

To test the Peltier junctions, they were placed on a heating device of at least 75 °C, the actual temperature of which is recorded in Tables 2 and 3. After the temperature is measured, a series of resistors of increasing value were connected between the anode and the cathode of the Peltier junction in order to measure the voltage produced and set a current draw from the unit. A passive heat sink was placed on top of the cold side to slow thermal saturation. The voltage drop across this resistor was measured on a digital multimeter and the maximum voltage measured during the trial was recorded. The passive heat sink used during these trials was insufficient in preventing thermal saturation, so an “instantaneous” reading for the voltage at the maximum temperature difference was recorded, along with the temperature of the cold side of the device.

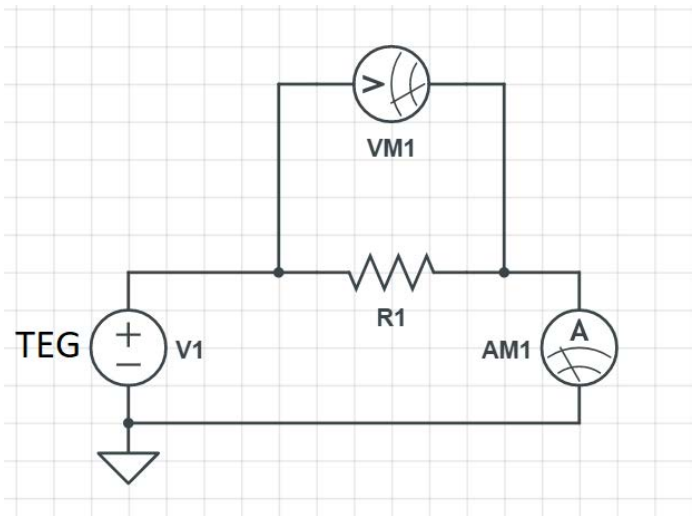

Figure 1: the DC voltage source V1 represents the Peltier Junction and R1 as the resistance the voltage is being measured over

a. Test 1, *TEC1-12706*

   i. The first set of trials conducted was on the voltage generation of the *TEC1-12706* Peltier Junctions through different magnitudes of resistors. These devices were designed to convert an electric current into thermal transport, thus creating a hot and cold side of the junction. However, these can also be used to turn heat flow into an electrical current (and voltage). This test was conducted in order to get an idea of how much voltage could be expected from this type of device and if they could ever generate enough voltage to be boosted. Temperature differences were not recorded for this trial.

Resistance	Test 1 (V_g)
10Ω	1.058 V
100Ω	1.065 V
1KΩ	0.8126 V
10KΩ	0.7221 V
100KΩ	0.7171 V

Table 1: First set of TEG tests.

b. Test 2, *Marlow TG12-6 82078* [2]

   i. The second set of trials conducted was on the voltage generation of the *Marlow TG12-6 82078* Peltier Junctions through different magnitudes of resistors. These devices were designed to better convert thermal energy into electric current more efficiently than the *TEC1-12706* units. These trials were conducted to determine if these units could produce enough voltage individually to power a boost converter that would power the Arduino. The temperature of the hot and cold side were recorded at the time the peak voltage was observed and recorded. These results are in Table 2.

Resistance	Test 2 (V_g)	Test 2 (t_{plate} , t_{top})
10Ω	1.067 V	76.1°C , 38.9°C
100Ω	1.117 V	73.6°C , 38.8°C
1KΩ	1.56 V	76.4°C , 40.5°C
10KΩ	1.352 V	78.1°C , 40.3°C
100KΩ	1.265 V	79.5°C , 40.4°C

Table 2: Second set of TEG tests

c. Test 3, two *Marlow TG12-6 82078* in series

i. The third test conducted with the Peltier junctions were to measure the voltage, current, and temperature of two *Marlow TG12-6 82078* units that were thermally in parallel and electrically in series. The purpose of this test was to determine if the voltages produced by the Thermoelectric Generators (TEGs) would be additive in series, and if this voltage produced by these TEGs could be represented as a simple Thevenin or Norton equivalent model for use in later modeling for the boost converter circuitry.

ii. The TEGs were thermally in parallel, i.e. adjacent to each other, so that both would be experiencing the same temperature differential which results in both devices producing the same voltage. If the devices were thermally in series, i.e. stacked on top of each other, then one device would operate as a generator while the other would operate as a load, which would produce less power than a single unit by itself. The devices are electrically in series because we are primarily concerned with generating enough voltage to be boosted, and not as concerned with doubling the current. The voltage measured was ample enough to give some choices when selecting the boost converter to be used in the next stage. Voltage measurements with recorded temperature differential are presented in Table 3. Each row corresponds to the listed load resistor, and the measured current is also listed.

Resistance	Test 3 (V_g)	Test 3 (t_{plate} , t_{top})	Test 3 (I_m)
10Ω	1.10	74.9 °C , 39.1°C	108 mA
100Ω	2.07	82.9°C , 39.3°C	21 mA
1KΩ	2.32	80.5°C , 40.4°C	2.3 mA
10KΩ	2.75	84.2°C , 43.4°C	0.262 mA
100KΩ	2.49	81.3°C , 37.6°C	0.025 mA

Table 3: Third set of TEG tests

iii. Figure 2 shows a plots comparing the measured voltage output for the TEG vs increasing load resistance and a theoretical Thevenin Equivalent circuit model for the TEGs. Two values were picked for the Thevenin equivalent resistance in the theoretical models at 10 and 20 ohms. These values were chosen as the experimental measurements fell within these bounds. A plot of the raw voltage output measurements versus load resistance is generally deterministic, but as the output voltage from the TEG varries with temperature difference, an attempt to normalize the data to the difference in temperatures was done to reduce varaibles in the analysis. Both plots are presented, with little variation between the two.

The results suggest that a simple Thevenin or Norton equivalent model for the TEG is not reasonable as there are other non-linear properties of the Peliter Junction that are at work. We proceeded to move on to more experimental measurements of what electrical power the devices could produce rather than continuing to work on modeling.

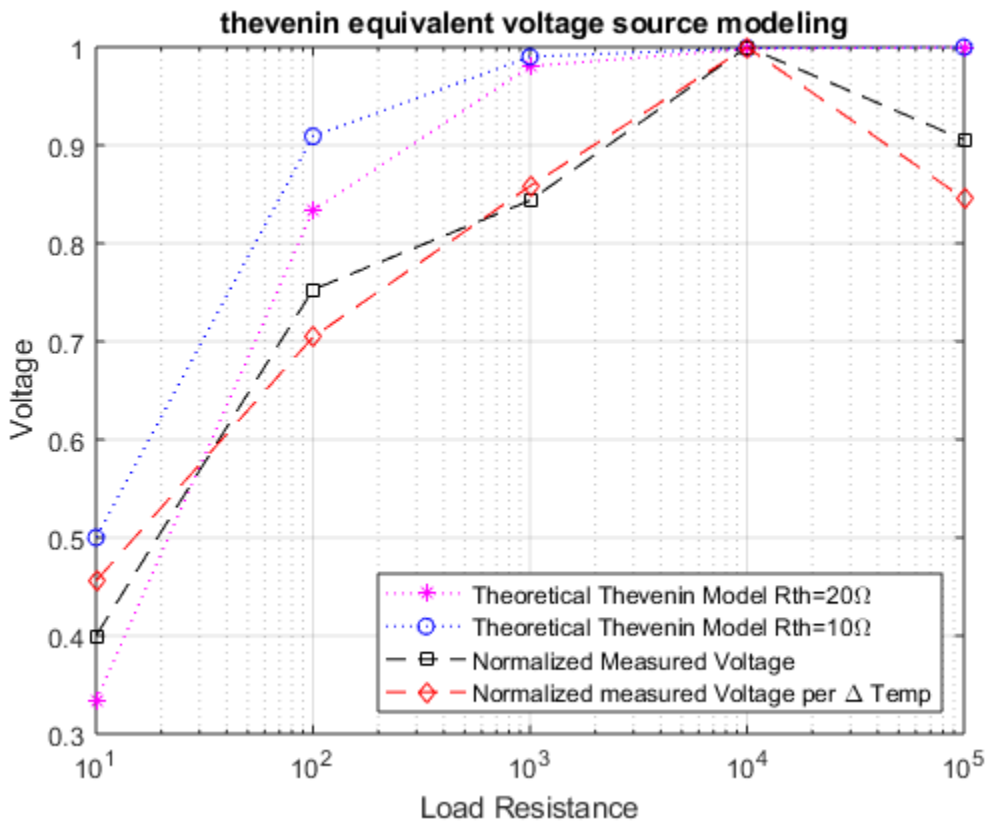

Figure 2: Comparison of TEG output voltage taken with increasing load resistance. Theoretical response with a 10Ω and 20Ω Thevenin equivalent resistance, raw voltage data, and TEG voltage output per temperature difference on the Peltier junction.

B. Code

During this portion of the testing, code was written to be executed when the Arduino unit was powered to test how long the Arduino would have to be in a sleep state and how long it could be on per charging cycle. Separate code was also written to determine the minimum voltage required to turn the digital pin on the Arduino high for the purposes of triggering the interrupt pin to wake up the Arduino. The full code described is listed in appendix B

While researching the sleep functionality of the Arduino, literature indicated that the sleep modes available would only turn off the ATmega microprocessor, while leaving the rest of the peripheral electronics online. For further development, it is recommended that an ATmega microprocessor alone be used in prototyping future versions to further reduce power costs.

C. Boost regulator Integrated Circuit Chips

d. Surface mount

i. The *TPS6122* [3] integrated circuit was theoretically able to provide the voltage step up that we require given the voltage and current the TEGs can produce. Simulations in LTSPICE proved promising. Ultimately this trial did not get past the prototyping phase due to difficulty in soldering a prototype together. The form factor for the chip (SC-70) is a surface mount chip with 0.65mm spacing between pins. A circuit board for this circuit was milled on site, but the scale was too small to facilitate soldering. Figure 3 shows the LTSPICE example circuit which would have been used to boost the voltage generated to power the Arduino Uno Wifi.

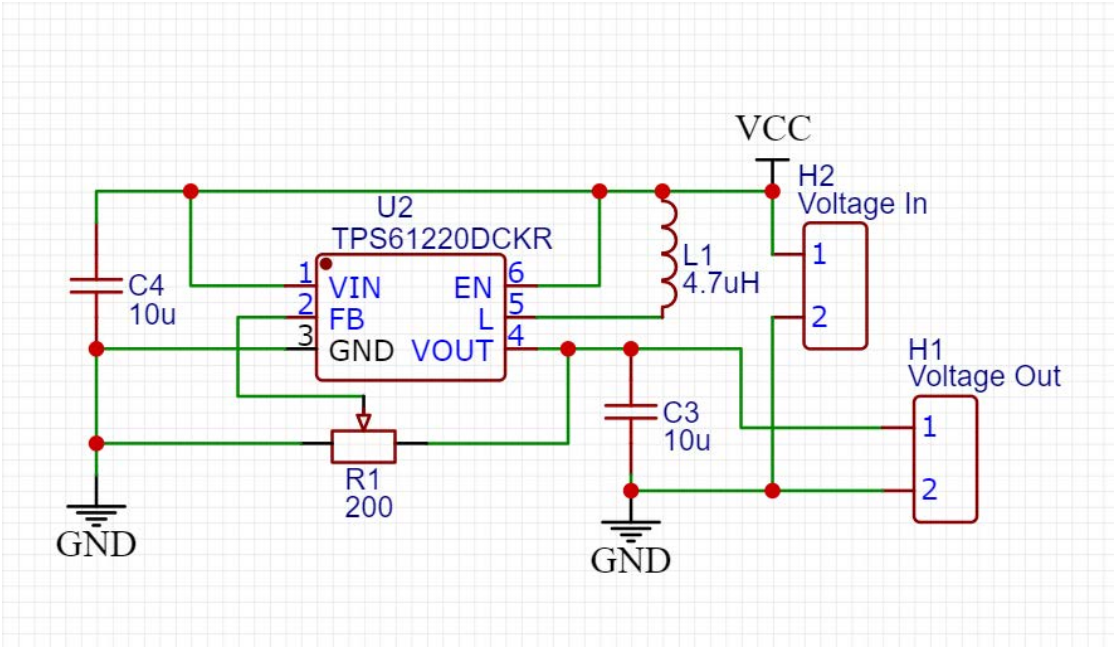

Figure 3: Sample circuit for TPS6122 boost converter

e. Through hole options

Two through hole IC Boost regulators were selected for trials, The *MAXIM MAX630* [4] and the *Texas Instruments TL499A* [5]. Both circuits were prototyped on a solderless breadboards, and a soldered version on a prototyping board was construed.

i. MAXIM MAX630

1. This device has a higher minimum input voltage (2.300 V) requirement to be able to charge the super-capacitor to a range that will power the Arduino. It has an internal voltage comparison which could have been used to trigger an interrupt on the Arduino which made this chip a viable option. The voltage required by this

chip is still within the scope of voltages that two TEGs can theoretically provide, so this should provide a good comparison for the for boost regulator options. The full schematic for the circuit prototyped is in Figure 4.

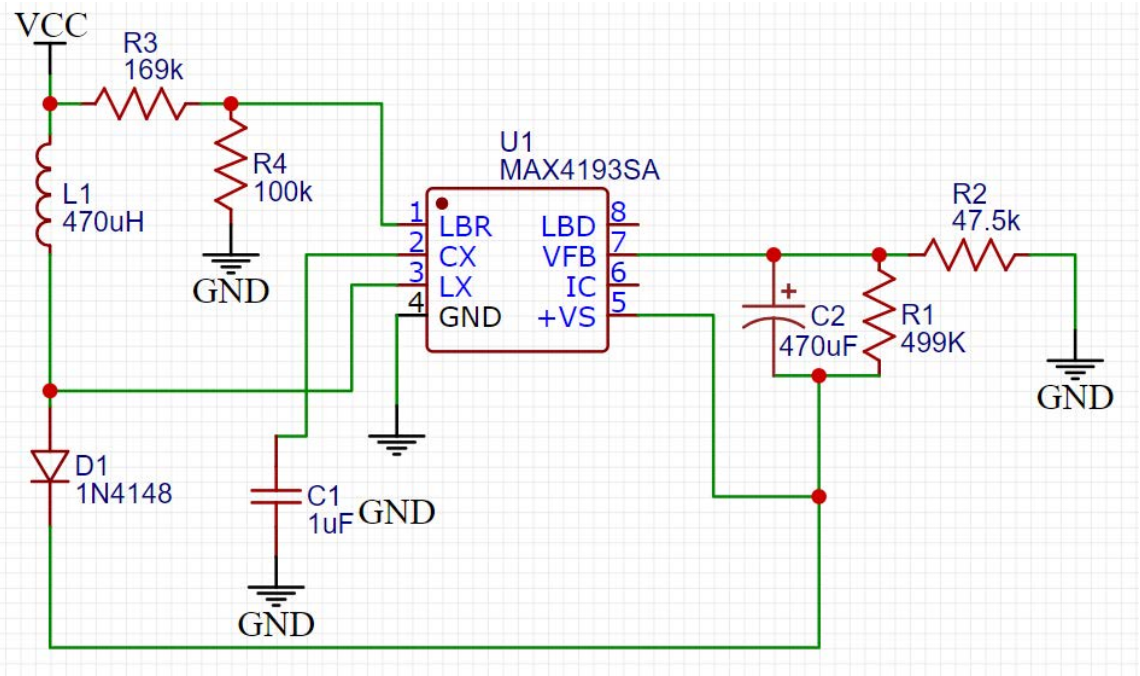

Figure 4: Sample circuit for MAXIM 630 boost converter

ii. TL499

1. This device operates on lower minimum input voltage (1.00 V) but will require an additional external voltage divider in order to provide a trigger to the interrupt pin on the Arduino when the Super-Capacitor voltage is sufficient to power the Arduino Uno WIFI. The circuit schematic for the implemented boost regulator circuit is in Figure 5.

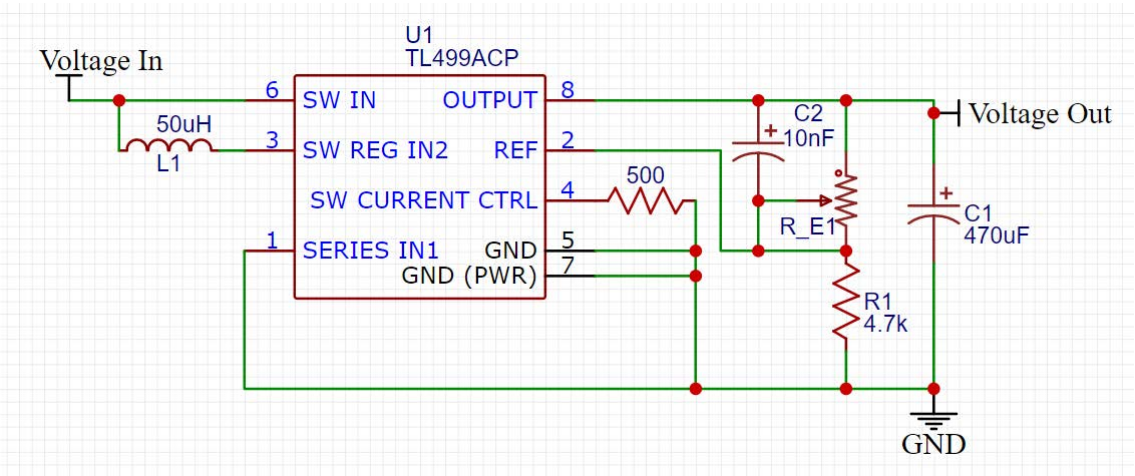

Figure 5: Sample circuit for TL499 boost converter

D. Chip performance testing

The boost converter circuits were tested with a series of trials. The first set of trials were conducted using a benchtop power supply to measure the charge/discharge time of the holding capacitors specified in the data sheets of the boost converters. The potentiometers of each circuit were adjusted so that the circuits would output 9.0V during these trials. The time for the *MAXIM 630* and *TL499* to reach 9.0V and to discharge to 4.5V are presented in Tables 4 and 6 respectively.

The second set of trials adds two supercapacitors and repeats the charge time measurements from the previous trial. The super-capacitors used were 1 Farad, 5.5V rated units. In order to hold a voltage sufficient to power the Arduino and avoid exceeding the maximum rating of the super-capacitors, they were connected in series, resulting in an 11 Volt rated, 0.5 Farad storage device. This super-capacitor bank was then connected in parallel with the specified holding capacitors already in the circuit, and the time to reach full charge and discharge for the *MAXIM 630* and *TL499* were recorded and presented in Table 5 and 7 respectively.

f. MAXIM MAX630

i. Power supply without 11V, 0.5F capacitor bank

1. As shown in Table 4, the Maxim circuit took much longer to charge the supercapacitors than the TI circuit, but the charge time is still within the realm of feasibility for the practical application so trials with this circuit were continued.

Charge/Discharge	MAXIM (V_{in} = 2.3V)
Δt 0.0V - > 9.0V (s)	9.07
Δt 9.0V - > 4.5V (s)	18.73

Table 4: Maxim charged from power supply without super-capacitors

ii. Power supply with 11V, 0.5F capacitor bank

1. As shown in Table 5 below, the charge times for this circuit with the supercapacitor included in the circuit under optimal conditions is far too long to be used in any practical application.

Charge/Discharge	MAXIM (V_{in} = 2.3V) 0.5F cap
Δt 0.0V - > 2.0V (m:s)	20:01.7
Δt 2.0V - > 3.0V (m:s)	28:56.5
Δt 3.0V - > 4.0V (m:s)	13:46.8
Δt 4.0V - > 5.0V (m:s)	16:51.4
Δt 5.0V - > 6.0V (m:s)	19:40.2
Δt 6.0V - > 7.0V (m:s)	24:34.7
Δt 7.0V - > 8.0V (m:s)	36:19.2

Δt 8.0V - > 9.0V (m:s)	50:52.0
Δt 9.0V - > 3.0V (m:s)	00:57.7
Δt 3.0V - > 0.5V (m:s)	02:16.1
Δt 0.5V -> 90mV (m:s)	03:52.8
Δt 90mV -> 50mV (m:s)	02:12.0
Δt 50mV -> 25mV (m:s)	03:51.8

Table 5: Charge/discharge rates for MAXIM with super-capacitors

g. TL499

i. Power supply without 11V, 0.5F capacitor bank

1. The TL499 chip exceeded expectation on the power supply and moved onto the next stage of trials.

Charge/Discharge	TL499 (V_{in} = 1.5V)
Δt 0.0V - > 9.0V (s)	0.87
Δt 9.0V - > 4.5V (s)	8.6

Table 6: Charge/discharge rates for TL499 without super-capacitors

ii. Power supply with 11V, 0.5F capacitor bank

1. The charge/discharge time measured for this chip, although much longer than without the capacitor bank, was still well within the realm of practicality for a self-powered device on the pipeline, and thus moved onto the next stage of testing.

Charge/Discharge	TL499 (Vin = 1.5V), 0.5F cap
Δt 0.0V - > 9.0V (s)	100.68
Δt 9.0V - > 4.5V (s)	38.33

Table 7: Charge/discharge rates for TL499 with super-capacitors

E. Combined circuit testing

This trial replaces the benchtop power supply with the TEG units. A heat sink with forced air was added to try and maintain a sufficient temperature differential across the TEG units. A photo of this setup is in Figure 6.

The supercapacitors were of such a size that the TEG's struggled to supply current, as such the charging time was considerably slower as shown in Table 8. During the test it was discovered that the temperature differential was difficult to maintain and the TEG's were reaching thermal saturation. As the tests went on, the increases in voltage grew slower and slower before eventually stopping completely. Once the voltage had stagnated, a touch of the hand onto the heated "cool side" of the TEG showed that the heat moving into the hand slightly desaturated the TEGs, which temporarily caused the voltage to increase again before the unit re-saturated.

h. Heat sink unit

i. Heat sink includes active and passive elements. Aluminum L bracket thermally pasted on top of *Marlow TG12-6 82078* Peltier junctions, with the secondary passive heat sink on top of L bracket holding the primary passive heat sink in place. Vertical component of L bracket is thermally pasted to passive heat sink with an active fan running off of a 16V power supply to simulate airflow that would be experienced on pipeline.

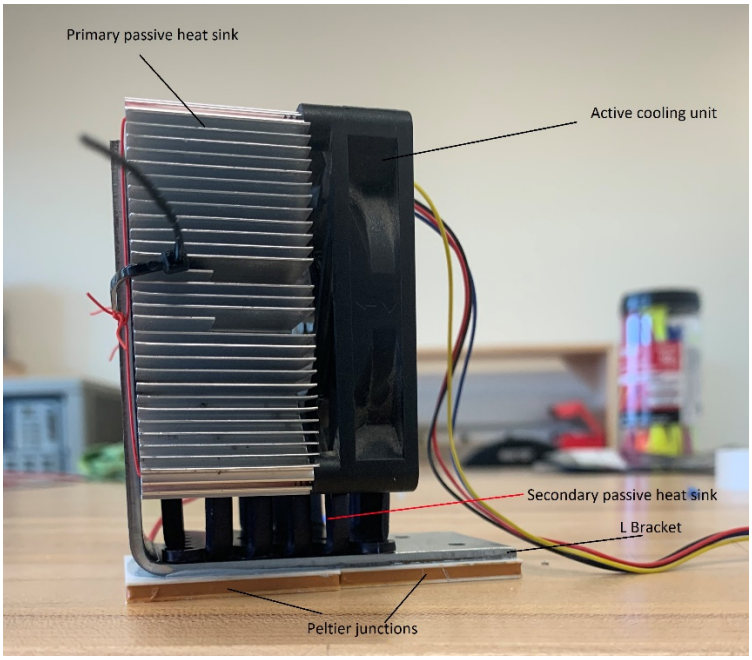

Figure 6: Heat sink unit for thermoelectric generators

i. System Trial

i. TL499

1. The *TL499* circuit was powered by the TEGs as shown in Figure 6 above. The circuit appeared to be monotonically increasing at first, but the longer the trial went on the clearer it became that even with the active cooling from the fan attached, the TEGs were thermally saturating. The monotonic increase in voltage developed into oscillating but still strictly increases in voltage, to oscillating but still net increasing voltage over any period, to oscillating about a voltage without any measurable change over a period of time. This trial was discontinued and deemed a failure.

Voltage (V_O)	Time (H:M:S)
0.2317 V	0:00:00
0.442 V	1:02:52

Table 8: charge rate for TEG powered TL499

3. Conclusions

Conceptual trials of the TEGs and boost regulators separately show promising results, however, without better thermal transport the thermoelectric generation will not work to power the microprocessor unit. Other avenues such as solar power should be explored.

Recommendations for further work would be to replace the Arduino Uno WIFI with a customized sensor platform such as a bare bones ATmega microprocessor unit to further cut down on power consumption. Development of a more efficient heat sink unit in order to draw more power from the thermoelectric generators are required if thermoelectric power is to be used.

4. Appendix A

- Data sheets for the following are attached in the file this report is in
  - Thermoelectric Generators
    - *TEC1-12706*
    - *Marlow TG12-6 82078*
  - Boost Converters
    - *TPS6122*
    - *Maxim 630*
    - *TL499*

Appendix B

- Code
  - Below is the code to be run by the Arduino in order to recognize interrupts and to begin taking data
    - #include <avr/sleep.h> // sleep library
    - #define interruptPin 2 // pin used to wake up arduino
    - int sensorValue = 0; // declaring int to store voltage, to be replaced with storing pipeline data
    - const int analogInPin = A0; // naming pin to be measured for ease of reading code
    - void setup() {

```
  Serial.begin(9600); // start sending data to the serial, at 9600 to match the processing code that is the companion for this program
  pinMode(interruptPin, INPUT_PULLUP); // seting the interrupt pin to use the internal pull up resistor
}
void GoingtoSleep(){
  sleep_enable(); // enables sleep mode
  attachInterrupt(0, WakeUp, HIGH); // give a way to exit sleep mode
  set_sleep_mode(SLEEP_MODE_PWR_DOWN); // selects sleep mode
  sleep_cpu(); // goes to sleep
}
void WakeUp(){
  Serial.println("Collecting data"); // indicates that the probe is collecting data
  sleep_disable(); // disable the sleep mode
  detachInterrupt(0); //removes the interrupt from the digital interrupt pin
}
void loop() {
    // when interrupt goes high, turn on device to begin taking measurements
    sensorValue = analogRead(analogInPin); // store value of voltage being read
    Serial.print(sensorValue); // prints value to serial monitor, to be replaced later with storing and or sending the data elsewhere
    Serial.print("\n");
    delay(250); // delays 250 ms before returning to sleep, if the interrupt is still high then the system will take another measurement and if the interrupt is no longer high then the system will remain in
    // sleep mode until the voltage drives the interrupt high
    GoingtoSleep(); // execute sleep mode function
```

- Below is the code to be run in Processing in order to take the data being sent to the serial port and store it on the local device.

```
import processing.serial.*;

Serial myPort;  // Create object from Serial class
String val;     // Data received from the serial port
PrintWriter output; //
int d = day();
int m = month();
int y = year();

void setup()
{
  // I know that the first port in the serial list on my mac
  // is Serial.list()[0].
  // On Windows machines, this generally opens COM1.
  // Open whatever port is the one you're using.
```

```
  String portName = Serial.list()[2]; //change the 0 to a 1 or 2, on this machine COM6 is 2
  myPort = new Serial(this, portName, 9600);
  String S = "C:\\Users\\Jacob\\Desktop\\Work\\Tests\\  test   " + str(m) + str('-') + str(d) + str('-') + str(y) + ".txt"; // adjust file directory for new machine
  output = createWriter(S);
  }

  void draw()
  {
  delay(100);
  if ( myPort.available() > 0)
  {  // If data is available,
  val = myPort.readStringUntil('\n');         // read it and store it in val
  }
  int h = hour();
  int M = minute();
  int s = second();
  String Time = str(h)+str(':')+str(M)+str(':')+str(s);
  String valT=Time + str(' ') + val;
  output.println(valT); //print it out to the file
  }

  void keyPressed() {
  output.flush(); // Writes the remaining data to the file
  output.close(); // Finishes the file
  exit(); // Stops the program
  }
```

- Below is the code used to find the voltage required to turn the digital pin high

```
  int sensorValue = 0.0;
  const int analogInPin = A0;
  const int IntPin = 2;
  int Intstate = 0;
  char space = '  ';
  float k = 0.0;
  void setup()
  {
  //initialize serial communications at a 9600 baud rate
  Serial.begin(9600);
  pinMode(IntPin, INPUT);
  }
  void loop()
  {
  sensorValue = analogRead(analogInPin); // reads the voltage on the analog in pin
```

```
Intstate = digitalRead(IntPin); // reads the digital voltage of the interrupt pin
k = 5 * sensorValue / 1024.0;
Serial.print(sensorValue); // prints the analogue voltage value to the monitor
Serial.print(space);
Serial.print(Intstate); // prints the interupt pin value to the monitor
Serial.print(space);
Serial.print(k, 3); // prints the interupt pin value to the monitor
Serial.print("\n");   // new line
//wait 250 milliseconds so we don't drive ourselves crazy
delay(250);
}
```

5. References

[1] Marlow Industries, *Technical Data Sheet for TG12-6*, DOC# 102-0343 REV M www.marlow.com

[2] Hebei I.T. (Shanghai) Co,. Ltd, *Thermoelectric Cooler TEC1-12706,* www.hebeiltd.com.cn Rev 2.03

[3] Texas Instruments, *TPS6122x Low Input Voltage, 0.7 V Boost Converter With 5.5uA Quiescent Current.* www.ti.com SLVS776B –JANUARY 2009–REVISED NOVEMBER 2014

[4] Maxim, *CMOS Micropower Step-Up Switching Regulator* www.maximintegrated.com/en.html , 19-0915; Rev 2; 9/08

[5] Texas Instruments, *TL499A Wide-Range Power-Supply Controllers.* www.ti.com, SLVS029H –JANUARY 1984–REVISED NOVEMBER 2015

Circuit board layouts were done using the online tools provided by https://www.circuitlab.com/ and https://easyeda.com/